Beyond Viscosity—How Density, Vibration and Interfacial Tension Affect Solvent Aided
Bitumen Production

by

Robert Alexander Stewart

A thesis submitted in partial fulfillment of the requirements for the degree of

Doctor of Philosophy

in

Chemical Engineering

Department of Chemical and Materials Engineering
University of Alberta

Abstract

Bitumen and heavy oil comprise a significant percentage of proven oil reserves globally. The environmental impacts of producing these resources with current technologies is a concern for environmentalists, oil producing companies, resource rich jurisdictions and society at large. Dilution of the viscous oil with solvents could permit the production of these reserves with lower greenhouse gas emissions than is achieved using current thermal methods where viscosity is reduced by heating. Solvent injection has yet to be implemented as the production method of choice and this suggests that there is significant residual technological uncertainty. Two orders of magnitude disagreements between predicted production rates, based largely on analogies with thermal production methods, and rates extrapolated from laboratory and pilot plant experimental results contribute to this uncertainty, and underscore fundamental and process knowledge gaps between laboratory experiments and field application.

This thesis addresses a number of potential impacts of adding solvents to bitumen production processes, whether pilot plants or operating facilities that have been under represented in the publically available literature to date. The addition of solvents to the production environment changes fluid properties beyond the desired viscosity reduction. Changes in fluid density and interfacial tension impact the force balance in reservoirs and laboratory apparatus. External factors such as ambient vibration can also affect production outcomes. The impacts of properties and external environmental conditions are addressed in this work through the systematic application of dimensionless group comparisons and scaling analysis benchmarked with experiments. The change in density of the hydrocarbon

with the addition of solvent relative to connate water density is addressed. Conditions where the hydrocarbon phase density changes from more to less dense than that of water are identified. Implications for the production of bitumen are discussed. The impacts of vibration are addressed. An experimental apparatus is described and the predominance of impacts arising from bubble formation and movement in vibrating unconsolidated porous media systems are illustrated using Ultra Violet (UV) fluorescent imaging. The apparatus, experimental outcomes and scaling analysis are expected to apply to diverse processes from packed catalyst beds in process reactors to geologic carbon dioxide sequestration in addition to bitumen and heavy oil production. Dimensionless group analysis is used to compare and contrast solvent and thermal production environments. Bond number value differences suggest that interfacial tension plays a larger role in solvent assisted production environments than previously recognized. This insight, along with support from Prandtl and Schmidt number values, support a new but as yet unproven discrete flow mechanism "sloughing at the bitumen solvent interface" that controls the kinetics of solvent assisted bitumen production.

Outcomes from this work are relevant to industrial and academic researchers alike in the target application. They will influence experimental design, apparatus construction and operation, and hypothesis testing as researchers attempt to reduce environmental impacts of heavy hydrocarbon and bitumen production. Impacts in related fields involving complex fluid motion in porous media are also anticipated. The ongoing relevance and importance of scaling laws and dimensional analysis is underscored.

Preface

This document is written using the paper based format and contains published material that has multiple authors and contributors. Robert Stewart was responsible for the research programs associated with all of the works within this thesis.

Published work:

Chapter 2: Stewart, Robert A., Wood, Caitlin V., Murowchuk, Steven J., Shaw, John M., "Phase Order Inversion During Heavy Oil and Bitumen Production with Solvent Addition", Energy & Fuels 2014, 28(7), pp 4835-4848.

Chapter 3: Stewart, Robert A., Shaw, J.M., "A dynamic pressure view cell for acoustic stimulation of fluids - Micro-bubble generation and fluid movement in porous media", Review of Scientific Instruments 2015, Vol 86 Issue 9, pp 1-13 (095101).

Named co-authors, Caitlin Wood and Steven Murowchuk, were summer and co-op students respectively under Robert's direct supervision. These individuals contributed to the above referenced publication by completing experiments and compiling data. Robert's supervisor, J. M. Shaw, supported all of the work in this document, including the two published works referenced above, through critical review and support of the research program, concepts, and publications.

Chapter 4: Stewart, Robert A., Shaw, J.M., "On vibration induced fluid and particle motion in unconsolidated porous media – observations and dimensional scaling analysis", will be submitted for publication at an appropriate journal and includes the use of otherwise unpublished interfacial tension data for 1-methynaphthalene and water measured by Ifeanyichukwu (Bobby) Uyanwune in the lab of Dr. Hongbo Zeng, Chemical and Materials Engineering, University of Alberta.

Chapter 5: Stewart, Robert A., Shaw, J.M., "Interface renewal and concentration shock through sloughing – accounting for the dissonance between production models and measured outcomes for solvent assisted bitumen production processes", comprises an un-submitted discussion paper that connects the concepts of the previous three chapters and points to a more complete understanding of solvent assisted bitumen production. A similar article will be submitted to The Journal of Canadian Petroleum Technology or a similar journal in the future.

Dedication

This publication is dedicated to my family, fiancée and friends without whom I would not have made it to this stage or through the PhD program. To my Parents, Hugh and Miranda Stewart, thank you for your constant support throughout my life of learning, fostering/stimulating my curiosity and providing light when all seemed dark. My Fiancée Laura Baxter, who supported me through this PhD and without whom it would have been much longer, more stressful, less successful, you gave, and continue to give me something to look forward too. My sisters Fiona and Katrina Stewart who provided support and friendship as well as critical reality checks when I need them most. Finally my friends, specifically David Chalmers and Brendan Tallon, you provided support, necessary outside perspective and breaks away from the drudgery throughout the duration of this degree.

This thesis and resulting PhD are your success as much as mine. Thank you!

Acknowledgements

Table of Contents

List of Tables

List of Figures

List of Symbols

Chapter 2

x_i	mass fraction of component i
ρ_i	density of component i

Chapter 3

f	frequency in Hz
c	speed of sound in a fluid in m/s
L	length in m
n	a positive integer
0	subscript denotes the properties of the continuous fluid phase
v	volume fraction of bubbles
β	bulk modulus of the fluid in Pa
ρ	combined fluid (liquid and gas) density in kg/m^3
g	subscript denotes the properties of the gas
P	pressure in Pa
r	bubble radius in m
γ	is the adiabatic exponent

Chapter 4

D	bubble or tube diameter in m
Ω	angular frequency of the oscillation in Hz
ρ	density of the liquid drop in kg/m^3
ρ_0	density of the continuous liquid phase in kg/m^3
μ	dynamic viscosity of the liquid in Pa*s
σ	interfacial tension between two liquids in N/m
k	ratio of specific heats of the gas bubble
P_0	average pressure in the continuous fluid in Pa
α	sound attenuation coefficient

x	distance from the location in m
I_0	reference sound intensity

Chapter 5

δ	film thickness in m
μ	dynamic viscosity of the liquid in Pa*s
v	average velocity in m/s
ρ	density in kg/m^3
θ	angle of incline
C_a	concentration of component a in a fluid
D	mass diffusion coefficient in m^2/s
t	time from the initiation of diffusion in seconds
σ	interfacial tension between two fluids
C_p	specific heat of the system
k	thermal conductivity of the system
$\varnothing$	porosity
y	distance from the initial in m
l	subscript for continuous liquid phase
W	subscript for wetting phase
D	subscript for displacing phase
P	subscript for producing phase
as	subscript for saturation limit of component a

Chapter 1: Introduction

Heavy Oil and Bitumen Production

High-viscosity and high-density hydrocarbon deposits (heavy oils, bitumen) are located in many places around the world including a proven 169.3 billion barrels in Alberta, Canada [1] that accounts for 10.2 % of in place proven reserves [2]. These resources typically require some form of stimulation in order to be produced and they are being or have already been produced in Saudi Arabia, USA, Russia, Venezuela and Canada. Some deposits, such as those in Alberta, Canada, are very close to the surface, and are produced through mining. Other deposits, such as in the Orinoco Delta in Venezuela and Colombia, are much deeper and therefore warm enough to be produced using down-hole pumps. In the reservoirs that are too cold and therefore very viscous and are inaccessible by mining techniques, steam is injected to heat the formation and reduce the viscosity of the hydrocarbon that is then pumped to the surface. In Canada, the heavy oil that requires thermal viscosity reduction or is mined is called bitumen. Many different methods of thermal stimulation have been tested and locally successful ones are exploited at large scales in California and Alberta.

While 70-80% of the emissions from hydrocarbons come from end users (combustion) [3], the need to reduce the energy intensity and therefore emissions from oil, and specifically heavy oil production, has intensified, and has become critical to maintaining the social license to produce these resources. Thermal production methods are more emissions intensive than mining [4] and 80% of the resource is not accessible by mining [3]. Potential customer losses have already been felt in Canada—through legislated limitations imposed on market access (oil composition) and pipeline construction. Despite improvements in emission intensity achieved by the industry, significant additional work is required to reduce or eliminate the emissions, and to improve public perception and to provide an ongoing social license to operate.

Thermal viscosity reduction has been the primary method for producing the heavy oils since the 1950's when Cyclic Steam Stimulation (CSS) was first used successfully in Venezuela [5]. CSS uses a single vertical well. During stimulation, steam is injected and heats the heavy oil in place. This part may take months. Inside the reservoir the mobile heavy oil is denser than water so it settles to the bottom of the oil free chamber produced during previous cycles. Once the reservoir reaches a desired temperature the reservoir is produced, generally with a down-hole pump or pump-jack through the same vertical well. This method proved viable where the reservoir was thick enough to minimize heat losses, where the overburden could withstand the pressure, and there was enough oil accessible to make the well economic. Thinner reservoirs, or thinner sections of reservoirs, were not developed until horizontal wells became possible.

Horizontal drilling allowed one well to access a large area of thinner reservoirs making recovery economic. A different process, Steam Assisted Gravity Drainage (SAGD) exploiting horizontal drilling technology, was developed by Butler et al. in 1980 [6]. This process uses two parallel horizontal wells in continuous operation. The upper well is used to inject steam and the lower well is used to produce heavy oil. This continuous process has been adopted widely in Alberta, Canada. Through the steam injection process a chamber surrounding the well pair is developed with oil free sand inside the chamber, mobile oil at the interface and non-mobile reservoir outside the chamber. As with CSS, the bitumen is denser than water and flows toward the bottom of the reservoir where it is pumped to the surface. As SAGD is a continuous process the steam–water interface elevation must remain above the producer to prevent short-circuiting of the steam. This steam trap is maintained by controlling the rate that fluid is removed from the chamber and due to the density difference between bitumen and water, it is generally understood that a liquid water layer acts as the trap. Multiple horizontal wells are co-located on a single well pad. Only small surface disturbances are needed to facilitate access to large areas of the oil reserve. The SAGD process has better economics and smaller environmental impact intensities than CCS. Both SAGD and CSS require large volumes of make-up water and natural gas for combustion to generate steam. The industry wide average of volume of make-up water per

barrel of heavy oil produced is 3.18 m^3 water/m^3 oil [4] with a large range depending on reservoir conditions.

The industry has been focused on fresh water use reduction for a long time and achieves a high rate of recycle as well as use of brackish water from saline aquifers. The cost of the processing facilities to bring the water to boiler feed water quality is a significant component of the capital cost of the bitumen production facilities. This combined with the natural gas consumption to fuel the steam generators, makes the cost per barrel of heavy oil produced in both capital and operating level, much higher than for conventional onshore oils.

With the environmental aspect of the in-situ heavy oil production related to water being dealt with through efficient recycle of produced water, the main environmental impact of the thermal production processes is the emissions from natural gas combustion. Large quantities of natural gas are burned to produce the steam that is injected into the heavy oil reservoirs. Steam generation is achieved through Once Through Steam Generators (OTSG) or Heat Recovery Steam Generators (HRSG) on the back end of a cogeneration facility. Both processes have been optimized for efficiency—driven by emissions regulation and natural gas costs. Cogeneration facilities produce electricity using gas turbines upstream of the HRSG that is sold into the Alberta electrical system to enhance the operating economics of a project. Nonetheless both processes produce a large volume of emissions that is now the main focus for environmental stewardship improvement.

Solvents have been suggested as a method to reduce heavy oil viscosity in-situ with no or limited steam addition to reduce the emissions footprint of heavy oil production starting in the mid to late 1980's [7, 8]. Along with the reduction in emissions comes large capital and operating cost reductions through the elimination of water processing facilities and reductions in natural gas consumption. Solvents have been suggested as a method to reduce fresh water consumption but this is no longer a driving factor due to the very high level of water recycle already achieved in current operations. Solvents reduce the heavy oil viscosity through dilution, a process that is already completed on the surface to allow

shipping of the heavy oil by pipeline. The diluted bitumen is often referred to as dilbit. The cost of solvent is a major operating expenditure for producers that do not upgrade or refine bitumen prior to shipment. This has two benefits as the supply chain and associated economic risks are already understood and the cost of solvents, provided recovery is high, have already been factored into the cost of operations. The suggested solvents are generally readily available light hydrocarbons with high solubility in the heavy oil such as propane and butane. High-solubility inert gases, such as CO_2 have also been tested due to their availability. There is a myriad of options and variables that have been suggested and explored: mixtures of solvents, solvents as vapors, condensing solvents, liquid solvents, mixtures of steam and solvents. Many numerical, lab and field experiments have been completed with the hope that a solvent assisted process becomes the next standard for the industry replacing SAGD.

Other methods being tested for viscosity reduction include in-situ combustion where the viscosity is thermally reduced but no surface emissions are produced, electrical based heating, and either electromagnetic or resistance heating [9]. These methods are not considered further in this document as they are outside the scope of the work.

Published accounts on solvent assisted processes suggest that some process concepts are scalable and economic but, to date, none of these alternative processes has displaced the steam assisted thermal production methods. This suggests that the processes are uneconomic, not understood or incorrectly applied. The publically available literature is hampered by the lack of insights from corporate developments and may be missing key insights from field trials. Production models for solvent assisted bitumen production processes have consistently provided outcomes orders of magnitude worse than measured outcomes [7, 8, 10]. Without clear evidence of predictability, technological risk is prohibitive, and potential environmental and economic benefits remain elusive. Discovery of un-described phenomena that impact the use of solvents in heavy oil production is a clear priority in this field, if these potential benefits are to be realized. Fundamental understanding of the phenomena at play in solvent assisted heavy oil recovery is required.

A phenomenological approach that transfers insights developed from classical contributions to flow in porous media is adopted here.

Analysis of Forces in Reservoirs

Analysis of forces at play in a reservoir permits prediction of fluid movement and therefore the performance of stimulation techniques and production processes. As in all fluids in porous media there are static and dynamic forces interacting to cause specific outcomes. Static forces related to gravity, interfacial tension and pressure balance to hold fluids in position. For motion to occur the static forces must be overcome or unbalanced. Flow rate is then dependent on the resistive viscous force. External pressure gradients, either static or time dependent are often at play during production and under reservoir conditions. Inertial forces balance out the equation to determine the rate of change of fluid motion. With simple fluids, known properties and geometries, force and momentum balances can be completed to determine how fluids move. In more complicated systems where there are numerous unknowns one must rely on an understanding of governing phenomena. Well-known dimensionless groups are very powerful tools for determining prevailing influences.

Scaling analysis can be approached using two generally relied upon methods: the Buckingham Pi Theorem [11] and Inspectional Analysis [12]. The Buckingham Pi Theorem is generally adopted if only characteristic properties of the system are known. For example the viscosity, velocity and density of a fluid in a pipe of known diameter fully captures the characteristic information for single phase pipe flow and yields the well-known Reynolds number. To apply Inspectional Analysis, the equations governing the system and the associated boundary conditions must be known. The specificity of Inspectional Analysis yields a more complete analysis of a system but the approach is complicated to apply and does not work well in systems where there are many unknowns.

Fluid properties are very important for both force balance calculations and dimensional analysis. Without accurate data outcomes are difficult to interpret or apply for individual

cases and comparisons among cases are precluded. It is paramount that properties under operating conditions be available and understood. Governing properties include: fluid composition, temperature, pressure and interfacial tensions among phases present and with the reservoir medium. The impact of changes or uncertainties of these properties, or parameters of the system, must be carefully weighed to determine whether they are material to production performance, and if so where physically at steady state or when temporally at a specific location. For example, the addition of solvents and the injection method employed alter numerous system properties that are not impacted or are impacted differently in thermal production methods. Solvent addition changes the density of the produced fluid and its relationship with the density of water, and alters the interfacial properties. This impacts fluid transport within the reservoir and introduces behaviors different from those arising in thermal production processes. To date, these differences are under-represented in the literature because the central idea—that reducing the viscosity allows oil to flow—is so entrenched that potential impacts of other properties such as density, the subject of Chapter 2, and interfacial tension differences are largely absent from the publically available literature. While high-pressure and high-temperature interfacial tension measurements are outside the scope of this study, the case for such measurements is clearly made in Chapter 5, where dimensional analysis leads to a previously un-described mechanism for interface renewal in solvent assisted production processes that resolves the dissonance between experimental and predicted production outcomes.

Vibration and Dissonance Between Predicted and Measured Outcomes

Production outcomes from laboratory and pilot scale physical models for solvent assisted production processes can be impacted by vibrations produced by equipment that is transmitted to the experimental apparatus. These impacts are not considered in the interpretation of results in the publically available literature, and have not been assessed as a possible explanation for the dissonance between measured and predicted production outcomes. Vibration introduces an additional variable to the already complicated

production environment. Including vibration in the scaling analysis, the subjects of Chapters 3 and 4, is key to initiating discussion on the topic. Chapter 3 concerns the development of an apparatus to test how vibration impacts the relative motion of components within bubble–liquid–unconsolidated porous media environments. Scaling analysis and experimental results are reported in Chapter 4.

Objectives

The objective of this work is to outline a phenomenological approach to understanding fluid motion in unconsolidated porous media with concentration gradients and vibration. The insights and methods described extend beyond a specific industrial application to include contamination movement in aquifers, carbon sequestration, and hydrocarbon refining among other applications. The understanding developed shall be presented in a way that it is broadly applicable. The specific industrial focus of this work concerns solvent assisted bitumen production processes and the gap between theory and experimental work. The key questions related to this are:

- Do changes in fluid properties, density and interfacial tension in particular, associated with solvent addition affect fluid motion differently than in thermal methods of bitumen production?
- Does vibration impact two and three phase fluid motion in unconsolidated porous media?
- Can the apparent dissonance between experimentally measured and predicted solvent assisted bitumen production rates be attributed to identifiable phenomena?

Approach

These questions are approached from the perspective of changes in the force and energy balances arising from the addition of solvent and vibration to reservoir like environments. Methodical use of dimensionless groups supported by experimental investigation of specific and previously untested phenomena are cornerstones of the project. A cross-disciplinary view of the research outcomes has been maintained throughout the thesis to extend the applicability of outcomes to audiences beyond those interested in heavy oil production. The same fundamental forces are at play and the same types of deconstruction to basic principles apply to carbon sequestration, contaminant movement in aquifers as well as processing technologies.

Outline

This thesis was prepared in paper format with four chapters written as stand-alone publications. The second and third chapters were published in Energy and Fuels, and The Review of Scientific Instruments respectively. Chapter four has been submitted to Water Resources Research, and Chapter five will be submitted to The Journal of Canadian Petroleum Technology or a similar journal. Conclusions and future work comprise Chapter six.

The four technical chapters progress through under-explored phenomena caused by changes in fluid and reservoir properties that can occur when solvents are added to bitumen production environments. The addition of solvents can change the fluid density, induce vibrations to the system and change the interfacial tension. Chapter two looks at how the addition of solvent changes the density of the hydrocarbon and therefore changes the gravity driven orientation of aqueous and hydrocarbon phases. The specific temperature, pressure and composition at which this phase order inversion is determined through data collection and used to validate a simple mixing rule approach for calculation.

Chapter three discusses the development of a dynamic pressure view cell to allow the observation of vibrations in porous media. Chapter four uses scaling analysis to determine frequencies and length scales where vibration causes disruption to static liquid–bubble–unconsolidated solid media force balance. The dynamic pressure view cell is used with a UV fluorescent imaging system to observe that the presence of bubbles dominates the result of vibrations on fluids in unconsolidated porous media. This impacts both experimental tests, pilot operations and industrial applications of adding solvent to bitumen reservoirs. Chapter five addresses the change that solvent makes to the interfacial tension balance compared to thermal production methods. This change in interfacial tension allows for the development of a discontinuous flow concept, called sloughing, to explain the observed ~100x higher mass transfer in solvent driven bitumen production experiments than predicted using Fickian diffusion. Density gradients between solvent and diluted bitumen drive repeated interface flow events followed by rapid diffusion of solvent across a high concentration gradient causing higher production rates than if the solvent has to continuously diffuse through a flowing film.

References

[1]   Government of Alberta, "Oil Sands: The Resource," 2012. [Online]. Available: http://www.oilsands.alberta.ca/FactSheets/Resource_FSht_June_2012_Online.pdf. [Accessed: 19-Mar-2016].

[2]   "EIA International Energy Statistics," 2014. [Online]. Available: http://www.eia.gov/cfapps/ipdbproject/iedindex3.cfm?tid=5&pid=57&aid=6&cid=regions&syid=2010&eyid=2014&unit=BB. [Accessed: 19-Mar-2016].

[3]   IHS CERA, "Oil Sands, Greenhouse Gases, and US Oil Supply: Getting the Numbers Right," 2012.

[4]   A. Brandt, "Upstream greenhouse gas emissions from Canadian oil sands as a feedstock for European refineries," 2011.

[5]   J. Alvarez and S. Han, "Current Overview of Cyclic Steam Injection Process," *J. Petro. Sc. R.,* vol. 2, no. 3, pp. 116–127, 2013.

[6]   R. M. Butler, "Method for continuously producing viscous hydrocarbons by gravity drainage while injecting heated fluids," CA1130201A1, 1979.

[7]   R. M. Butler and I. J. Mokrys, "Solvent analog model of steam - assisted gravity drainage," *AOSTRA J. Res.*, vol. 5, no. 1, pp. 17–32, 1989.

[8]   S. G. Dunn, E. H. Nenniger, and V. S. V. Rajan, "A study of bitumen recovery by gravity drainage using low temperature soluble gas injection," *Can. J. Chem. Eng.*, vol. 67, pp. 978–991, 1989.

[9]   Oil Sands Discovery Centre, "Facts about Alberta's oil sands and its industry," 2014.

[10]   J. E. Nenniger, "How Fast is Solvent Based Gravity Drainage?," in *Canadian International Petroleum Conference*, 2008.

[11]   F. M. White, *Fluid Mechanics*, 6th ed. New York: McGraw Hill, 2008.

[12]   A. E. Ruark, "Inspectional analysis - a method which supplements dimensional analysis," *J. Mitchell Soc.*, 1935.

Chapter 2: Phase Order Inversion During Heavy Oil and Bitumen Production with Solvent Addition

Robert A. Stewart, Caitlin V. Wood, Steven J. Murowchuk, John M. Shaw

Introduction

Gravity drainage production of hydrocarbons relies on the density difference between fluids in the reservoir to allow separation and production of the desired phase [1-5]. In the Steam Assisted Gravity Drainage (SAGD) process used for the production of Athabasca Bitumen, the injected steam, the condensed steam and mobilized connate water are all less dense than the hot bitumen. Placement of the producer wells close to the bottom of reservoirs maximizes recovery. As bitumen and water are co-produced, primary separation at the surface is based on a similar order of phase densities.

The use of solvents for viscosity reduction during in situ production is not a new concept but due to the additional cost and complexities compared to thermal production techniques, especially the sensitivity of process economics to solvent recovery, this approach has not been implemented on a large scale. The continued desire to reduce the environmental impact and the cost associated with thermal production of bitumen and heavy oil drives the development of solvent assisted production techniques. The density and viscosity of Athabasca bitumen + solvent mixtures has been explored by numerous research groups [6-14] in support of solvent assisted process development and the phase inversion of heavy hydrocarbons with water has also been observed [15]. However, the impact of density gradients and phase order inversion in solvent addition processes appears to have been overlooked. During production it is difficult to avoid a broad range of solvent + bitumen compositions arising in a reservoir and this affects the spatial distribution of the density gradients that are the driving force for production by gravity

drainage [2-4]. Several data sets for the density of bitumen or bitumen fraction + solvent or gas mixtures [7,9,10,12-14,16] are shown in Figure 2-1. The data sets include both "live" and "dead" bitumen samples from different reservoirs in Northern Alberta combined with CO, CO_2, ethane, propane, pentane and toluene. It is also worth noting that the Athabasca bitumen sample used by Amani et al. [12] is from the same batch employed in the present work. Some mixtures possess higher densities than water, others possess densities lower than that of water. Some mixtures saturate before they cross the density of water, while others straddle the density of water and can be either more dense or less dense than water depending on the global composition, temperature and pressure. As the density of bitumen from diverse sources is greater than but comparable to the density of water, most added solvents and light gases have the potential to reduce the density of the hydrocarbon rich phase to values lower than that of water over ranges of composition temperature and pressure. Consequently, the phase order can change. Phase order inversion is likely to occur in heavy oil reservoirs subject to solvent injection, even if the phase state of the solvent, at the point of injection, and operating conditions within the reservoir are selected with care.

In this work, the principles of phase order inversion, and the roles of pressure, temperature, and composition on phase order are explored using high quality density data for mixtures comprising Athabasca bitumen as the base hydrocarbon and heptane and toluene as solvents. The densities of these mixtures are compared with correlations for pure water [16] and measured density values for SAGD produced water. Phase order inversion modeling and implications regarding the use of solvents in bitumen or heavy oil production and processing are also discussed. The impact of water solubility on hydrocarbon phase density is ignored because the impact is negligible under the range of conditions of interest in the present work [19].
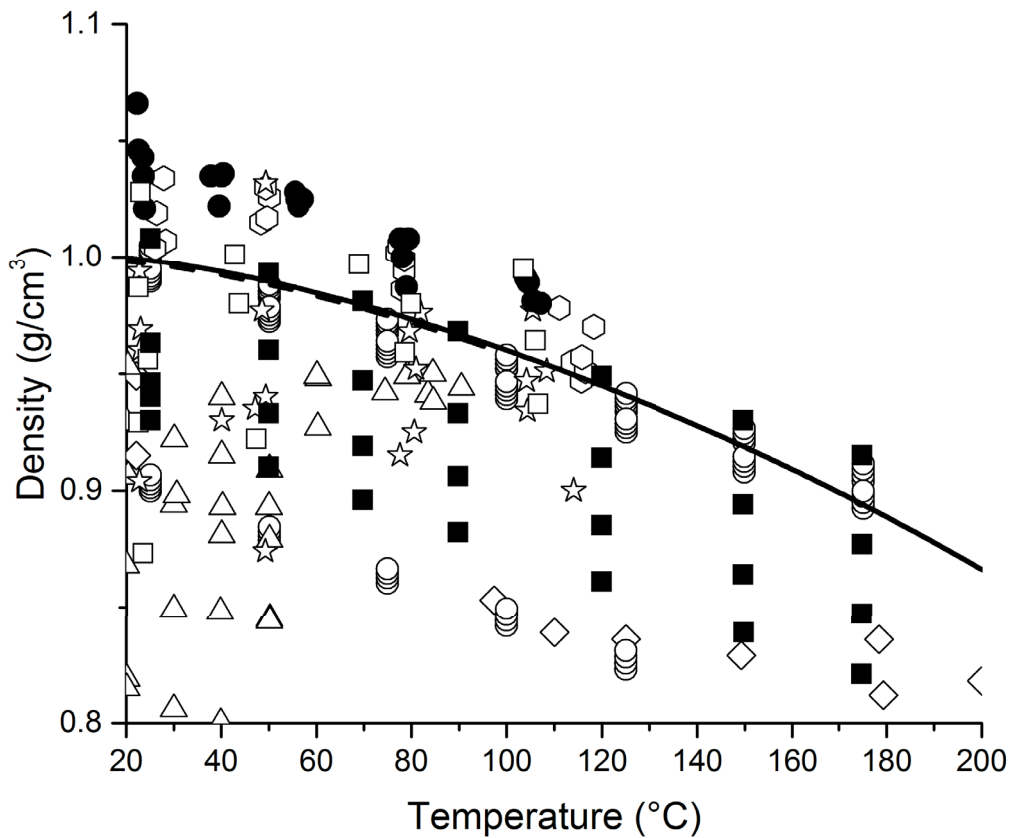
Figure 2-1: Reported density data for bitumen and bitumen fractions + light hydrocarbons and gases relative to water. The pseudo binary mixtures are: Athabasca bitumen + 0.448, 0.667 mass fraction toluene from 0.10 to 12.47 MPa [12] (◇), Peace River bitumen saturated with C_2H_6 from 1.39 to 4.25 MPa [9] (▢), Athabasca Bitumen saturated with CO from 2.8 to 9.93 MPa [14] (⬡), Athabasca Bitumen + 0.052 to 0.261 mass fraction C_3H_8 at from 0.86 to 4.93 MPa [7] (△), Dead Peace River Bitumen + 0.03, 0.06, 0.30 mass fraction condensate from 0.10 to 10 MPa [13] (◯), Athabasca Bitumen saturated with C_2H_6 from 1.3 to 8.6 MPa[14] (☆), Peace River Bitumen saturated with CO2 from 1.5 to 6.2 MPa [9] (●), Athabasca Bitumen + 0 to 0.154 mass fraction C_5H_{12} at 1 MPa [10] (■), Water (NIST) at 3.45 MPa [16] (—), Water (NIST) at 0.101 MPa [16] (– –).

Experimental

Materials

The bitumen sample, supplied by Syncrude Canada Ltd., was mined and then partially processed. It was retrieved following naphtha recovery and it is designated as a coker feed. Thermophysical properties, composition, and the phase behavior of this specific sample are available in a number of recent publications [17-19]. Solvents, Fisher scientific HPLC grade toluene and n-heptane, have nominal purities of 99.9% and 99.6% respectively. A SAGD produced water sample, obtained from the Shell Orion facility in the Cold Lake region of Alberta, was used as received.

Mixture Preparation for Phase Density Measurement

Two approaches were adopted for mixture preparation that depended on the anticipated viscosity range of a mixture. For mixtures with low viscosity, Athabasca bitumen + toluene (0.20 – 0.90 mass fraction toluene) and Athabasca bitumen + heptane (0.20 – 0.90 mass fraction heptane), 100 to 200 gram batches were prepared by mixing bitumen preheated to 80°C into the solvents at room temperature using a flask, and a magnetically driven bar stirrer. For more viscous samples, Athabasca bitumen + toluene (0.20 mass fraction toluene or less) and Athabasca bitumen + heptane (0.20 mass fraction heptane or less), 30 to 40 gram batches were prepared by adding solvent to bitumen in sealed containers, held at 80°C and shaken at intervals over the course of 3 days. In both cases, aliquots of these samples were injected into the density meter using a syringe.

Density Measurements

Anton Paar DMA 5000 and DMA HP density meters were used for density measurements. The DMA 5000 operates at atmospheric pressure and at temperatures ranging from 15 to 80°C, and is equipped with an automated sample changer and temperature scan feature. Both of these features were used here. Individual samples were also injected manually into the DMA 5000 and measurements were made at set temperature intervals, typically 1°C,

over the operating range of the device (10-80°C). For repeated measurements, samples were left in the density meter and the scans repeated. The DMA HP cell can be used from ambient conditions up to 69 MPa and 200°C. Individual samples were injected manually and a nitrogen atmosphere was used to exert the desired pressure on the fluid. Measurements were made at selected temperatures and pressures.

For both devices, the period of oscillation of a U-tube, which contains a sample, is correlated with density. Both meters were calibrated using density standards and viscosity correction was applied to measurements reported for the DMA 5000 using a built-in proprietary Anton Paar function. The DMA 5000 was calibrated using De-Ionized and Ultra-Filtered (DIUF) water and air across the measurement temperature range as per the instruction manual. The DMA HP was calibrated using DIUF water and nitrogen and the Anton Paar wide range adjustment tool. This tool uses a number of known sample densities to generate a polynomial function with oscillation frequency as the measured input and density as the output. The reported measurement accuracies are: +/- 10^{-5} g/cm^3 for the DMA 5000 and +/-10^{-4} g/cm^3 for the DMA HP. In this work, all measurements shown with a pressure were measured using the DMA HP. If no pressure is given the sample was measured using the DMA 5000 at atmospheric pressure. With both density meters, deviations arising from measurement repeatability and reproducibility were assessed. For each density measurement, the average density value, the number of repeated measurements and the value of the maximum measured deviation from the average measurement are reported.

Three types of measurement validation experiments were performed with the density meters. These assessed measurement deviation from values for toluene, heptane and water recommended by NIST [16], the repeatability of measurements, and the reproducibility of measurements particularly for mixtures containing bitumen. The maximum deviations for toluene and n-heptane density values (obtained using the DMA 5000) from those recommended by NIST are 0.0001 g/cm^3 and 0.0005 g/cm^3 respectively, as shown in Table 2-1. These values are within the uncertainty of the values provided by NIST, 0.05% for toluene and 0.2% for n-heptane respectively [16]. The maximum deviations for toluene and

DIUF water measured in the DMA HP at 20 and 80°C and atmospheric pressure were 0.0006 g/cm^3 and 0.00001 g/cm^3 respectively as shown in Table 2-2. These deviations are within same order of magnitude as the uncertainties provided by NIST for water. The maximum deviation values for DIUF water and toluene measured in the DMA HP at 1.1 and 3.26 MPa, 0.00015 g/cm^3 and 0.0017 g/cm^3 respectively, also shown in Table 2-2, are an order of magnitude larger than the uncertainty of water density values recommended by NIST. These uncertainties, while small in absolute and relative terms, were the largest found in any of the comparisons against NIST values, or repeated measurements and therefore are the largest quantifiable source of uncertainty for the DMA HP measurements with pure or nearly pure fluids. Density measurements were also reproduced in both the DMA 5000 and the DMA HP units to determine the maximum uncertainty associated with bitumen density measurements. These values are reported in Tables 2-3 and 2-4 respectively. While, the magnitude of the repeatability uncertainty of the DMA HP with the solvents and water were within the manufacturer's estimated uncertainty, uncertainties for Athabasca bitumen were found to be significantly larger. The largest uncertainty found across all measurements was the reproducibility of bitumen density between the DMA 5000 and the DMA HP units - +/- 10^{-2} g/cm^3. Consequently, this measure of reproducibility is used to assess the impact of bitumen density uncertainty on phase order inversion envelopes and the applicability of ideal mixing as a basis for phase density calculation. While high, this uncertainty is consistent with bitumen density value uncertainty reported elsewhere using a different measurement method [19]. Contributions to phase order inversion envelope uncertainty from solvent and water density uncertainty, temperature uncertainty, 0.001°C for the DMA 5000 and 0.05°C for the DMA HP, and pressure uncertainty, 20 kPa for the DMA HP are negligible by contrast.

Table 2-1: Heptane and Toluene DMA 5000 density measurements compared to NIST recommended values

Temperature (°C)	Measured density (g/cm³)	Deviation from NIST (g/cm³)	Measured density (g/cm³)	Deviation from NIST (g/cm³)
	Heptane		Toluene	
15	0.6881	0.0001	0.8714	-0.0001
20	0.6839	0.0001	0.8668	-0.0001
25	0.6797	0.0000	0.8621	-0.0001
30	0.6754	0.0000	0.8575	-0.0001
35	0.6711	0.0000	0.8528	-0.0001
40	0.6668	0.0000	0.8481	-0.0001
45	0.6624	-0.0001	0.8434	-0.0001
50	0.6580	-0.0001	0.8387	-0.0001
55	0.6536	-0.0002	0.8339	-0.0001
60	0.6492	-0.0002	0.8291	-0.0001
65	0.6447	-0.0003	0.8243	-0.0001
70	0.6401	-0.0004	0.8195	-0.0001
75	0.6355	-0.0005	0.8146	-0.0001
80	0.6309	-0.0005	0.8098	-0.0001

Table 2-2: DIUF water and Toluene DMA HP measurements compared to NIST recommended values

Temperature (°C)	Average pressure (MPa)	Average density (g/cm³)	Deviation of average from NIST (g/cm³)	Maximum deviation between repeats (g/cm³)	Number of repeats
De-Ionized Ultra Filtered Water			0.0002	0.00001	
20	0.101	0.99820	0.00001	0.000005	5
20	1.092	0.9988	-0.0002	0.000005	6
20	3.267	0.9998	-0.0001	0.000001	5
80	0.101	0.97180	-0.00001	0.000005	7
80	1.098	0.97219	0.00005	0.000006	4
80	3.266	0.97313	0.00008	0.000002	5
140	1.093	0.92660	-0.00008	0.000009	6
140	3.267	0.92769	0.00001	0.00001	5
Toluene			0.002	0.0001	
20	0.101	0.8663	0.0006	0.000004	5
20	1.095	0.8675	0.0001	0.000006	6
20	3.268	0.8692	0.0001	0.000003	5
80	0.101	0.8092	0.0006	0.00005	9
80	1.088	0.8093	0.002	0.00004	7
80	3.269	0.8117	0.002	0.00003	6
140	1.087	0.7492	0.0003	0.00002	5
140	3.268	0.7518	0.002	0.00003	7
200	1.103	0.6772	0.0003	0.00004	7
200	3.269	0.6837	0.0006	0.0001	8

Table 2-3: Density of Athabasca bitumen at atmospheric pressure (DMA 5000)

Temperature (°C)	Average density (g/cm³)	Maximum deviation between repeats (g/cm³)	Number of repeats	Average density (g/cm³)	Maximum deviation between repeats (g/cm³)	Number of repeats	Deviation between samples (g/cm³)
	Sample 1	0.0002		Sample 2	0.00006		0.00012
10				1.03190	0.00006	4	
11				1.03140	0.00006	4	
12				1.03088	0.00005	4	
13				1.03034	0.00005	4	
14				1.02978	0.00005	4	
15	1.02927	0.00002	3	1.02921	0.00005	4	0.00006
16	1.02869	0.00002	3	1.02863	0.00005	4	0.00006
17	1.02810	0.00002	3	1.02804	0.00005	4	0.00006
18	1.02751	0.00001	3	1.02744	0.00004	4	0.00007
19	1.02691	0.00002	3	1.02684	0.00004	4	0.00007
20	1.02631	0.00001	3	1.02623	0.00004	4	0.00008
21	1.02570	0.00001	3	1.02562	0.00004	4	0.00008
22	1.02509	0.00001	3	1.02500	0.00004	4	0.00009
23	1.02447	0.00001	3	1.02439	0.00004	4	0.00008
24	1.02386	0.00001	3	1.02377	0.00004	4	0.00009
25	1.02324	0.00001	3	1.02315	0.00004	4	0.00009
26	1.02262	0.00001	3	1.02253	0.00004	4	0.0001
27	1.02200	0.00001	3	1.02190	0.00004	4	0.0001
28	1.02138	0.00001	3	1.02128	0.00004	4	0.0001
29	1.020757	0.000007	3	1.02066	0.00003	4	0.0001
30	1.020133	0.000007	3	1.02003	0.00003	4	0.0001
31	1.019513	0.000007	3	1.01941	0.00003	4	0.0001
32	1.018890	0.000010	3	1.01878	0.00003	4	0.0001
33	1.018267	0.000007	3	1.01816	0.00003	4	0.0001
34	1.017643	0.000007	3	1.01753	0.00003	4	0.0001
35	1.01702	0.00001	3	1.01691	0.00003	4	0.0001
36	1.016397	0.000007	3	1.01628	0.00003	4	0.0001
37	1.015773	0.000007	3	1.01566	0.00003	4	0.0001
38	1.015147	0.000007	3	1.01504	0.00003	4	0.0001
39	1.014527	0.000007	3	1.01441	0.00003	4	0.0001
40	1.013903	0.000007	3	1.01379	0.00003	4	0.0001
41	1.013277	0.000007	3	1.01316	0.00003	4	0.0001
42	1.012657	0.000007	3	1.01254	0.00003	4	0.0001
43	1.012033	0.000007	3	1.01192	0.00003	4	0.0001
44	1.011413	0.000007	3	1.01129	0.00003	4	0.0001
45	1.010787	0.000007	3	1.01067	0.00003	4	0.0001
46	1.010167	0.000007	3	1.01005	0.00003	4	0.0001
47	1.009543	0.000007	3	1.00943	0.00003	4	0.0001
48	1.008923	0.000007	3	1.00881	0.00003	4	0.0001
49	1.008300	0.000000	3	1.00819	0.00003	4	0.0001
50	1.007680	0.000000	3	1.00756	0.00003	4	0.0001
51	1.007057	0.000007	3	1.00694	0.00003	4	0.0001

52	1.006437	0.000007	3	1.00632	0.00002	4	0.0001
53	1.005817	0.000007	3	1.00570	0.00003	4	0.0001
54	1.005197	0.000007	3	1.00508	0.00003	4	0.0001
55	1.004573	0.000007	3	1.00446	0.00002	4	0.0001
56	1.003950	0.000000	3	1.00385	0.00002	4	0.0001
57	1.003330	0.000000	3	1.00323	0.00002	4	0.0001
58	1.002710	0.000000	3	1.00261	0.00002	4	0.0001
59	1.002090	0.000000	3	1.00199	0.00002	4	0.0001
60	1.001470	0.000000	3	1.00137	0.00002	4	0.0001
61	1.000850	0.000000	3	1.00075	0.00002	4	0.0001
62	1.000230	0.000000	3	1.00014	0.00002	4	0.00009
63	0.999607	0.000007	3	0.99952	0.00002	4	0.00009
64	0.998987	0.000007	3	0.99890	0.00002	4	0.00008
65	0.998367	0.000007	3	0.99829	0.00002	4	0.00008
66	0.99775	0.00002	3	0.99767	0.00002	4	0.00008
67	0.99713	0.00002	3	0.99705	0.00002	4	0.00007
68	0.99650	0.00002	3	0.99644	0.00002	4	0.00007
69	0.99589	0.00003	3	0.99582	0.00002	4	0.00007
70	0.99526	0.00003	3	0.99521	0.00002	4	0.00006
71	0.99464	0.00004	3	0.99459	0.00002	4	0.00005
72	0.99402	0.00005	3	0.99398	0.00002	4	0.00004
73	0.99339	0.00005	3	0.99335	0.00003	4	0.00004
74	0.99277	0.00006	3	0.99275	0.00002	4	0.00003
75	0.99215	0.00008	3	0.99213	0.00002	4	0.00002
76	0.99152	0.00009	3	0.99152	0.00002	4	0.00001
77	0.9909	0.0001	3	0.99090	0.00002	4	0.00001
78	0.9903	0.0001	3	0.99029	0.00002	4	0.00002
79	0.9896	0.0002	3	0.98968	0.00002	4	0.00004
80	0.9890	0.0002	3	0.98906	0.00002	4	0.00006

Table 2-4: Density of Athabasca bitumen at elevated pressure (DMA HP)

Temperature (°C)	Average pressure (MPa)	Average density (g/cm^3)	Maximum deviation between repeats (g/cm^3)	Number of repeats
DMA HP Bitumen Sample 1			0.0005	
20	0.10	1.029505	0.000003	8
20	1.13	1.030134	0.000003	12
20	3.29	1.031452	0.000003	3
30	0.10	1.02324	0.00002	25
30	1.13	1.02389	0.00001	22
30	3.29	1.02527	0.00001	11
80	0.10	0.9902	0.0001	20
80	1.13	0.99095	0.00007	19
80	3.29	0.99253	0.00003	10
140	0.10	0.9523	0.0001	10
140	1.13	0.9535	0.0004	20
140	3.29	0.9557	0.0005	14
200	0.10	0.9214	0.0004	6
200	1.13	0.9226	0.0003	10
200	3.29	0.9250	0.0003	9
DMA HP Bitumen Sample 2			0.001	
80	0.10	0.9907	0.0003	34
80	1.13	0.994338	0.000004	7
80	3.29	0.998	0.001	16
140	0.10	0.9537	0.0003	29
140	1.13	0.95673	0.00007	9
140	3.29	0.9604	0.0008	16
200	0.10	0.91690	0.00005	11
200	1.13	0.919	0.001	22
200	3.29	0.924	0.001	15
DMA HP Bitumen Sample 3			0.00004	
80	0.10	0.99338	0.00004	6
80	1.02	0.99383	0.00003	6
80	3.46	0.99530	0.00004	5
140	1.02	0.956492	0.000005	5
140	3.46	0.95832	0.00002	4

Results and Discussion

Density Data

Atmospheric and high-pressure density measurements for Athabasca bitumen, heptane, toluene and water are reported in Tables 2-1 - 2-4. Atmospheric density measurements for Athabasca bitumen + toluene and heptane binaries are reported in Table 2-5. The maximum repeatability deviations are small compared to the values of these measurements. Examples of measurement reproducibility for Athabasca bitumen + 0.127 mass fraction toluene, + 0.094 mass fraction toluene, and 0.07 mass fraction heptane and 0.04 mass fraction heptane at atmospheric pressure are reported in Tables 2-6 – 2-9. The maximum deviation between reproduced measurements using the DMA 5000 is less than 0.0003 g/cm^3. Measurement repeatability for Athabasca bitumen + 0.07 mass fraction heptane at high pressure is illustrated in Table 2-10 and the maximum deviation observed, with numerous repeats is 0.0001 g/cm^3. SAGD produced water chemistry is in Table 2-11. Atmospheric density measurements for SAGD produced water are reported in Table 2-12. The reported values have maximum deviations from one another of 0.006 g/cm^3 and the average values differ from NIST recommended values, for pure water, by less than 0.005 g/cm^3. Mineral salts have a minimal impact on water density for this case but high salt concentrations can increase the density to above that of Athabasca bitumen. These density data and their respective uncertainties provide a basis to test the validity of the ideal mixing assumption for bitumen + toluene and bitumen + heptane mixtures at atmospheric pressure; to identify bitumen + solvent compositions with densities equal to that of water over a range of temperatures at atmospheric pressure; and to capture the effects above atmospheric pressure, and temperatures above 80 °C on the density of mixtures, albeit with a reduced accuracy and precision.

Excess Volumes for Bitumen + Solvent Pseudo Binary Mixtures

For asymmetric and miscible liquid mixtures, large negative excess volumes are anticipated as the critical temperature of the light component is approached. This occurs because the

reduced temperature of the mixture as a whole is low relative to the reduced temperature of the light component and the significant decrease in light component density arising as the critical temperature is approached does not arise in the mixture as a whole. This effect is well known and is built into conventional equation of state models. The normalized excess volumes for squalane + propane binary mixtures expressed as the ratio of the excess volume to the volume and plotted against the ratio of temperature to critical temperature of propane, Figure 2-2, provides an illustrative example. The critical temperature of propane is 96.68 °C and the critical pressure is 4.25 MPa [16]. The excess volume calculations, performed at 1, 4 and 5 MPa and 0.1, 0.2 mass fraction propane using the Advanced Peng Robinson equation of state implemented in VMGSim Process Simulator V7.0 [20], show that the deviation from ideal mixing in the liquid phase is small and stable remote from the propane critical point and becomes large and negative as the critical temperature of the light component is approached. Above a reduced temperature of ~ 0.9 systematic negative deviations from ideal mixing are anticipated even if positive deviations arise at lower reduced temperatures. Such deviations from ideal mixing have been observed for Athabasca bitumen + toluene [12] and for bitumen + pentane [10] mixtures.

Remote from a solvent critical point, non-ideal mixing effects are frequently small, and can be masked by measurement uncertainty. In this work, non ideal mixing is only "observed" if measurement repeatability (a weak test) is applied to the bitumen + toluene and bitumen + heptane pseudo binary mixture density data, as shown in Figures 2-3a and 2-4a, and is not "observed" if measurement reproducibility (a rigorous test) is applied to the data as shown in Figures 2-3b and 2-4b. While every effort was made to minimize the measurement uncertainty associated with bitumen, there is a significant irreducible uncertainty with respect to bitumen density measurement reproducibility. This arises from the complexity of the phase behavior of Athabasca bitumen at room temperature and the existence of polymorphic and thermal history dependent effects that can affect density values [12,17-19, 21]. Consequently, non-ideal mixing effects are masked if the more rigorous test of significance is applied to the data in this work but the general principle is not negated. For asymmetric and miscible liquid mixtures negative volumes of mixing are expected as the light component critical temperature is approached and there is a mixture dependent

upper temperature limit for the validity of the ideal mixing assumption. For example, this assumption is unlikely to be valid above a light component reduced temperature of 0.9, unless the density data possess significant uncertainty.
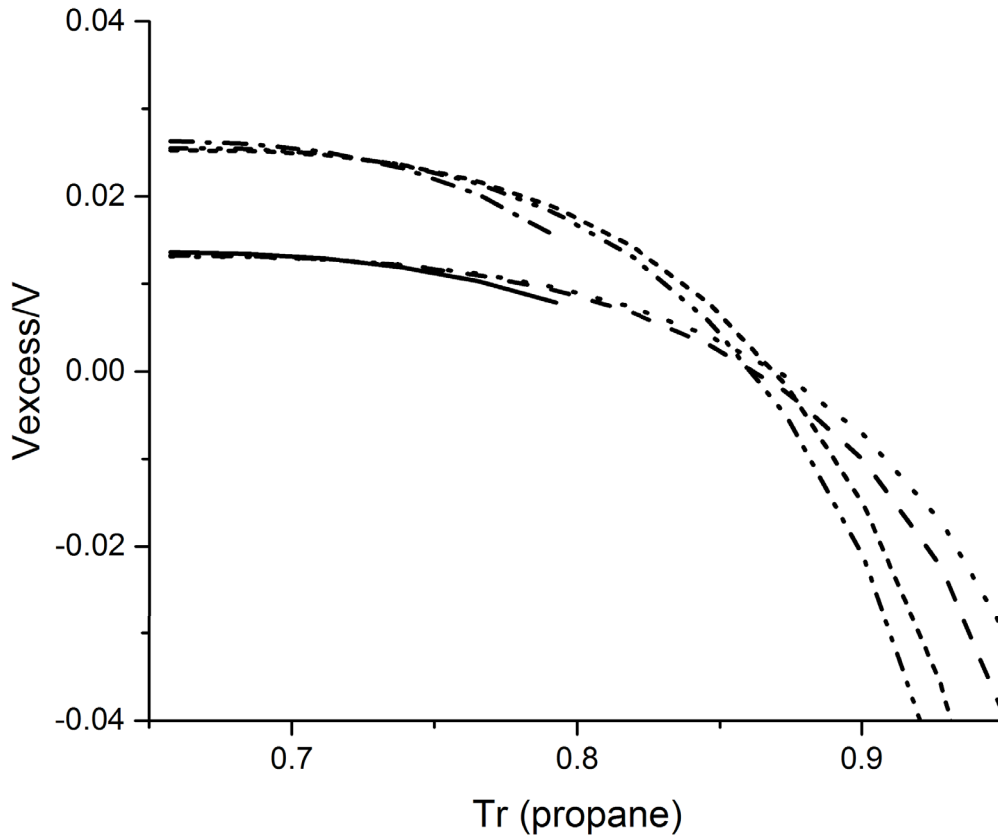
Figure 2-2: Normalized excess volume for squalane + propane binary mixtures: 0.1 mass fraction propane at 1 MPa (————), 4 MPa (▬ ▬ ▬) and 5 MPa (··········); 0.2 mass fraction propane at 1 MPa (▬ · ▬), 4 MPa (▬ · · ▬), and 5 MPa (▬ ▬ ▬), using the Advanced Peng Robinson equation of state in VMGSim Process Simulator V7.0 [20], to calculate component and mixture volumes.

Table 2-5: Density of Athabasca bitumen + toluene and Athabasca bitumen + n-heptane mixtures (DMA 5000)

Temperature (°C)	Solvent mass fraction	Average density (g/cm³)	Max deviation (g/cm³)	Number of repeats
Athabasca bitumen + toluene			0.0002	
20	0.888	0.88232	0.00006	6
20	0.797	0.89525	0.00002	5
20	0.699	0.90980	0.00004	8
20	0.600	0.92515	0.00005	6
20	0.500	0.94088	0.00006	6
20	0.399	0.95730	0.00002	4
20	0.231	0.98538	0.00003	5
20	0.201	0.98983	0.00008	4
20	0.300	0.97360	0.00003	3
30	0.889	0.87323	0.00005	5
30	0.800	0.88621	0.00006	4
30	0.700	0.90127	0.00001	4
30	0.599	0.916920	0.000008	4
30	0.500	0.93287	0.00004	4
30	0.300	0.96657	0.00003	4
30	0.398	0.94974	0.00002	5
30	0.200	0.9839	0.0001	3
80	0.889	0.8272	0.0001	5
80	0.800	0.84157	0.00002	4
80	0.697	0.85876	0.00008	3
80	0.600	0.8755	0.0002	3
80	0.499	0.89337	0.00002	5
80	0.400	0.91134	0.00006	5
80	0.300	0.93005	0.00008	3
80	0.200	0.94969	0.00009	3
Athabasca bitumen + heptane			0.002	
20	0.887	0.7123	0.0004	4
20	0.797	0.737	0.002	5
20	0.700	0.762	0.006	5
20	0.600	0.793	0.002	5
20	0.500	0.8262	0.0001	4
20	0.399	0.86128	0.00008	4
20	0.300	0.89814	0.00006	5
20	0.200	0.938	0.002	4
30	0.889	0.700	0.005	5
30	0.800	0.726	0.004	4
30	0.699	0.752	0.005	4
30	0.600	0.7845	0.0009	4
30	0.499	0.81851	0.00004	4
30	0.399	0.85385	0.00005	4
30	0.300	0.89019	0.00008	4
30	0.200	0.9311	0.0001	5

Table 2-6: Density of Athabasca bitumen + 0.1275 mass fraction toluene and Athabasca bitumen + 0.1271mass fraction toluene (DMA 5000)

Temperature (°C)	Average density (g/cm³)	Maximum deviation between repeats (g/cm³)	Number of repeats	Average density (g/cm³)	Maximum deviation between repeats (g/cm³)	Number of repeats	Deviation between sample averages (g/cm³)
	Bitumen + 0.1275 mass fraction toluene	0.00001		Bitumen + 0.1271 mass fraction toluene	0.00002		0.0002
10				1.00962	0.00002	4	
11				1.00895	0.00002	4	
12				1.00827	0.00002	4	
13				1.00760	0.00002	4	
14				1.00692	0.00002	4	
15	1.00606	0.00001	3	1.00624	0.00002	4	0.0002
16	1.00538	0.00001	3	1.00557	0.00002	4	0.0002
17	1.00471	0.00001	3	1.00490	0.00002	4	0.0002
18	1.00404	0.00001	3	1.00422	0.00002	4	0.0002
19	1.00337	0.00001	3	1.00355	0.00002	4	0.0002
20	1.00270	0.00001	3	1.00287	0.00002	4	0.0002
21	1.00203	0.00001	3	1.00220	0.00002	4	0.0002
22	1.00136	0.00001	3	1.00153	0.00002	4	0.0002
23	1.00069	0.00001	3	1.00086	0.00002	4	0.0002
24	1.00002	0.00001	3	1.00018	0.00001	3	0.0002
25	0.99935	0.00001	3	0.99952	0.00002	4	0.0002
26	0.99868	0.00001	3	0.99884	0.00002	4	0.0002
27	0.99801	0.00001	3	0.99817	0.00002	4	0.0002
28	0.99734	0.00001	3	0.99750	0.00001	4	0.0002
29	0.99668	0.00001	3	0.99683	0.00001	4	0.0002
30	0.99601	0.00001	3	0.99617	0.00001	4	0.0002
31	0.99534	0.00001	3	0.99550	0.00001	4	0.0002
32	0.99467	0.00001	3	0.99483	0.00001	4	0.0002
33	0.99400	0.00001	3	0.99416	0.00001	4	0.0002
34	0.99333	0.00001	3	0.99349	0.00001	4	0.0002
35	0.99267	0.00001	3	0.99282	0.00001	4	0.0002
36	0.99200	0.00001	3	0.99215	0.00001	4	0.0002
37	0.991330	0.000009	3	0.99149	0.00001	4	0.0002
38	0.99066	0.00001	3	0.99082	0.00001	4	0.0002
39	0.99000	0.00001	3	0.99015	0.00001	4	0.0002
40	0.98933	0.00001	3	0.98948	0.00001	4	0.0002
41	0.98866	0.00001	3	0.98882	0.00001	4	0.0002
42	0.987991	0.000009	3	0.98815	0.00001	4	0.0002
43	0.98732	0.00001	3	0.98748	0.00001	4	0.0002
44	0.986656	0.000009	3	0.98682	0.00001	4	0.0002
45	0.98599	0.00001	3	0.98615	0.00001	4	0.0002
46	0.985321	0.000009	3	0.98548	0.00001	4	0.0002
47	0.984653	0.000008	3	0.98482	0.00001	4	0.0002

48	0.983985	0.000009	3	0.98415	0.00001	4	0.0002
49	0.983317	0.000009	3	0.98348	0.00001	4	0.0002
50	0.982649	0.000009	3	0.98282	0.00001	4	0.0002
51	0.981980	0.000009	3	0.98215	0.00001	4	0.0002
52	0.981311	0.000009	3	0.98149	0.00001	4	0.0002
53	0.980642	0.000008	3	0.98082	0.00001	4	0.0002
54	0.979973	0.000008	3	0.98015	0.00001	4	0.0002
55	0.979305	0.000009	3	0.979486	0.000009	4	0.0002
56	0.978634	0.000008	3	0.978818	0.000008	4	0.0002
57	0.977965	0.000008	3	0.978151	0.000010	4	0.0002
58	0.977295	0.000007	3	0.977484	0.000010	4	0.0002
59	0.976623	0.000006	3	0.976816	0.000009	4	0.0002
60	0.975953	0.000007	3	0.976149	0.000009	4	0.0002
61	0.975282	0.000007	3	0.975481	0.000009	4	0.0002
62	0.974610	0.000007	3	0.974813	0.000009	4	0.0002
63	0.973938	0.000006	3	0.974144	0.000008	4	0.0002
64	0.973267	0.000004	3	0.973476	0.000008	4	0.0002
65	0.972615	0.000002	3	0.972808	0.000007	4	0.0002
66	0.971965	0.000001	3	0.972139	0.000008	4	0.0002
67	0.971311	0.000005	3	0.971470	0.000008	4	0.0002
68	0.970658	0.000006	3	0.970801	0.000005	4	0.0001
69	0.970002	0.000007	3	0.970132	0.000007	4	0.0001
70	0.969347	0.000005	3	0.969462	0.000006	4	0.0001
71	0.968690	0.000006	3	0.968794	0.000005	4	0.0001
72	0.968033	0.000002	3	0.968124	0.000006	4	0.00009
73	0.967376	0.000002	3	0.967455	0.000005	4	0.00008
74	0.966720	0.000005	3	0.966786	0.000005	4	0.00007
75	0.966056	0.000002	3	0.966117	0.000004	4	0.00006
76	0.965397	0.000002	3	0.965448	0.000004	4	0.00005
77	0.964737	0.000002	3	0.964779	0.000005	4	0.00004
78	0.964075	0.000002	3	0.964111	0.000005	4	0.00004
79	0.963415	0.000002	3	0.963443	0.000004	4	0.00003
80	0.962755	0.000001	3	0.962774	0.000004	4	0.00002

Table 2-7: Density of Athabasca bitumen + 0.094 mass fraction toluene (DMA 5000)

T (°C)	Average density (g/cm³)	Maximum deviation between repeats (g/cm³)	Repeats	T (°C)	Average density (g/cm³)	Maximum deviation between repeats (g/cm³)	Repeats
		0.00002					
10	1.01618	0.00001	3	46	0.992444	0.000009	3
11	1.01552	0.00002	3	47	0.991790	0.000008	3
12	1.01485	0.00001	3	48	0.991135	0.000008	3
13	1.01419	0.00001	3	49	0.990480	0.000008	3
14	1.01353	0.00001	3	50	0.989825	0.000007	3
15	1.01286	0.00001	3	51	0.989170	0.000008	3
16	1.01220	0.00001	3	52	0.988516	0.000008	3
17	1.01154	0.00001	3	53	0.987861	0.000008	3
18	1.01087	0.00001	3	54	0.987207	0.000008	3
19	1.01021	0.00001	3	55	0.986553	0.000006	3
20	1.00955	0.00001	3	56	0.985899	0.000007	3
21	1.00889	0.00001	3	57	0.985243	0.000007	3
22	1.00823	0.00001	3	58	0.984590	0.000006	3
23	1.00757	0.00001	3	59	0.983936	0.000006	3
24	1.00691	0.00001	3	60	0.983281	0.000006	3
25	1.00625	0.00001	3	61	0.982626	0.000007	3
26	1.00559	0.00001	3	62	0.981972	0.000006	3
27	1.00493	0.00001	3	63	0.981318	0.000005	3
28	1.00427	0.00001	3	64	0.980663	0.000004	3
29	1.00361	0.00001	3	65	0.980009	0.000005	3
30	1.00295	0.00001	3	66	0.979353	0.000007	3
31	1.00229	0.00001	3	67	0.978698	0.000006	3
32	1.00164	0.00001	3	68	0.978043	0.000004	3
33	1.00098	0.00001	3	69	0.977388	0.000003	3
34	1.00032	0.00001	3	70	0.976732	0.000005	3
35	0.99966	0.00001	3	71	0.976076	0.000005	3
36	0.99900	0.00001	3	72	0.975420	0.000004	3
37	0.99835	0.00001	3	73	0.974763	0.000004	3
38	0.99769	0.00001	3	74	0.974107	0.000003	3
39	0.99703	0.00001	3	75	0.973450	0.000003	3
40	0.99638	0.00001	3	76	0.972793	0.000003	3
41	0.99572	0.00001	3	77	0.972136	0.000002	3
42	0.99507	0.00001	3	78	0.971480	0.000003	3
43	0.994411	0.000009	3	79	0.970839	0.000003	3
44	0.993754	0.000009	3	80	0.970199	0.000005	3
45	0.993100	0.000008	3				

Table 2-8: Density of Athabasca bitumen + 0.0701 mass fraction heptane and Athabasca bitumen + 0.0700 mass fraction heptane (DMA 5000)

Temperature (°C)	Average density (g/cm³)	Maximum deviation between repeats (g/cm³)	Number of repeats	Average density (g/cm³)	Maximum deviation between repeats (g/cm³)	Number of repeats	Deviation between samples average (g/cm³)
	Bitumen + 0.0701 mass fraction heptane	0.00002		Bitumen + 0.0700 mass fraction heptane	0.00002		0.0003
10				1.0007		1	
11				1.0001		1	
12				0.9994		1	
13				0.9987		1	
14				0.9981		1	
15	0.99775	0.00002	3	0.99745	0.00002	3	0.0003
16	0.99710	0.00002	2	0.99679	0.00002	3	0.0003
17	0.99645	0.00002	2	0.99614	0.00002	3	0.0003
18	0.99580	0.00002	2	0.99548	0.00002	3	0.0003
19	0.99514	0.00002	2	0.99483	0.00002	3	0.0003
20	0.99449	0.00002	3	0.99417	0.00002	3	0.0003
21	0.99384	0.00002	2	0.99352	0.00001	3	0.0003
22	0.99319	0.00002	2	0.99287	0.00001	3	0.0003
23	0.99254	0.00002	2	0.99221	0.00001	3	0.0003
24	0.99189	0.00001	2	0.991562	0.000009	3	0.0003
25	0.99124	0.00001	3	0.990910	0.000010	3	0.0003
26	0.99059	0.00002	2	0.990258	0.000009	3	0.0003
27	0.98994	0.00001	2	0.989606	0.000010	3	0.0003
28	0.98929	0.00001	2	0.988955	0.000009	3	0.0003
29	0.98864	0.00001	2	0.988304	0.000009	3	0.0003
30	0.98799	0.00001	3	0.987654	0.000009	3	0.0003
31	0.98734	0.00001	2	0.987004	0.000009	3	0.0003
32	0.98669	0.00001	2	0.986354	0.000009	3	0.0003
33	0.98604	0.00001	2	0.985703	0.000008	3	0.0003
34	0.98539	0.00001	2	0.985054	0.000008	3	0.0003
35	0.98474	0.00001	3	0.984405	0.000008	3	0.0003
36	0.98410	0.00001	2	0.983756	0.000008	3	0.0003
37	0.98345	0.00001	2	0.983107	0.000008	3	0.0003
38	0.98280	0.00001	2	0.982459	0.000007	3	0.0003
39	0.98215	0.00001	2	0.981810	0.000007	3	0.0003
40	0.98150	0.00001	3	0.981163	0.000007	3	0.0003
41	0.98086	0.00001	2	0.980515	0.000007	3	0.0003
42	0.98021	0.00001	2	0.979868	0.000007	3	0.0003
43	0.97956	0.00001	2	0.979221	0.000006	3	0.0003
44	0.97891	0.00001	2	0.978574	0.000006	3	0.0003
45	0.97826	0.00001	3	0.977927	0.000006	3	0.0003
46	0.97762	0.00001	2	0.977281	0.000006	3	0.0003
47	0.97697	0.00001	2	0.976635	0.000006	3	0.0003

48	0.97632	0.00001	2	0.975990	0.000006	3	0.0003
49	0.97568	0.00001	2	0.975343	0.000006	3	0.0003
50	0.97503	0.00001	3	0.974698	0.000006	3	0.0003
51	0.97438	0.00001	2	0.974053	0.000005	3	0.0003
52	0.97373	0.00001	2	0.973408	0.000005	3	0.0003
53	0.97309	0.00001	2	0.972764	0.000005	3	0.0003
54	0.97244	0.00001	2	0.972119	0.000005	3	0.0003
55	0.971794	0.000009	3	0.971474	0.000005	3	0.0003
56	0.971148	0.000009	2	0.970830	0.000006	3	0.0003
57	0.970502	0.000008	2	0.970185	0.000004	3	0.0003
58	0.969855	0.000008	2	0.969542	0.000004	3	0.0003
59	0.969209	0.000009	2	0.968898	0.000004	3	0.0003
60	0.968561	0.000008	3	0.968255	0.000004	3	0.0003
61	0.967916	0.000008	2	0.967611	0.000004	3	0.0003
62	0.967269	0.000007	2	0.966967	0.000003	3	0.0003
63	0.966623	0.000007	2	0.966323	0.000003	3	0.0003
64	0.965976	0.000007	2	0.965680	0.000002	3	0.0003
65	0.965329	0.000006	3	0.965038	0.000003	3	0.0003
66	0.964683	0.000007	2	0.964393	0.000002	3	0.0003
67	0.964036	0.000006	2	0.963751	0.000003	3	0.0003
68	0.963389	0.000007	2	0.963107	0.000002	3	0.0003
69	0.962741	0.000006	2	0.962464	0.000002	3	0.0003
70	0.962093	0.000005	3	0.961821	0.000002	3	0.0003
71	0.961446	0.000005	2	0.961178	0.000002	3	0.0003
72	0.960798	0.000005	2	0.960534	0.000002	3	0.0003
73	0.960150	0.000005	2	0.959890	0.000001	3	0.0003
74	0.959502	0.000005	2	0.959247	0.000002	3	0.0003
75	0.958853	0.000004	3	0.958603	0.000001	3	0.0002
76	0.958203	0.000004	2	0.957959	0.000001	3	0.0002
77	0.957554	0.000004	2	0.957314	0.000001	3	0.0002
78	0.956905	0.000003	2	0.956669	0.000001	3	0.0002
79	0.956254	0.000003	2	0.956025	0.000002	3	0.0002
80	0.955605	0.000003	3	0.955380	0.000001	3	0.0002

Table 2-9: Density of Athabasca bitumen + 0.040 mass fraction heptane (DMA 5000).

T (°C)	Average density (g/cm³)	Maximum deviation between repeats (g/cm³)	Number of repeats	T (°C)	Average density (g/cm³)	Maximum deviation between repeats (g/cm³)	Number of repeats
		0.00001					
10	1.01484	0.00001	3	46	0.991769	0.000007	3
11	1.01420	0.00001	3	47	0.991132	0.000006	3
12	1.01355	0.00001	3	48	0.990496	0.000008	3
13	1.01291	0.00001	3	49	0.989859	0.000007	3
14	1.01227	0.00001	3	50	0.989223	0.000007	3
15	1.01162	0.00001	3	51	0.988587	0.000006	3
16	1.01098	0.00001	3	52	0.987951	0.000006	3
17	1.01034	0.00001	3	53	0.987316	0.000006	3
18	1.00969	0.00001	3	54	0.986680	0.000005	3
19	1.00905	0.00001	3	55	0.986045	0.000006	3
20	1.00841	0.00001	3	56	0.985409	0.000006	3
21	1.00776	0.00001	3	57	0.984774	0.000006	3
22	1.00712	0.00001	3	58	0.984140	0.000005	3
23	1.00648	0.00001	3	59	0.983505	0.000005	3
24	1.00584	0.00001	3	60	0.982871	0.000004	3
25	1.005196	0.000009	3	61	0.982237	0.000005	3
26	1.004554	0.000009	3	62	0.981602	0.000004	3
27	1.003913	0.000008	3	63	0.980969	0.000004	3
28	1.003271	0.000008	3	64	0.980334	0.000004	3
29	1.002630	0.000009	3	65	0.979701	0.000005	3
30	1.001990	0.000009	3	66	0.979068	0.000005	3
31	1.001348	0.000008	3	67	0.978434	0.000004	3
32	1.000709	0.000009	3	68	0.977800	0.000004	3
33	1.000069	0.000008	3	69	0.977167	0.000004	3
34	0.999429	0.000009	3	70	0.976534	0.000004	3
35	0.998790	0.000008	3	71	0.975901	0.000004	3
36	0.998149	0.000007	3	72	0.975268	0.000003	3
37	0.997512	0.000008	3	73	0.974635	0.000003	3
38	0.996872	0.000007	3	74	0.974003	0.000003	3
39	0.996234	0.000007	3	75	0.973370	0.000003	3
40	0.995595	0.000008	3	76	0.972737	0.000003	3
41	0.994957	0.000008	3	77	0.972104	0.000002	3
42	0.994319	0.000007	3	78	0.971472	0.000003	3
43	0.993681	0.000007	3	79	0.970838	0.000002	3
44	0.993043	0.000006	3	80	0.970205	0.000002	3
45	0.992406	0.000007	3				

Table 2-10: Density of Athabasca bitumen + 0.0701 mass fraction heptane at elevated pressures

Temperature (°C)	Average pressure (MPa)	Average density (g/cm³)	Maximum deviation between repeats (g/cm³)	Number of repeats
Bitumen + 0.0701 mass fraction heptane			0.0001	
30	0.10	0.98946	0.00001	8
30	1.11	0.990586	0.000004	11
30	3.29	0.991746	0.000004	7
80	0.10	0.95667	0.00006	24
80	1.11	0.95795	0.00005	13
80	3.29	0.959384	0.000007	7
140	0.10	0.91791	0.00003	6
140	1.11	0.91873	0.00002	7
140	3.29	0.9209	0.0001	11
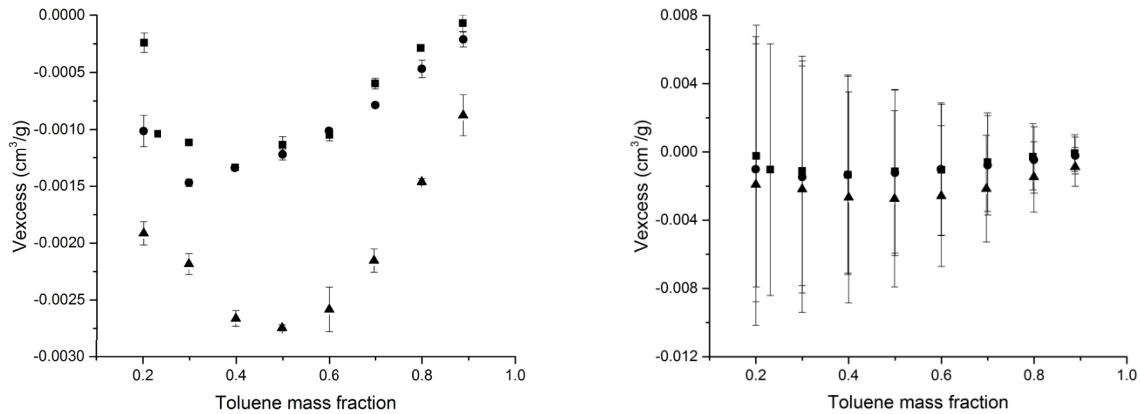
Figure 2-3: Excess volume for Athabasca Bitumen + toluene mixtures at 20°C (■), 30°C (●), and 80°C (▲) based on: a) density measurement repeatability b) density measurement reproducibility.
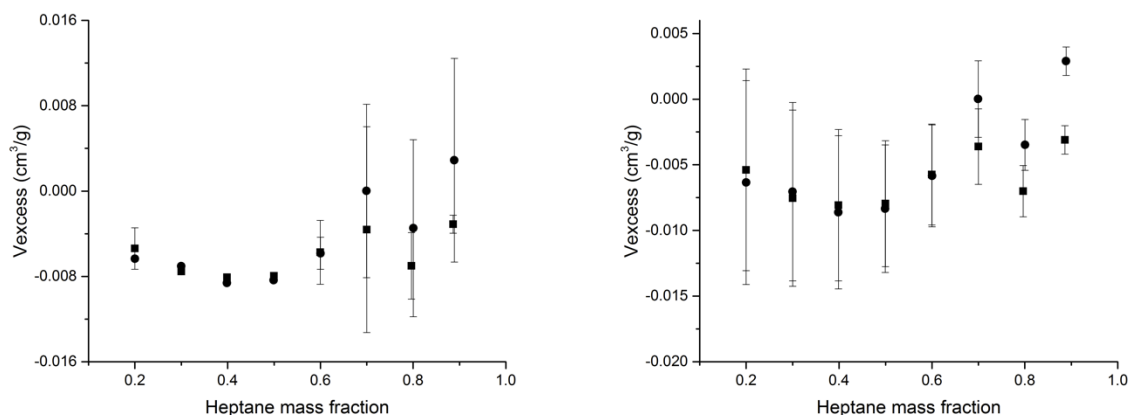
Figure 2-4: Excess volume for Athabasca Bitumen + heptane mixtures at 20°C (■) and 30°C (●) based on: a) density measurement repeatability, b) density measurement reproducibility.

Phase Order Inversion for Bitumen + Solvent Pseudo Binary Mixtures and Water

Illustrative examples for Athabasca bitumen + toluene and heptane mixtures are shown in Figures 2-5 and 2-6 at atmospheric and elevated pressures respectively. Measured densities of the hydrocarbon phase are compared with density values for NIST water [16] at the same conditions in both figures, and points of intersection are identified. From Figure 2-5 one observes that at atmospheric pressure the density of the Athabasca bitumen + toluene (0.127 mass fraction) mixture intersects the density of water at approximately 30°C, while the density of the Athabasca bitumen + heptane (0.07 mass fraction) mixture the density of water at approximately 10°C. These intersection temperatures provide points on the phase inversion envelopes presented in this work. At high pressures, Figure 2-6, the density of mixtures with the same compositions approach the density of water from below and a second inversion is expected for both mixtures at a temperature below 200°C due to the approximately linear density trajectory of the Athabasca bitumen + solvent mixtures observed in Figures 2-5 and 2-6. Thus, Athabasca bitumen + solvent mixtures may be more dense than water at low temperature, less dense at intermediate temperatures and more dense than water at high temperatures. As the densities of produced water, DIUF water and NIST water differ little, as shown in Table 2-12 and elsewhere [10], the impact of dissolved

32

mineral matter has a minimal effect on water density and hence the inversion temperature values. Thus, the observed trends are robust with respect to water composition.

Phase Order Inversion Envelope Construction

The loci of points where the densities of the water-rich and hydrocarbon-rich liquid phases intersect comprise phase order inversion envelopes. As phase densities and the relative density of phases change with pressure, phase inversion envelopes are most conveniently presented as functions of temperature at fixed values of pressure. Points can be identified directly by experiment, as illustrated in Figures 2-5 and 2-6, by regressing or interpolating experimental density data adjacent to points of intersection, or by imposing a model on a set of data as a whole. The last approach was adopted here because the number of experimental measurements is limited, and because the ideal mixing assumption was shown to be justified within the uncertainty of the data. However, other approaches are tenable [19]. The phase inversion envelopes for Athabasca bitumen + toluene (Figure 2-7) and Athabasca bitumen + heptane (Figure 2-8) with water were constructed on the basis of Agamat's Law, Equation 2-1, where the inverse density of a mixture is a mass fraction (x_i) weighted sum of the inverse densities (ρ_i) of the constituents:

$$\frac{1}{\rho_{mixture}} = \sum \frac{x_i}{\rho_i}$$

Equation 2-1

The density of Athabasca bitumen was regressed from experimental data in Tables 2-3 and 2-4 as:

$$\rho_{bitumen} = AT + B$$

Equation 2-2

where the pressure dependent coefficients A and B for the density (g/cm^3) of Athabasca Bitumen are given in Table 2-13 and temperature is expressed in °C. As the measured density values for toluene and heptane differed little from the recommended values from

33

NIST [16], Tables 2-1 and 2-2, the NIST recommended values were used to construct phase inversion envelopes.

Points on the phase inversion envelope arise where the hydrocarbon mixture density and the water density are equal. By combining this constraint with Equations 2-1 and 2-2, an expression for solvent mass fraction ($x_{solvent}$) at points of intersection is obtained:

$$x_{solvent} = \frac{\left(\frac{1}{\rho_{water}} \rho_{bitumen} \rho_{solvent} - \rho_{solvent} \right)}{\left(\rho_{bitumen} - \rho_{solvent} \right)}$$
<div align="right">**Equation 2-3**</div>

The impact of hydrocarbon solubility, typically measured at the ppm level [22] and the impact of inorganic salts on water density is ignored in Equation 2-3. NIST [16] recommended values for water density are used in the calculations.

The phase order inversion envelopes reported in Figures 2-7 and 2-8 each include four sets of envelope calculations. Two (one based on regressed bitumen density values obtained with the DMA 5000, and the other based on bitumen density values obtained with the DMA HP unit) are for atmospheric pressure. These envelopes have an upper temperature limit of 100°C, because water vapour and not water liquid is stable above this temperature. One envelope is for 1.1 MPa. This envelope terminates at 170 °C, again because water vaporizes. The fourth envelope is for 3.29 MPa and it is truncated at a reduced temperature of 0.85 for each solvent, 230 °C for Athabasca bitumen + toluene (critical temperature 318 °C [16]) and at 185 °C for Athabasca bitumen + heptane (critical temperature 267 °C [16]) because the ideal mixing assumption is expected to break down as the critical point of the light hydrocarbon is approached. These envelopes comprise the thick curves in Figures 2-7 and 2-8. The corresponding thin curves to the right and left reflect the impact of Athabasca bitumen density measurement reproducibility on envelope placement. The envelopes can shift systematically by up to +/- 0.05 mass fraction toluene and by up to +/- 0.02 mass fraction heptane respectively from the mean boundary composition values based on the measurement reproducibility uncertainty for Athabasca bitumen. Measured points on the

phase inversion envelopes are also included in the Figures. For compositions on the left of the envelopes, the hydrocarbon-rich phase is denser than the water-rich phase, and for compositions on the right, the water-rich phase is denser than the hydrocarbon–rich phase.

The phase inversion envelopes for the two Athabasca bitumen + solvent mixtures are qualitatively similar: both Athabasca bitumen + solvent mixtures possess a range of composition values that invert twice as temperature is increased; at fixed temperature, compositions at which inversion occurs are pressure insensitive; at temperatures approaching the critical temperature of the solvent negative volumes of mixing are expected and consequently the envelopes are encountered at higher solvent mass fractions than anticipated by ideal mixing. These features of the phase envelopes would also be shared with other solvents and the method for preparing phase order inversion envelopes and the observed outcomes are readily extended from heptane to lower alkanes (hexane, pentane, butane) where based on the same assumptions the envelopes are qualitatively similar but where even lower mass fractions are needed to cause inversion and the zones where the hydrocarbon-rich phase is more dense than the water-rich phase are correspondingly smaller, or to larger alkanes where the reverse arises. The outcomes for toluene are equally generalizable and equivalent. Low-density miscible liquids induce phase order inversion.

Density data from Amani et al. [12] for Athabasca bitumen + 0.000, 0.448, 0.667 mass fraction toluene at 200 to 300 °C, were interpolated, using a quadratic function, to obtain points on the phase inversion envelope and these values are compared to calculations performed using Equation 2-1 – 2-3 to test whether the ideal mixing assumption holds for bitumen + toluene mixtures at temperatures higher than can be reached using the DMA HP. For the ideal mixing calculations, the Athabasca bitumen density data from Amani et al. [19] were used. NIST [16] recommended values for toluene were used. The impact of pressure on bitumen density and on envelope placement was ignored. The published uncertainty in Amani et al.'s measurements of Athabasca bitumen and Athabasca bitumen + toluene were used to calculate the maximum uncertainty in the phase inversion. Points on the phase inversion envelope were determined using the density of liquid water from NIST

[16] at the same temperature and pressure. The outcomes of these calculations are shown in Figure 2-9. The interpolated values based on experimental data and values computed on the basis of ideal mixing overlap within the uncertainty of the measurements. However, the computed values systematically trend to underestimation, as expected, as the critical temperature of toluene is approached. Nonetheless, the calculations suggests that the ideal mixing assumption can be used to predict the phase inversion envelopes up to reduced temperatures exceeding 0.9, at least for this one case, where potential impacts of non-ideal mixing are masked by measurement uncertainty.
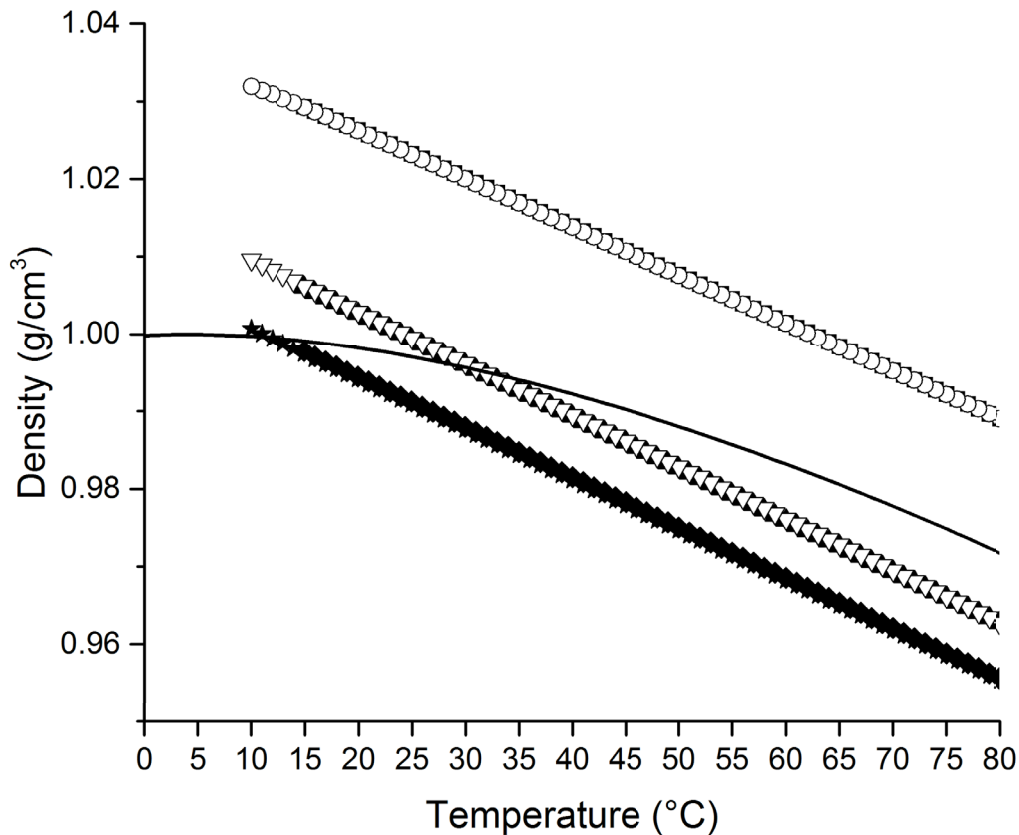
Figure 2-5: Density of bitumen and bitumen + solvent mixtures measured using the DMA 5000 relative to NIST water at 0.10 MPa (—) [16]. Athabasca bitumen sample 1 (■), sample 2 (O); Athabasca bitumen + 0.1275 mass fraction toluene (▲); Athabasca bitumen + 0.1271 mass fraction toluene (▽); Athabasca bitumen + 0.0701 mass fraction heptane (◆); Athabasca bitumen + 0.070 mass fraction heptane (★).
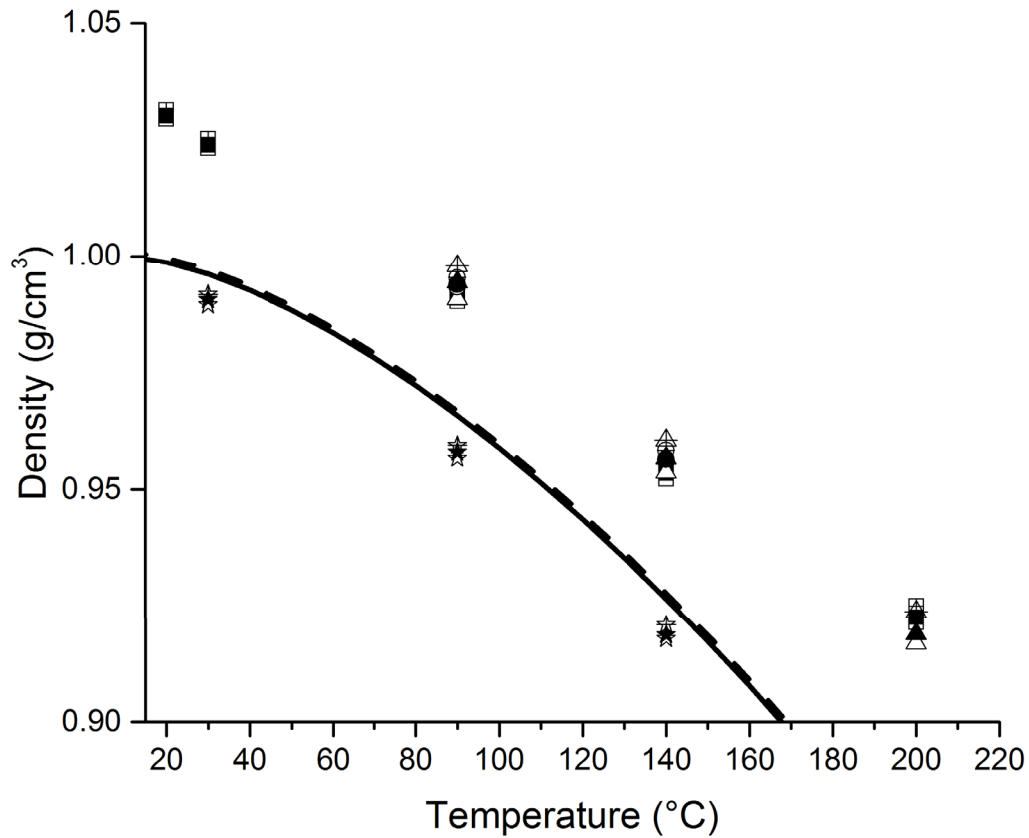
Figure 2-6: Illustrative comparison of bitumen and bitumen + solvent mixture density data obtained using DMA HP relative to the density of water (NIST recommended values) at 1.12 MPa (——) and 3.29 MPa (– –)[16]. Athabasca bitumen sample 1 at 0.10 MPa (□), 1.13 MPa (■) and 3.29 MPa (⊞); Athabasca bitumen sample 2 at 0.10 MPa (△), 1.13 MPa (▲) and 3.29 MPa (⟁); Athabasca bitumen sample 3 at 0.10 MPa (○), 1.02 MPa (●), and 3.46 MPa (⊕); Athabasca bitumen + 0.0701 mass fraction heptane at 0.10 MPa(☆), 1.11 MPa (★), 3.29 MPa (⛤).

Table 2-11: SAGD produced water chemical analysis. Completed by Wilson Analytics Inc., Sherwood Park, Alberta.

Method	Analysis	Units	Result
Classical	Alkalinity, Total	mg/L	383
Classical	Bicarbonate	mg/L	467
Classical	Carbonate	mg/L	<1
Classical	Chloride	mg/L	1085
Classical	pH	N/A	5.34
Spectroscopy	Barium	mg/L	<2
Spectroscopy	Calcium	mg/L	5.7
Spectroscopy	Magnesium	mg/L	<0.4
Spectroscopy	Potassium	mg/L	33
Spectroscopy	Sodium	mg/L	917
Spectroscopy	Strontium	mg/L	0.3
Spectroscopy	Sulphate	mg/L	108
Spectroscopy	Iron*	mg/L	<0.5
Spectroscopy	Manganese*	mg/L	<0.1
Picnometer	Specific gravity		1
Calculation	Cation Sum	mEq/L	41.14
Calculation	Anion Sum	mEq/L	40.47
Calculation	Ion Balance (Cation/Anion)		1.02
Calculation	Ion Balance (% difference)		0.82
Calculation	Total Dissolved Solids	mg/L	2380

*Note: Sample not acidified.

Table 2-12: Density of SAGD produced water compared to NIST recommended values for water

Temperature (°C)	Average density (g/cm³)	Deviation from NIST water (g/cm³)	Maximum deviation between repeats (g/cm³)	Number of repeats
Shell Orion Prod. Water		0.005	0.006	
20	1.000	0.002	0.006	3
40	0.994	0.002	0.00003	3
60	0.984	0.001	0.003	8
80	0.967	-0.005	0.003	5

Table 2-13: Coefficients for Equation 2-2 Athabasca bitumen density (ρ=AT+B in g/cm^3)

Data set	A (g/cm^3/°C)	B (g/cm^3)	Max deviation from data (g/cm^3)
0.10 MPa (DMA 5000 Sample 2)	-6.184x10^{-4}	1.0386	0.002
0.10 MPa (DMA HP Sample 1)	-6.080x10^{-4}	1.0408	0.005
1.13 MPa (DMA HP Sample 1)	-6.047x10^{-4}	1.0417	0.005
3.29 MPa (DMA HP Sample 1)	-5.981x10^{-4}	1.0431	0.004
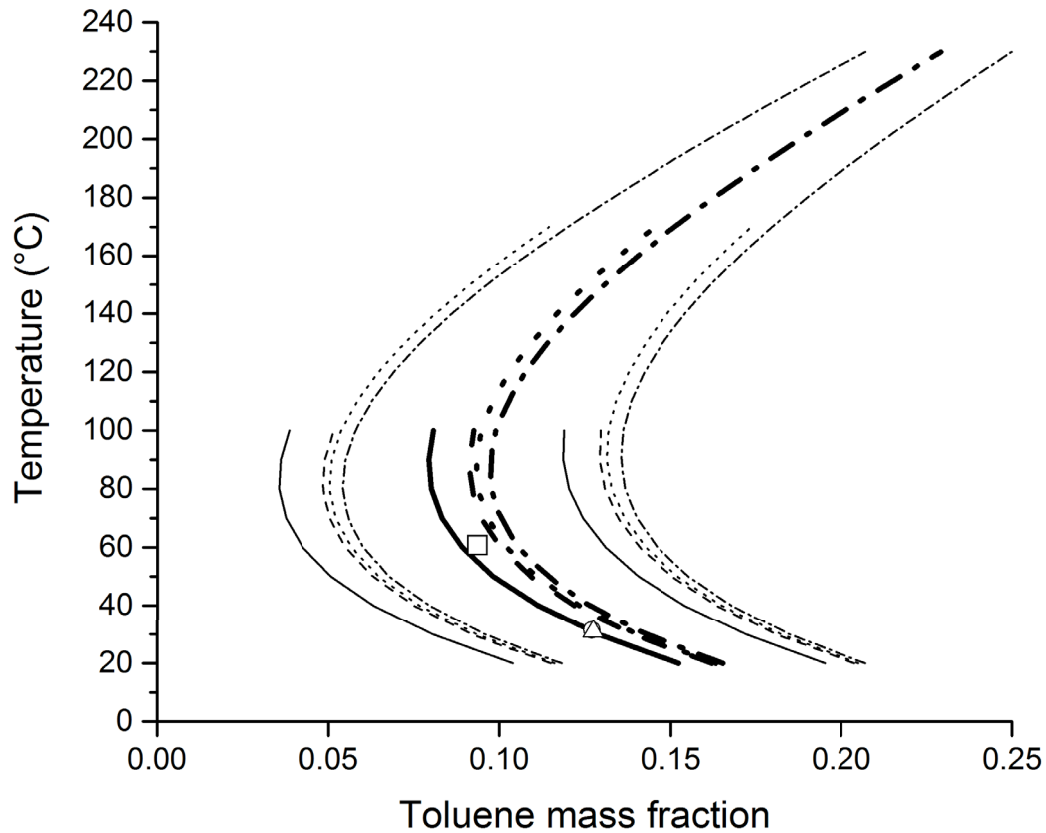
Figure 2-7: Phase inversion envelopes for Athabasca bitumen + toluene + water mixtures at 0.1 MPa based on data from the DMA 5000 (————), and at 0.10 MPa (− − −), 1.13 MPa (▬▬▬) and 3.29 MPa (▬ · ▬) based on data from the DMA HP. The corresponding lighter curves reflect the maximum uncertainty associated with the bitumen density reproducibility. Measured points on the phase inversion boundaries are also shown at 0.10 MPa based on data from the DMA 5000 for 0.094 (□), 0.1271 (○) and 0.1275 (△) mass fraction toluene.
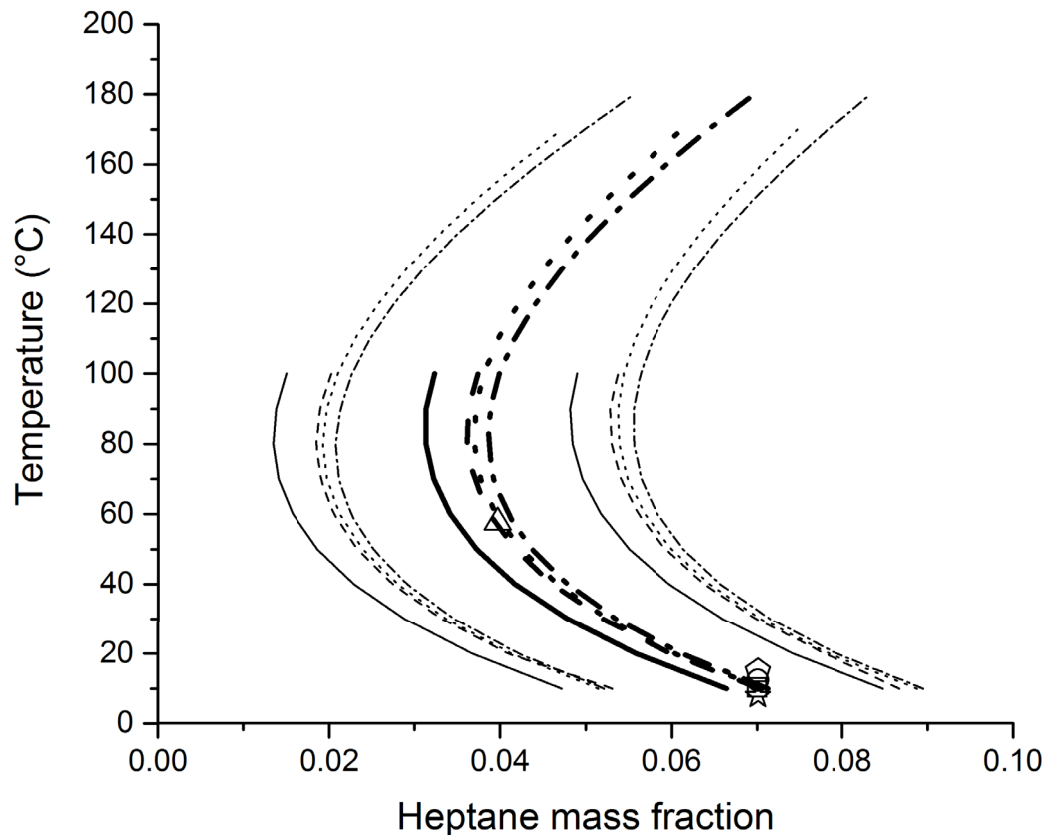
Figure 2-8: Phase inversion envelopes for Athabasca bitumen + heptane + water mixtures at 0.1 MPa based on data from the DMA 5000 (————) and at 0.10 MPa (– – –), 1.13 MPa (▬▬▬▬) and 3.29 MPa (▬ · ▬) based on data from the DMA HP. The corresponding lighter curves reflect the maximum uncertainty associated with the bitumen density reproducibility. Measured points on the phase inversion boundaries are also shown at 0.10 MPa based on data from the DMA 5000 for 0.0700 (□), 0.0701 (○), 0.040 (△) mass fraction heptane and based on data from the DMA HP for 0.0701 mass fraction heptane at 0.10 MPa (⬠), 1.11 MPa (☆) and 3.29 MPa (⬡).
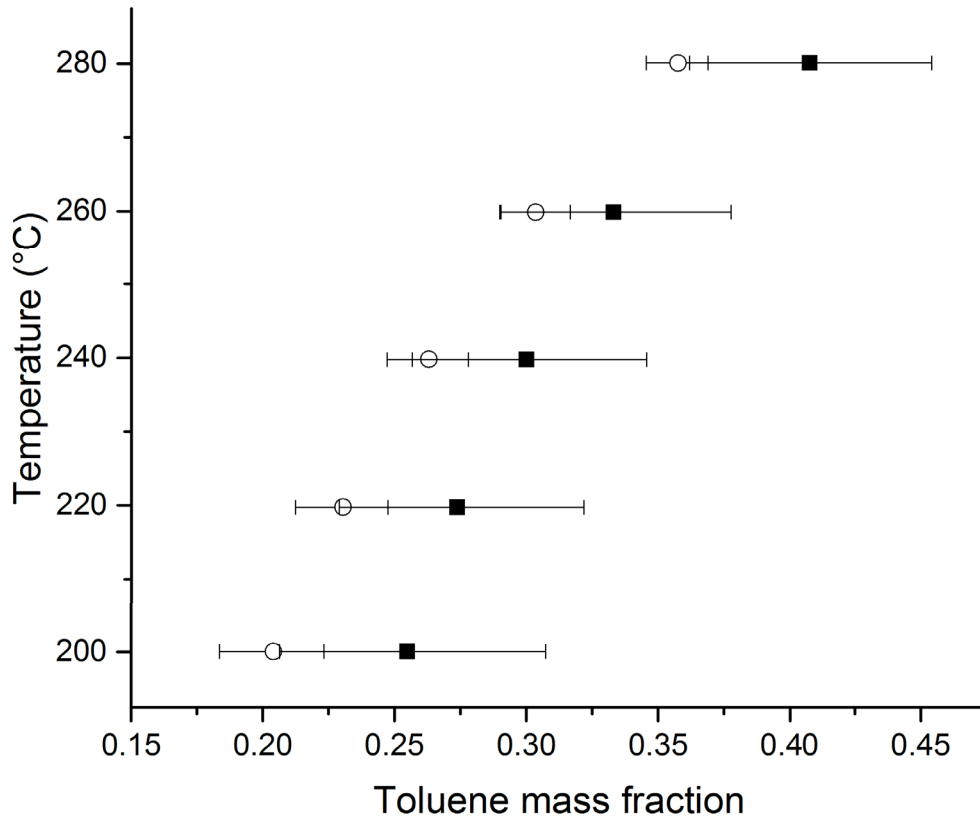
Figure 2-9: Pressure independent phase inversion boundary for Athabasca bitumen + toluene interpolated from mixture data (■) and calculated from component data assuming ideal mixing at comparable conditions (○) based on data from Amani [12].

Implications for Heavy Oil and Bitumen Production Processes

Phase order inversion is sensitive to fluid properties. Small changes in relative fluid properties, either more dense water i.e.: water with high solute concentrations; or less dense hydrocarbons, may not exhibit phase order inversion. Solvents are not essential. For example, phase order inversion has been observed for a heavy oil sample on its own at near ambient conditions [15]. It is also possible to imagine reservoirs with thermal gradients where two-phase convective currents are formed due to phase order inversion. The illustrations in the present work provide a simple framework for the calculation of

conditions leading to phase order inversion for specific denser-than-water hydrocarbon resources, and the potential for this phenomenon to impact the design or performance of processes for their production, transport and refining.

In conventional SAGD operations, the density of bitumen remains greater than that of connate water and condensed steam.   This fore knowledge facilitated the conceptual development of this process. Phase order inversion of the hydrocarbon rich and water rich phases by changing the hydrocarbon-rich phase composition introduces an additional and uncontrolled variable in the gravity drainage process, both in the reservoir and in surface facilities. As only small mass fractions of solvent are needed to cause phase order inversion, it is readily realized if miscible liquids are present as demonstrated above, or if light hydrocarbons are dissolved into the denser-than-water hydrocarbon reservoir fluid from the gas phase. As composition is not controlled in reservoirs, spatial variation in relative phase density arises, and production systems set up on the basis of conventional SAGD operation may not operate according to expectation. Understanding and controlling the compositions and conditions where phase inversion occurs could lead to the development of new production methods or variants but avoidance of phase inversion would appear to be preferred over relying on kinetic or hydrodynamic effects that may mitigate the impact of phase density inversion. One option is the introduction of hydrocarbon resource soluble gases that under the conditions applied do not induce liquid phase density inversion at saturation. However both pore level and reservoir level effects are anticipated. Phase order inversion adds to the complexity of the already complex added solvent production processes where steam condensation, which transfers heat to the hydrocarbon resource, must occur separately in time or space from dissolution of solvent in the resource, because liquid water is a barrier to solvent mass transfer.

Conclusions

The densities of hydrocarbon resources such as heavy oil and bitumen are typically greater than the density of both pure liquid water and liquid water found in reservoirs. Addition of low molar mass solvents to facilitate production as currently envisioned by the petroleum industry, leads to an inversion in the phase order over a broad range of pressures and temperatures even if only a small mass fraction of solvent is added to the hydrocarbon resource. Phase inversion envelopes for Athabasca bitumen + heptane and toluene illustrate the principle, and the qualitative outcomes, including composition ranges exhibiting two inversion temperatures at fixed pressure and the pressure insensitivity to envelope placement in the phase diagram, are generalizable to other solvents. While it is well known that the excess volumes for miscible asymmetric liquid mixtures are negative as the critical point of the lighter component is approached, excess volumes for Athabasca bitumen + toluene and heptane mixtures, can be assumed to be zero within experimental uncertainty over broad ranges of conditions due to irreducible deviations arising in the Athabasca bitumen density measurements that mask potential non-ideal mixing effects. The impact of non-ideal mixing on phase envelope placement is expected to be significant and systematic, in general, above a reduced temperature for the solvent of 0.9. Possible impacts of these findings on the ongoing development of techniques for the production of denser-than-water hydrocarbon resources and related applications are subjects of ongoing investigation.

Acknowledgements

References

[1]   R. M. Butler, G. S. Mcnab, and H. Y. Lo, "Theoretical Studies on the Gravity Drainage of Heavy Oil during In-situ Steam Heating," *The Canadian Journal of Chemical Engineering*, vol. 59, no. August, pp. 455–460, 1981.

[2]   B. Rostami, R. Kharrat, M. Pooladi-Darvish, and C. Ghotbi, "Identification of Fluid Dynamics in Forced Gravity Drainage Using Dimensionless Groups," *Transport in Porous Media*, vol. 83, no. 3, pp. 725–740, Nov. 2009.

[3]   C. Yang and Y. Gu, "Effects of Heavy-Oil / Solvent Interfacial Tension on Gravity Drainage in the Vapor Extraction (Vapex) Process," in *SPE/PS-CIM/CHOA International Thermal Operations and Heavy Oil Symposium*, 2005.

[4]   A. Firoozabadi and K. Ishimoto, "Reinfiltration in Fractured Porous Media: Part 1 - One Dimentional Model," *SPE Advanced Technology Series*, vol. 2, no. 2, pp. 35–44, 1994.

[5]   A. Firoozabadi, K. Ishimoto, and B. Dindoruk, "Reinfiltration in Fractured Porous Media: Part 2 - Two Dimentional Model," *SPE Advanced Technology Series*, vol. 2, no. 2, pp. 45–51, 1994.

[6]   S. Gupta, S. Gittins, A. Sood, K. Zeidani, and C. Energy, "Optimal Amount of Solvent in Solvent Aided Process," in *Canadian Unconventional Resources & International Petroleum Conference*, 2010, no. October, pp. 19–21.

[7]   A. Badamchi-Zadeh, H. Yarranton, W. Svrcek, and B. Maini, "Phase Behaviour and Physical Property Measurements for VAPEX Solvents: Part I. Propane and Athabasca Bitumen," *Journal of Canadian Petroleum Technology*, vol. 48, no. 1, Jan. 2009.

[8]   A. Badamchi-Zadeh, H. Yarranton, B. Maini, and M. Satyro, "Phase Behaviour and Physical Property Measurements for VAPEX Solvents: Part II. Propane, Carbon Dioxide and Athabasca Bitumen," *Journal of Canadian Petroleum Technology*, vol. 48, no. 3, Mar. 2009.

[9]   A. K. Mehrotra and W. Y. Svrcek, "Viscosity, Density and Gas Solubility Data for Oil Sand Bitumens. Part II: Peace River Bitumen Saturated with N2, CO, CH4, CO2 and C2H6," *AOSTRA Journal of Research*, vol. 1, no. 4, pp. 269–279, 1985.

[10]   F. J. Arguelles-Vivas, T. Babadagli, L. Little, N. Romaniuk, and B. Ozum, "High Temperature Density , Viscosity , and Interfacial Tension Measurements of Bitumen – Pentane – Biodiesel and Process Water Mixtures," *Journal of Chemical & Engineering Data*, vol. 57, pp. 2878–2889, 2012.

[11]   J. G. Guan, M. Kariznovi, H. Nourozieh, and J. Abedi, "Density and Viscosity for Mixtures of Athabasca Bitumen and Aromatic Solvents," *Journal of Chemical & Engineering Data*, vol. 58, no. 3, pp. 611–624, Mar. 2013.

[12]   M. J. Amani, M. R. Gray, and J. M. Shaw, "The Phase Behavior of Athabasca Bitumen + Toluene + Water Ternary Mixtures," *Fluid Phase Equilibria*, Mar. 2014.

[13]   H. Motahhari, F. F. Schoeggl, and M. A. Satyro, "Prediction of the Viscosity of Solvent Diluted Live Bitumen at Temperatures up to 175° C," in *Canadian Society for Unconventional Gas*, 2011, pp. 1–19.

[14]   A. K. Mehrotra and W. Y. Svrcek, "Viscosity, Density and Gas Solubility Data for Oil Sand Bitumens. Part 1: Athabasca Bitumen Saturated with CO and C2H6," *AOSTRA Journal of Research*, vol. 1, no. 4, pp. 263–268, 1985.

[15]   K. Takamura and E. E. Isaacs, "Interfacial Properties," in *AOSTRA technical handbook on oil sands, bitumens and heavy oils*, 1989, pp. 101–128.

[16]   E. W. Lemmon, M. O. McLinden, and D. G. Friend, "NIST Chemistry WebBook, NIST Standard Reference Database Number 69," P. J. Linstrom and W. G. Mallard, Eds. Gaithersburg MD, 20899: National Institute of Standards and Technology.

[17]   A. Bazyleva, M. Fulem, M. Becerra, B. Zhao, and J. M. Shaw, "Phase Behavior of Athabasca Bitumen," *Journal of Chemical & Engineering Data*, vol. 56, no. 7, pp. 3242–3253, Jul. 2011.

[18]   M. J. Amani, M. R. Gray, and J. M. Shaw, "Phase Behavior of Athabasca Bitumen+Water Mixtures at High Temperature and Pressure," *The Journal of Supercritical Fluids*, vol. 77, pp. 142–152, May 2013.

[19]   M. J. Amani, M. R. Gray, and J. M. Shaw, "Volume of Mixing and Solubility of Water in Athabasca Bitumen at High Temperature and Pressure," *Fluid Phase Equilibria*, vol. 358, pp. 203–211, Nov. 2013.

[20]   Virtual Materials Group Inc., "VMGSim User's Manual version 7." 2012.

[21]   N. Saber and J. M. Shaw, "On the Phase Behaviour of Athabasca Vacuum Residue+n-Decane," *Fluid Phase Equilibria*, vol. 302, no. 1–2, pp. 254–259, Mar. 2011.

[22]   M. A. Satyro, J. M. Shaw, and H. W. Yarranton, "A Practical Method for the Estimation of Oil and Water Mutual Solubilities," *Fluid Phase Equilibria*, vol. 355, pp. 12–25, Oct. 2013.

Chapter 3: A Dynamic Pressure View Cell for Acoustic Stimulation of Fluids—Micro Bubble Generation and Fluid Movement in Porous Media

Robert A. Stewart and J. M. Shaw

Introduction

Interest in vibration and acoustic stimulation applications in porous media and for oil production and aquifer decontamination is long standing but experiments reported to date have focused on limited ranges of frequencies and amplitudes [1, 2]. Vibrations in process facilities, arising from machinery operation, flow induced vibrations and other vibration sources have been studied extensively from the perspective of equipment integrity [3] while vibration impacts on process parameters have received little attention. Development of an apparatus to test and observe impacts of vibration with a range of frequencies and amplitudes on diverse fluids with and without media is required to initiate systematic investigation of these effects.

For example, Nikolaevskii [3] reviewed vibrational well stimulation tests and suggested that the resonant frequency of oil reservoirs is between 100 and 400 Hz. This is therefore the range of frequencies that need to be tested for observation of phenomena occurring in reservoirs. Ultrasonic frequencies have been tested for their ability to improve oil well productivity but are constrained to the near-well-bore zone, on the order of tens of centimeters, due to attenuation [4]. Short distances and high frequencies also remain of interest because pilot plants and laboratory facilities intended to simulate reservoir conditions and processes include equipment that generates high frequency nuisance vibrations and vessels with length scales affected by high frequency vibration. Heat and mass transfer, and flow outcomes realized in such equipment operated in such environments, may not translate to field performance.

Pumps and compressors are common sources of vibration for fluids in process equipment. Many of the frequencies arising in these rotating machines are multiples of the operating frequency. In centrifugal pumps, one such source of vibration is caused each time an impeller vane passes the cutwater, imparting a small pressure fluctuation to the fluid. Similar impacts are seen in centrifugal compressors that generally operate at higher rotational speeds than pumps. The frequencies of these sources of vibration are known to be a multiple of the drive frequency and are dependent on the number of impeller vanes, known as vane pass frequency [3]. Pulsation sources from reciprocating pumps and compressors are more obvious and are related to the end of a stroke or opening and closing of the suction and discharge valves. General industrial guidelines for pumps recommend that discharge pressures should not vary by more than 3% [5]. At atmospheric pressure, such fluctuations are 3 kPa. Much larger pressure amplitudes are possible in high-pressure processes. Lower amplitude vibrations are caused by turbulent flow in process pipework. For example, turbulent flow induces vibration along the wall that has been calculated using large eddy simulation to be on the order of 150 Pa [6]. The amplitude of the acceleration caused in the pipe by pressure fluctuations has been found experimentally to be related to Reynolds number through a power law relationship [6]. Larger vibrations are known to occur in process pipework at small-bore connectors and elbows due to vortex sheading at a frequency related to the flow velocity, density and Strouhal number. These vibrations are a known source of mechanical failure in process facilities with special screening procedures used to avoid causal situations in process pipework such as the "Guidelines for the avoidance of vibration induced fatigue failure in process pipework" [3]. Additional vibrations can be induced by chattering check valves, control valve throttling and flow around orifices in piping systems [7]. Figure 3-1 provides an illustrative example of sources of vibration observed in process pipework [8] that range from ~ 1 Hz to ~ 10 kHz. All of these sources are important because once vibrations are transmitted to the piping and surrounding structural elements they can travel throughout an entire piping system. In laboratory and pilot scale equipment, the frequency distribution and amplitude of vibrations comprise uncontrolled and frequently unmonitored variables in experimental design and outcome evaluation.
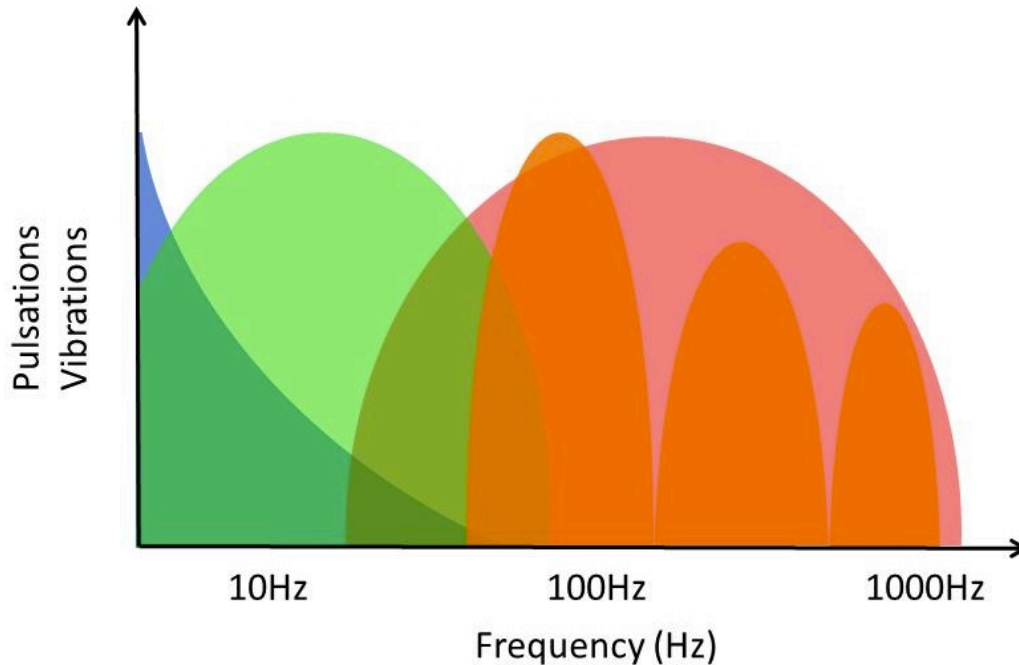
Figure 3-1: Cartoon of excitation sources in piping systems: Flow-induced turbulence related to local Reynolds number (blue), flow-induced vibration related to Strouhal number (green), acoustic induced vibration (red), machinery or rotating equipment generated vibration related to multiples of operating frequency (orange) [8].

Chrysikopoulos and Thomas developed a device to test the impact of acoustic stimulation on Non-Aqueous Phase Liquids (NAPL) in water and a single layer of glass beads [9, 10]. Perchloroethylene (PCE) ganglia were introduced to the glass bead monolayer at various capillary numbers with and without acoustic stimulation. The acoustic stimulation covered a range of frequencies from 75 to 225 Hz with a maximum pressure amplitude of 39 kPa. The concentration of PCE in the produced fluid increased at all levels of acoustic stimulation compared to constant flow without acoustic stimulation. The highest level of PCE content in the effluent was achieved at the lowest stimulation frequency (75 Hz). A camera was set up to record the motion of the PCE ganglia under static and acoustically stimulated conditions. Their images showed that pressure fluctuation overcame the capillary pressure that held the ganglia in pore throats allowing them to move forward into the glass bead bed. The shape of the ganglia changed, and many were broken into smaller

ganglia and displaced from the wall. A modified version of this device was used to investigate the flow of colloids through a packed bed of glass beads [10]. This device was operated over the frequency range 0-150 Hz with a pressure amplitude of 23 kPa. Colloid transport through porous media was determined using luminescence spectroscopy on the effluent.

Roberts et al. [11] measured the colloidal content in the effluent from a sandstone core flow test where a cyclic mechanical stress at 26Hz was applied to the core in a blind cell. Their device produces forces up to 900 N from 0 to 2000 Hz using a magnetostrictive actuator [12]. Stimulation at 26 Hz, produced a size independent increase in colloid content in the effluent over the observed 50 to 800 nm size range compared to zero added stress flow tests. They attributed the increased colloid content to enhanced detachment of particles from pore walls and to particle movement out of dead end pores [11].

Li et al. used a shaker table to observe oil ganglia displacing deionized water in a micromodel [13]. The shaker table was used to produce vibration accelerations of 0.5 m/s^2 to 5.0 m/s^2 at 10, 30 and 60 Hz. Shaking the micromodel produces waves that propagate from all solid surfaces through the fluid simultaneously. This approach is different from imparting vibration to the fluid directly and directionally. They found that increasing the amplitude of these global vibrations enhanced oil ganglia movement through the pore structure. A later publication from the same group used a shaker table to make pore scale observations of oil ganglia liberation between 5 and 14.7 Hz that the authors defined as the "seismic range". The shaker table acceleration was changed from below the level required to liberate the ganglia, related to the capillary pressure, to above. High-speed videography was used to determine ganglia length and point of liberation. Their work underscores the importance of visualization in apparatus design and operation, a feature that has been incorporated into many variable or fixed volume view cell designs for observing critical properties of fluids, phase behaviour and mixing [14-17]. Non-intrusive telemetry is normally used for visualization. Consequently, observation is pressure independent. However, the pistons or bellows used to control volume in these latter cases are not normally designed to be actuated dynamically.

Micromodels are generally solid 2D extrusions made from plastic, etched glass or silicon with a transparent cover. The additive or subtractive substrate method of manufacturing prevent 3D shapes from being generated and therefore hypotheses related to three-dimensional effects or unconsolidated media have not been demonstrated. 2D micromodels have been used by many researchers to visualize flow and ganglia entrapment in porous media (ex. [2, 13, 18-20]). Micromodels are a powerful experimental technique as they allow the designer to control the shapes of the pores, the solid surface properties, and fluid injection locations to test specific sets of experimental parameters. Fluorescent dyes have been used to highlight specific fluids within micromodels allowing for displacement mechanisms and saturation levels to be determined [18]. Some micromodels have been used with liquid and gas phases to explore different petroleum production techniques [2, 19, 20]. Ultrasonic (22.5kHz and 40kHz) displacement of immiscible phases has been tested within micromodels comprising both homogeneous and heterogeneous pillars immersed in an ultrasonic bath [2, 19]. Similar to the shaker table mentioned above this method causes pressure wave propagation to arise from all locations in the media at once. At a certain level of complexity it becomes simpler to use the natural porous media and different imaging techniques such as x-ray computer assisted tomography, magnetic resonance imaging, ultrasonic imaging or optical techniques.

High-pressure cells have been created for acoustic property measurement of fluids using piezoelectric actuators. Sturtevant et al. [21] created a device capable of measuring the speed of sound in fluids at temperatures up to 250°C and pressures up to 20.7 MPa. Their piezoelectric device operated in the MHz frequency range as do many non-intrusive inspection techniques utilizing ultrasound [16]. The use of piezoelectric actuators is clearly advantageous given the control over waveform and frequency but the frequencies used are not relevant to the present study due to very high attenuation and absences of sources generating this frequency range in industrial processes.

Rigord et al. [22] investigated varying the inlet pressure on a simulated core to determine how the transmittance and admittance of pressure changed with porous media

heterogeneity. Their device, designed to apply pressure waves to the core and not the fluid, generated large pressure amplitude sinusoidal waves but due to the "syringe like" design and the intended investigation only operated at very low frequency (0.07 Hz). Muhamad et al. [23] also used very low frequencies to investigate the impact that pressure variation has on the dilution and gravity production of heavy oil using butane under simulated reservoir conditions. The pressure reduction to atmospheric within the packed glass bead bed was held for 3 and 8 minute intervals. Pressure was controlled using a control valve at the solvent injection port of the cell that relieved pressure and then added butane at the pressure of the tank. They observed that final recovery and recovery rates were improved by the reduction in solvent pressure and suggested that this was due to a change in direction of the solvent diffusion driving force that formed channels in the media. Their apparatus did not permit observation of the simulated reservoir. The overall recovery was higher with shorter time interval pressure fluctuations.

Gas or vapour bubbles can be generated using pressure fluctuation and they are known to play an important role in acoustic propagation and attenuation [24]. Bubbles in sound fields have also been used for mixing in microfluidic devices [25] and in more conventional, soundless settings [26]. Many texts related to sonar and submarine warfare cover the topic of sound interacting with bubbles in water. More recently equations developed in that application area have been used to determine the gas content and size of bubbles in porous media [27]. Kim et al. [28] clearly describe how gas bubbles cause attenuation and change the compressibility of a medium. They show how to use this knowledge to calculate gas void fraction, and present a non-linear acoustic method to determine gas void fraction of a porous medium based on a piezoelectric transducer that simultaneously generates pressure signals with amplitudes of 58 and 53 kPa at 28 and 33 kHz respectively.

From the foregoing, apparatus for evaluating the influence of vibration on specific fluids and combinations of specific fluids and porous media have been developed for frequencies ranging from near zero up to 225 Hz and using ultrasonic piezoelectric transducers at frequencies above ~ 20 kHz. This work, drawing on the understanding and limitations of the prior art, targets the development of a general-purpose device for the gap in between,

which includes the industrially relevant range of frequencies found in pipework with an emphasis on the frequency range 500 Hz to 5000 Hz. A dynamic pressure cell able to accommodate a broad range of frequencies, waveforms and amplitudes, has been developed. The qualitative features of the device including waveform generation, the measurement of transmitted waveforms, imaging, bubble generation and micro-bubble detection, and visualization are exemplified, and illustrative applications including observation of flow in porous media are presented. Subsequent contributions will address quantitative measures related to the impacts of vibration and micro bubble formation on mutual diffusion and solid–liquid mass transfer in porous media, to cite but two applications.

Experimental Apparatus, Methods and Analysis

Apparatus

The acoustic apparatus comprises four main systems, each comprising multiple components: the electrical drive system, the view cell, the flow control system and the measurement system as sketched in Figure 3-2. The piezoelectric stack actuator (Physiks Instruments P840.40) is the key component of the electrical drive system. It also includes a signal generator (Agilent 33500B waveform generator) and an amplifier (Physiks Instruments E501.00, 100W, 30 to 130 V) used to control the actuator. The signal generator is connected to a PC using a USB to load arbitrary functions, and to the data acquisition system to provide a reference signal for the collected data. The view cell, shown in Figure 3-3, consists of a precision glass tube (Wilmad Lab Glass, 25.4 mm OD x 17.46 mm ID of 200 mm and 690.5 mm in length and bevelled ends), a bellows assembly (Servometer, custom design), piezoelectric stack actuator attachment accessories (Physiks Instruments P176.50 flexible tip and custom thread adaptors) a tube plug and fluid adjustment lines. The tube holder, piezoelectric actuator housing and the view cell stand are shown in Figure 3-4. Fluid addition and flow are controlled using the fluid adjustment lines within the tubes. For flow experiments a syringe pump (Teledyne ISCO 500D) is

attached to the fluid adjustment lines. It can be operated at controlled flow rates or controlled pressures. The syringe pump has two manual valves attached to it to control fluid flow and refill. The pressure output of the pump is fed to the digital acquisition system (DAQ) and recorded. The measurement system consists of a DAQ (National Instruments USB 6351), a dynamic pressure transducer (OMEGA DPX-101), a power supply for the pressure transducer (OMEGA ACC-PS1), a custom voltage divider to convert the signal from the pressure sensor into one compatible with the DAQ, a PC and a custom VI in LabView (National Instruments, 2012 SP1) to capture the pressure sensor, a signal generator, and syringe pump outputs. Custom VI Labview code is used to save sensor outputs at 100,000 samples per second in a binary data file and to provide real time visualization of signals.

Care must be taken during the assembly and initial filling of the tubes to prevent the introduction of air bubbles and the formation of bubbles from dissolved gases in fluids. Organic solvents were degassed using an ultrasonic cleaner (Elmasonic S 10/(H), 37kHz) and water was boiled to removed dissolved gasses prior to experiments except where stated otherwise. To avoid air bubble entrainment during bellows insertion into the glass tube, the bellows should be placed in the fluid and the tube inserted over the bellows. To prevent bubble entrainment at the other end of the tube, the plug should be inserted into a liquid filled tube with the injection lines open to atmosphere. In this way, the fluid pushes air into the injection lines and out of the tube as the plug is inserted, eliminating this source of air bubbles. To obtain bubble free porous media a mixture of unpacked beads and fluid should be poured into the tube with a plug and a filter in place to constrain the bead bed location. A second plug and filter are then inserted above the bubble free loosely packed bed and pushed into place to pack the bed. The view cell is designed to allow the user to observe what occurs during assembly and during experiments. Small bubbles, drops and particles are readily detected as illustrated in Figure 3-5. A 180 μm diameter glass bead, Fig. 3-5a, is easily observed in the tubes, Fig. 3-5b, without magnification.

Fluids and Particles - Illustrative Measurements

Acoustic tests were performed with four fluids: water (De-Ionized Ultra-Filtered water), n-pentane (Sigma Aldrich, lot 135690), castor oil (Exact, packaged for Loblaws Inc. by Par RW packaging Ltd., lot 30287-01, 2008), and toluene (Fisher Scientific, HPLC grade) using two lengths of tubes. Flow tests were performed at three flow rates, 5, 10 and either 100 or 200 ml/min depending on whether the maximum pressure for the DPVC (1 MPa) was exceeded at 200 ml/min, with/without a packed bed comprising 250-330 μm diameter spherical silica beads supplied by Sovitec (C1 SP 250-330 T0).
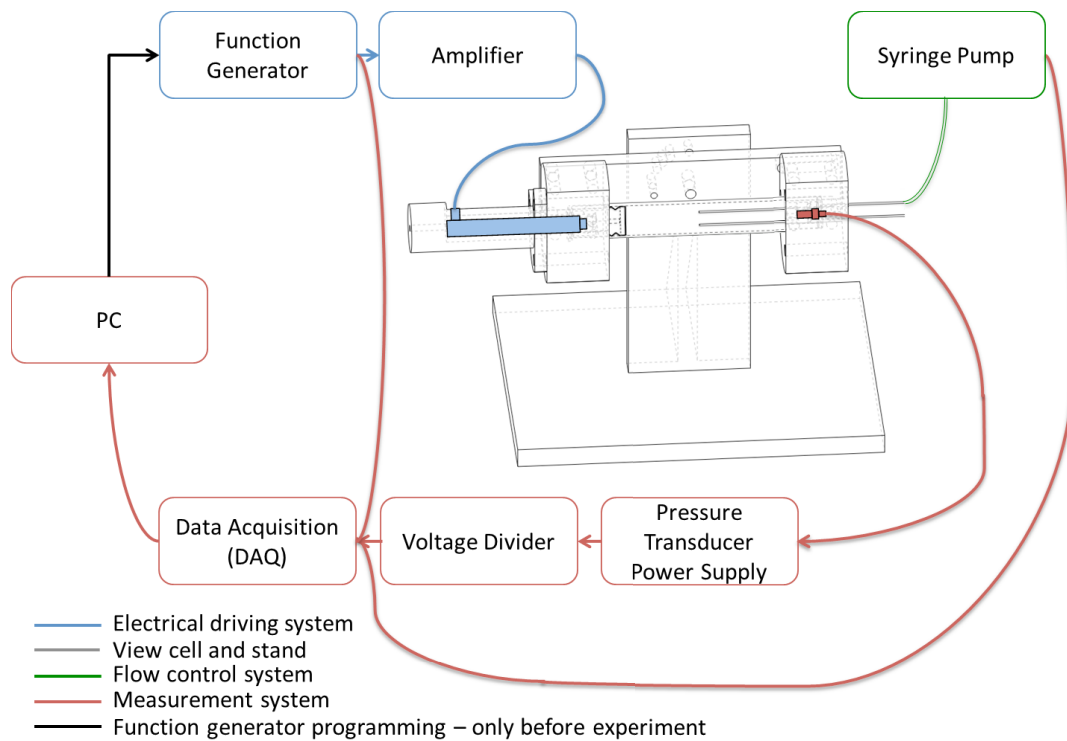
Figure 3-2: Acoustic apparatus showing 4 main systems
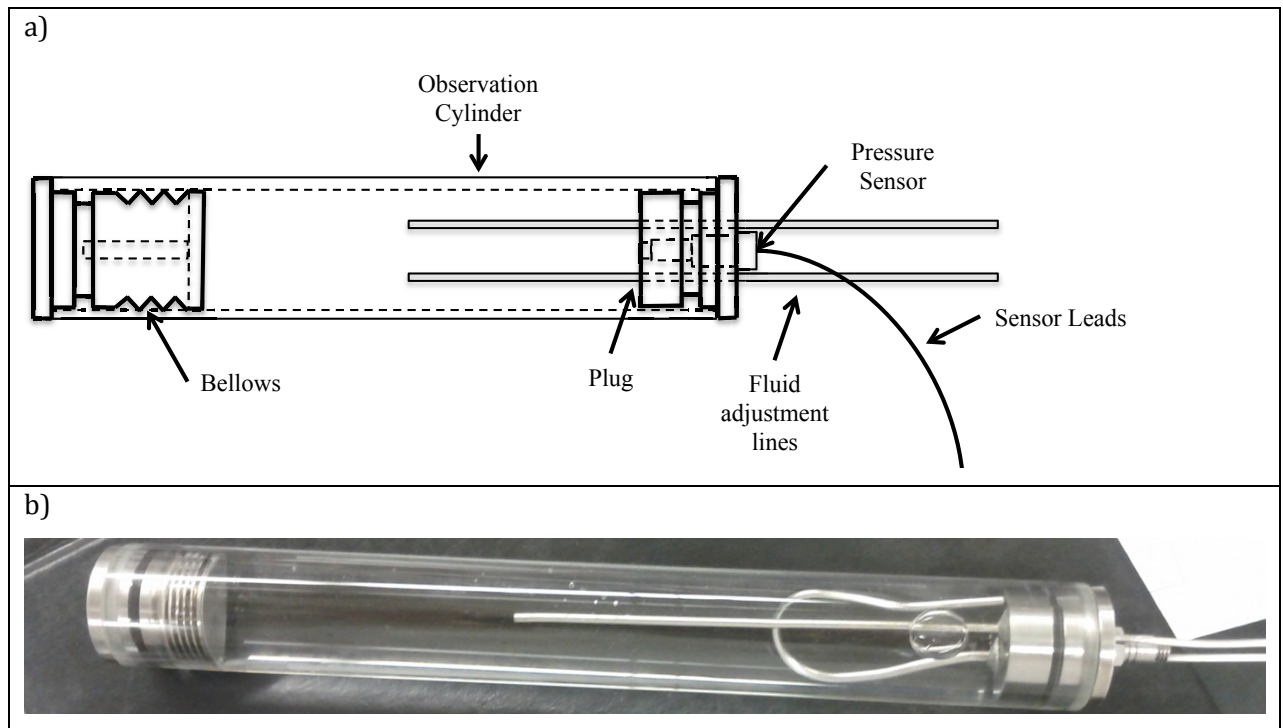
Figure 3-3: View Cell: a) schematic with labeled components: bellows, plug, fluid adjustment lines, pressure sensor and glass cylinder, b) image of the assembled 200 mm device filled in the same orientation as a) with tap water showing a large air bubble at the right hand side.
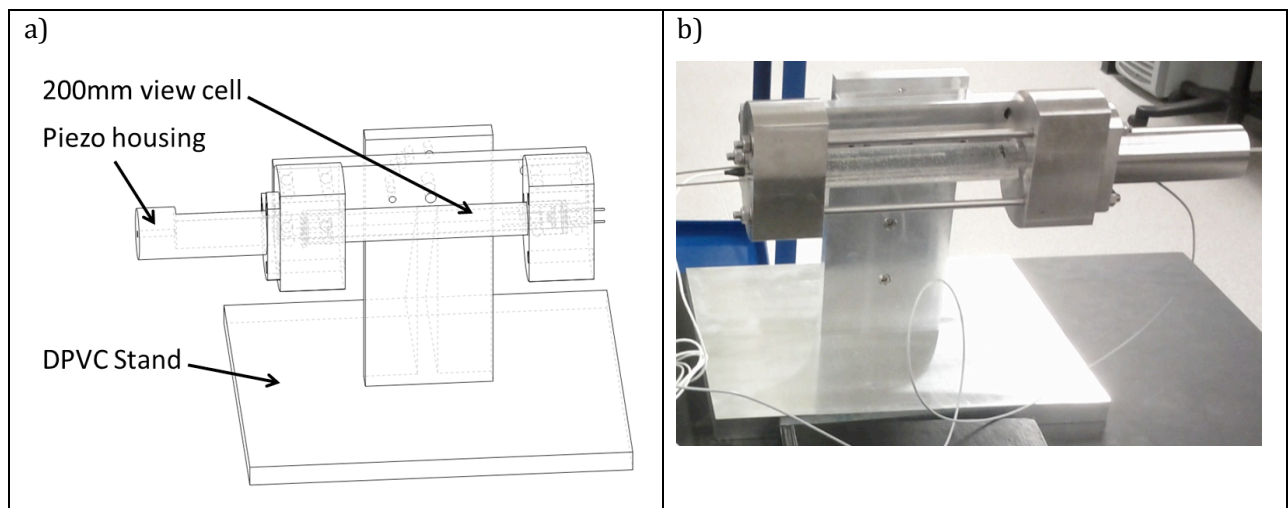
Figure 3-4: a) A schematic showing the Differential Pressure View Cell (DPVC) stand set up for the 200 mm cell, b) an image of the assembled DPVC with the 200 mm glass tube, the piezoelectric actuator and the pressure sensor installed.
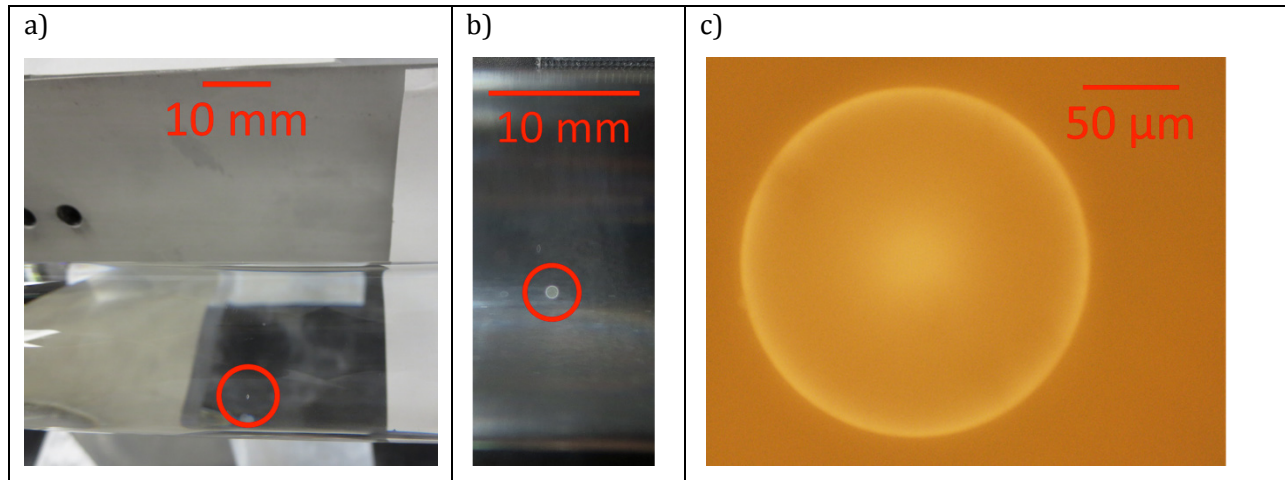
Figure 3-5: Images of a 180 μm diameter glass bead in the DPVC in water: a) viewed from a distance of 25 cm, b) viewed close up, c) viewed under a microscope.

Waveform, Waveform Analysis and Averaging Calculations

The same waveform was used in all experiments. The waveform was created using BenchLink, an Agilent wave generation software package, and uploaded to the signal generator at 20 kSa/s. The waveform was composed of sine waves at 10 to 5000 Hz and amplitudes of 0.5, 1 and 2 Vpp are output from the signal generator. This signal was then amplified 10 times to 5, 10 and 20 Vpp. The 10 to 100 Hz interval comprises 1 second segments with a 10 Hz step and the 200 to 5000 Hz interval comprises 0.5 second segments with a 100 Hz step. All acoustic transmission tests were analyzed using the same method. The start of a full waveform was identified in each test using a custom code in LabView. This was then used as the starting point for the data manipulation and interpretation. The input waveform is captured along with the dynamic pressure at the opposing end of the tube as seen in Figure 3-6a. The output waveforms are segmented by input frequency and then averaged over a single input period, Figure 3-6b. The lowest average point is subtracted from the highest average point to determine the average output peak-to-peak amplitude. The largest positive and negative deviations from the average are captured as the variability of the measurements. The peak-to-peak amplitude is plotted with the maximum positive and negative deviation values versus input frequency. The

resulting plot, Figure 3-6c, looks like a spectral plot but is actually a plot of the output pressure amplitude as a function of input frequency.

a)

bi)
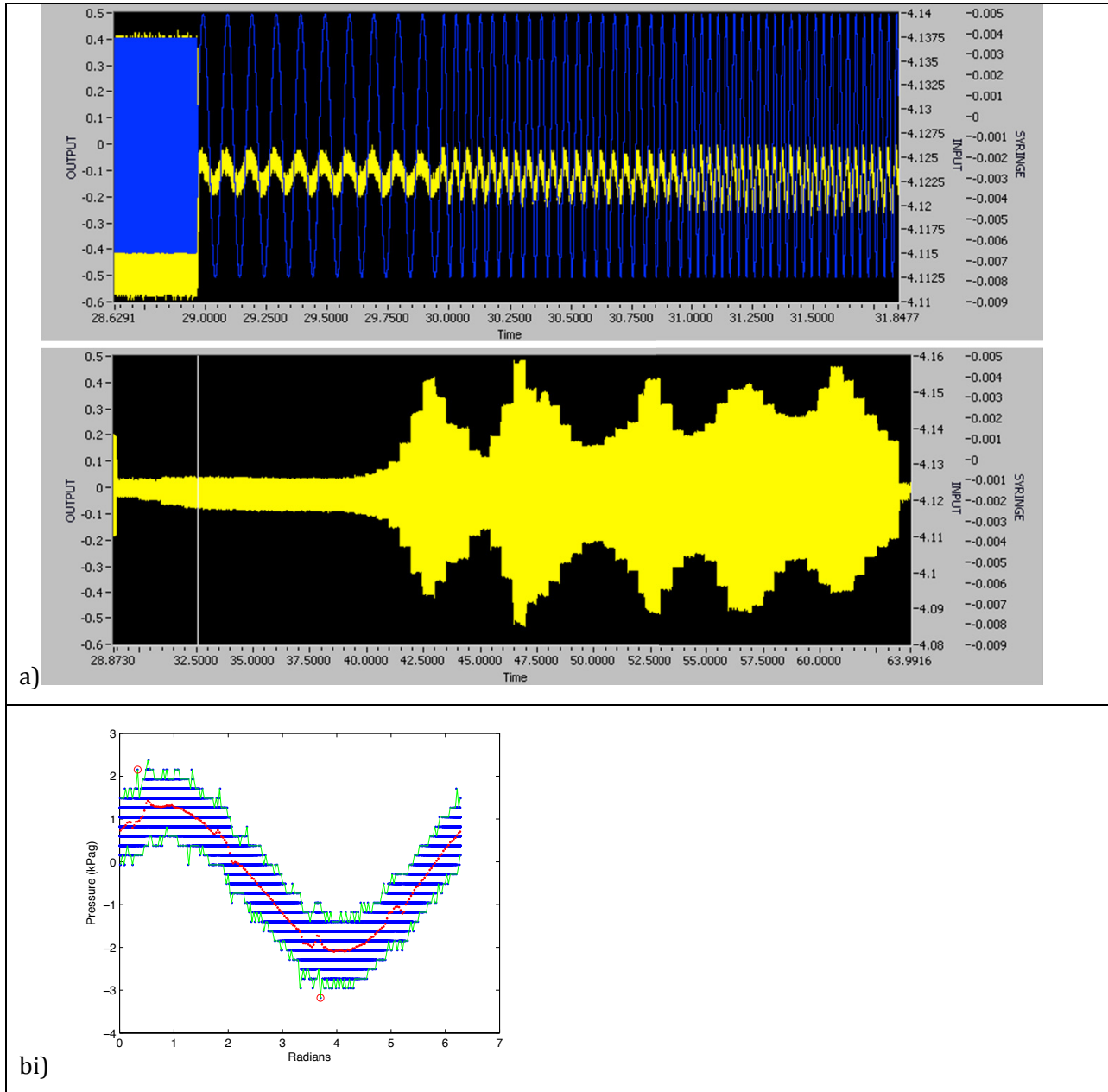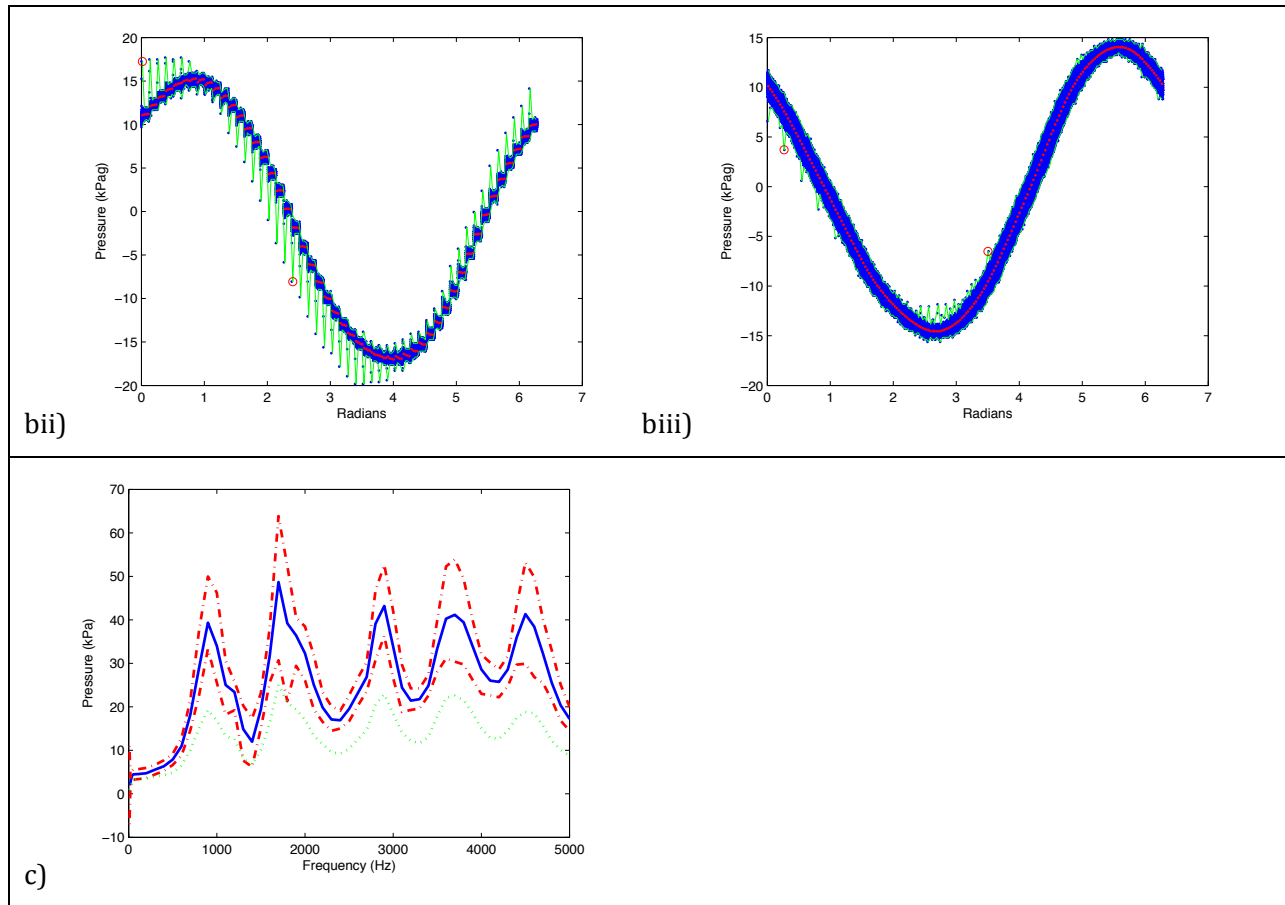
Figure 3-6: Waveform averaging example: a) raw waveforms: input (blue), output (yellow), b) data at 30 Hz (i), 2000 Hz (ii) and 4300 Hz (iii) plotted over one period of the input frequency period (blue), average of all values at a specific point in the period (red), maximum and minimum points at a given point in the period (green), c) frequency specific output with average pressure amplitude (blue) taken from the amplitude average period plots, maximum and minimum amplitudes (red dotted line) taken as the maximum deviation from the average period plot.

Results and Discussion

Baseline Calibrations in Air and an Air Filled Tube

The acoustic apparatus was operated without installing a tube in air, Figure 3-7a, and with an air filled tube, Figure 3-7b, to ensure that the transmitted waveform did not have

60

frequency dependent noise apart from noise arising in the liquid column. The absence of a signal at all input frequencies indicates that the sensor is isolated from the actuator. The output signals are all less than 1 kPa, and this can be considered the upper limit for signal noise using a 5 Vpp, 10 Vpp or 20 Vpp input signal.
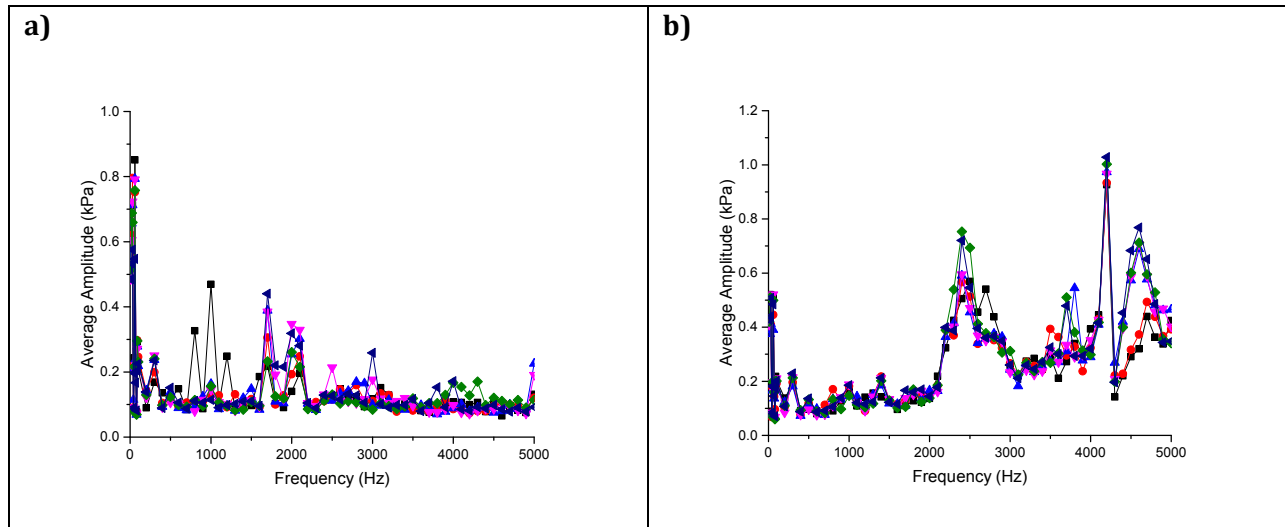
Figure 3-7: Output frequency response to a 5 Vpp input signal for: a) no tube, b) an air filled (200 mm) tube. The order of the sequential scans is

━■━ , ━●━ , ━▲━ , ━▼━ , ━◆━ , ━◀━ .

Transmitted Signal Attenuation in Stagnant Liquid Columns

Three liquids (water, pentane and castor oil) were placed in tubes with lengths 200 mm and 690.5 mm and exposed to the frequency scan described above to determine how attenuation impacts system response. These liquids were selected for baseline tests because water is a useful reference, pentane has a high vapour pressure and is therefore likely to cavitate, and castor oil is a non-toxic high-viscosity Newtonian fluid. Key properties for these fluids are given in Table 3-1. Once the bellows and plug are inserted into the fluid column their lengths are 163.15 mm and 653.6 mm. The longer fluid column is thus 4 times the length of the shorter fluid column. Each liquid sample was subject to a

minimum of six successive frequency scans to determine response repeatability – from the fluids and from the system itself. The frequency responses for these cases are presented in Figure 3-8a-f. As expected, resonant peaks were detected in all cases. While frequencies at which a fluid filled tube resonates can be calculated, contributions from the resonant operating frequency of the piezoelectric actuator, the frequency dependent compressibility of the bellows, and whether there are bubbles present that alter the compressibility of the liquid column and can shift the resonant response of the apparatus and apparatus response must be measured. For example, the resonant frequencies of the bellows and the piezoelectric actuator are 2800 Hz and 8 kHz respectively, in the unloaded state, according to the manufacturers. The resonant frequencies of these components are expected to vary with the applied frequency and the compressibility of the fluid as these affect the loading. Thus, the resonant frequency of these components and of the apparatus as a whole can depend on the applied frequency.

Key observations from this apparatus survey include: that the resonant frequencies are fluid column length dependent, a dominant and expected behaviour seen for all three fluids; that the amplitudes and form of the resonant peaks for water, Figure 3-8c vs. Figure 3-8d, and for castor oil, Figure 3-8e vs. Figure 3-8f, are repeatable and independent of tube length, suggesting that attenuation is not significant in the fluid columns in the absence of bubbles or obstacles to sound wave transmission; that with these tube lengths high peak-to-peak pressure amplitudes are limited to the 1 to 5 kHz range; and that there is significant diminution in peak-to-peak pressure amplitude below 500 Hz. Clearly, large and uniform peak-to-peak pressure amplitudes cannot be achieved at all frequencies without varying the tube length, and the input signal. The apparent anomalous behaviour of pentane shown in Figures 3-8a and 3-8b is attributed to bubble formation, a topic explored in detail in the section entitled "Bubbles and Resonance in Liquid in a Stagnant Column—Selected Background". In Figure 3-8a, the first scan is comparable to the scan for castor oil, Figure 3-8e. Each subsequent scan exhibits greater attenuation and the resonant peaks disappear by the sixth scan in response to increasing bubble formation with time. For the experiments reported in Figure 3-8b, the tube was filled with subcooled pentane and allowed to equilibrate. By increasing the baseline operating pressure of the system,

cavitation arising from induced vibration was supressed. Relieving the pressure back to atmospheric allowed bubbles to form in response to induced pressure fluctuations, leading to signal attenuation with time and elimination of resonant effects. While bubble detection in a fluid column can be made by direct visual observation for macroscopic bubbles, both micro and macro bubbles can be detected from changes in the transmitted amplitude signal relative to the liquid in the column—particularly at resonant frequencies.

Table 3-1: Fluid Properties at 20°C

	Density kg/m^3	Speed of sound m/s	Viscosity μPa*s	Vapor Pressure kPa
Water	998.21[1]	1482.34	1001.6[1]	2.337[6]
Pentane	625.75[1]	1035.5[1]	227.46[1]	56.549[6]
Castor Oil	959[3]	1498[2]	985000[4]	~0[7]
Toluene	866.89[1]	1324.34	562[5]	2.926[6]

Notes for Table 3-1:

1. See reference [29].

 2. See reference [30].

3. Measured using an Anton-Paar DMA5000 (this work).

 4. Measured using Malvern Gemini HR Nano Rheometer with a double gap (this work).

5. See reference [31].

6. Calculated using Antoine equation with coefficients from [29].

7. Assumed for purpose of this work.
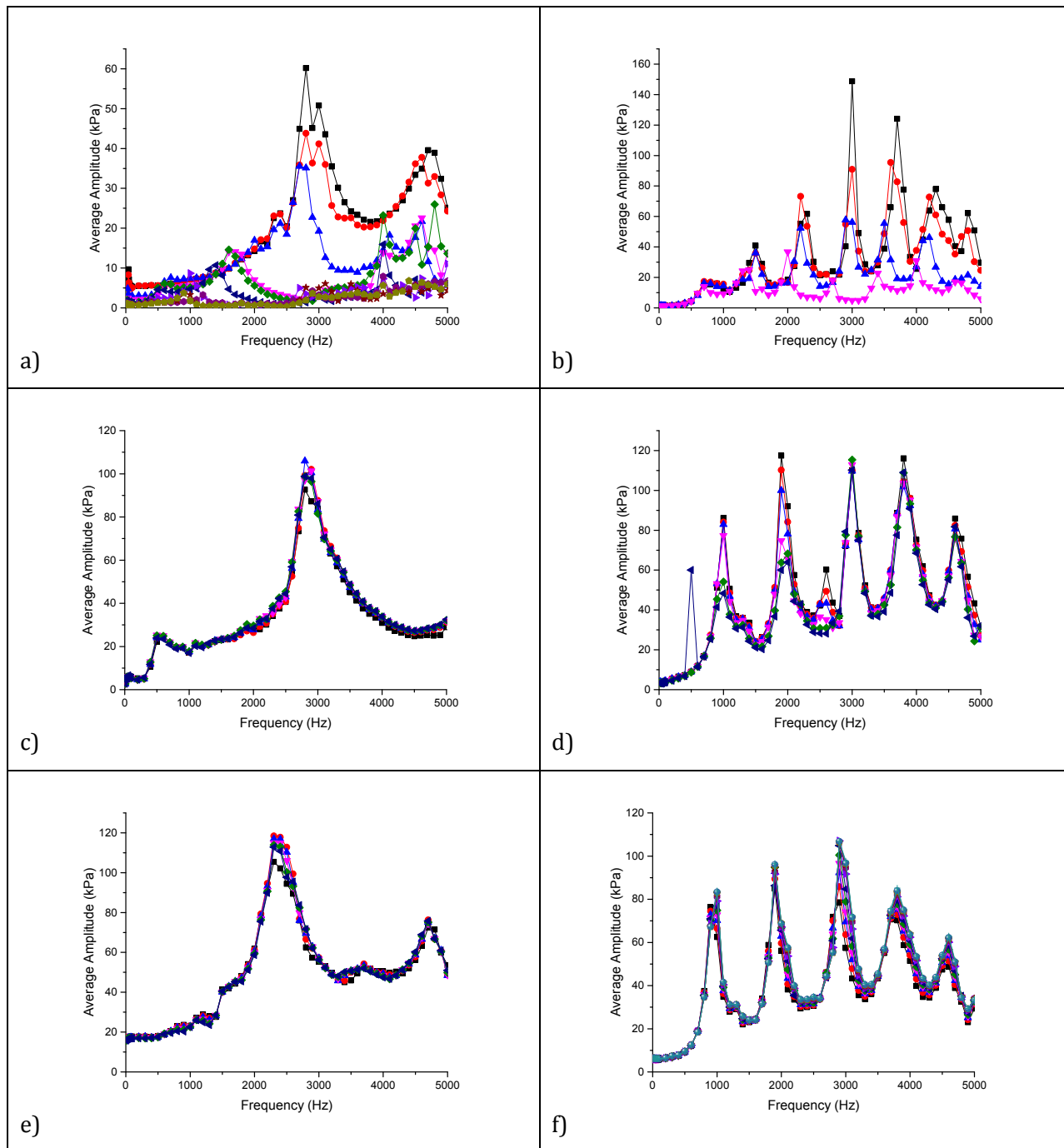
Figure 3-8: Frequency response actuated by 5 Vpp of a) pentane in a 200 mm tube, b) pentane in a 690.5 mm tube, c) DIUF water in a 200 mm tube, d) DIUF water in a 690.5 mm tube, e) castor oil in a 200 mm tube and f) castor oil in a 690.5 mm tube. Each data set colour is an individual scan through the frequencies. The order of the measurements in time was ━■━ , ━●━ , ━▲━ , ━▼━ , ━◆━ , ━◀━ , ━▶━ , ━⬣━ , ━★━ , ━⬟━ , ━●━ , ━┼━ .

Bubbles and Resonance in Liquid in a Stagnant Column—Selected Background

The resonant frequency for a close-ended tube, f_{tube}, containing a uniform fluid can be calculated from the speed of sound in the fluid, c, and length of the tube, L :

$$f_{tube} = \frac{c}{4L} n$$

<div align="right">**Equation 3-1**</div>

where n is a positive integer defining the number of quarter wavelengths observed in the standing wave in the tube.

If the speed of sound in a uniform bubbly fluid is known or can be calculated, the corresponding resonance frequency of the tube can also be determined using Equation 3-1. There are many equations for determining the speed of sound in bubbly fluids from simple to quite complex depending on assumptions including the adiabatic nature of the sound wave, and the impacts of viscosity and interfacial tension. In this work Wood's equation is used [32]:

$$\frac{c_0}{c} = \left(1 - v + v\frac{\beta_0}{P_0}\right)\left(1 - v + v\frac{\rho_g}{\rho}\right)$$

<div align="right">**Equation 3-2**</div>

where the subscript *0* denotes the properties of the continuous fluid phase, v is the volume fraction of bubbles, subscript g denotes the properties of the gas, β is the bulk modulus of the fluid, ρ is the combined fluid (liquid and gas) density and P is the pressure.

The derivation of Equation 3-2 assumes isothermal bubble compression. The composition, number and size of bubbles need not be known. Equation 3-2 provides reasonable predictions of the speed of sound remote from the resonant frequency of bubbles in a fluid [33]. The resonant frequency of bubbles in a fluid can be calculated from first principles [24]. When the input frequency is above the resonant frequency the bubbly fluid tends to

compress out of phase with the applied frequency. Bubbles smaller than the resonant size oscillate in phase with the applied frequency. This means that as the applied frequency approaches the resonant frequency the detected frequency shifts [24] and attenuation is also a maximum near the resonant frequency of the bubbles. From first principles a simple resonant frequency equation for spherical bubbles smaller than the wavelength of the sound wave [24] is obtained:

$$f_{bubble} = \frac{1}{2\pi r}\sqrt{\frac{3\gamma P_0}{\rho_0}}$$

Equation 3-3

where r is bubble radius, and γ is the adiabatic exponent.

The upper bubble size limit in the apparatus is approximately the radius of the glass tube (8.73 mm). From Equation 3-3, resonant air and vapour bubbles in the frequency range 1 Hz to 5 kHz fall in a narrow band, as shown in Figure 3-9, and are observable. Even at 5 kHz, resonant bubbles are $\sim$ 500 µm in radius or more than 5 times the radius of the smallest bubble visible unaided ($\sim$ 90 µm). This means that Equation 3-2 can be used to estimate the speed of sound in bubbly flows in this apparatus, as long as there are no visible bubbles resonating at a specific frequency.
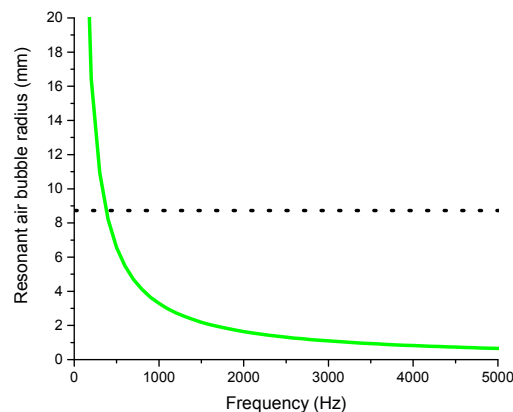
Figure 3-9: Resonant air bubble radius in water versus frequency. The upper size limit, the DPVC tube radius (8.73 mm) is shown as a dashed line.

While resonance contributions from the mechanical components (the piezoelectric actuator and bellows) also contribute to the complexity of the response of the system and may vary with operating conditions, observation of the changes in the waveform over consecutive samplings allows for the observation of bubble generation and may allow for estimation of bubble concentration or size. For example, the increase in the compressibility of the fluid due to bubbles shifts the resonant peaks in the tube and depresses all peaks due to increased attenuation. If a frequency specific decrease in amplitude is observed, the bubble causing this should either be observable or the number of unobservable bubbles must approach the volume of a resonant bubble at that frequency. Even if the bubbles are not resonating, the interplay between bubble and apparatus resonance is important because within a standing wave, bubbles smaller than the wavelength of the sound wave travel up the pressure gradient to the antinode. Bubbles larger than the wavelength travel down the pressure gradient to the node [34]. This can lead to vigorous bubble movement as reported by Liu et al. [25] that can affect local heat and mass transfer and mixing as is apparent in Figure 3-10 (Multimedia view).
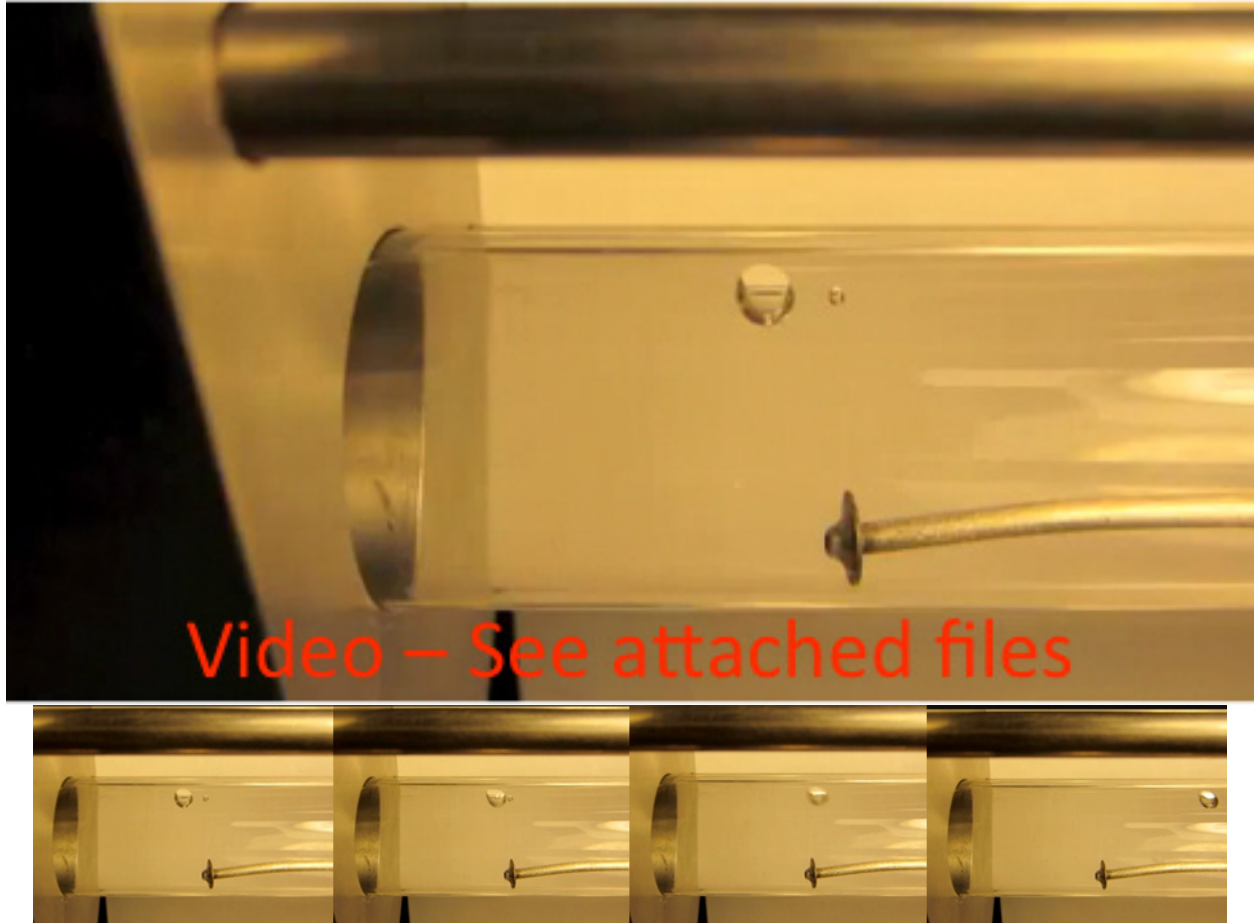
Figure 3-10: Video and still frames of a bubble in boiled DIUF water. For reference the washer on the end of the fluid adjustment line is 4.79 mm in diameter. (Multimedia view)[URL: http://dx.doi.org/10.1063/1.4929460.1]

Bubbles and Resonance in Liquid in a Stagnant Column—Results

Inserting air bubbles into the tube with water, Figure 3-11, and in more volatile fluids like toluene, Figure 3-12, allows for confirmation of the impact bubbles have on apparatus response. Figure 3-11a shows the frequency response from the 200 mm tube containing boiled DIUF water and following injection of a single air bubble (~3.3 mm in diameter). As expected, the overall amplitude drops when a bubble is present. Images and video of this air bubble are shown in Figure 3-10 (Multimedia view). The video shows how different frequencies cause different surface vibrations on the bubble. At certain frequencies, associated with the resonant frequency of the bubble, the bubble vibrates vigorously. Similar observations have been made by others who recommend the use of a bubble as a

mixer in microfluidic devices [25]. This observation shows that bubble resonance is effective for larger scale mixing as well. The responses shown in Figure 3-11b for tap water start with a large number of air bubbles attached to the tube wall. Once the tube is subjected to vibration, the bubbles detach from the tube surface and begin to coalesce into larger bubbles. A threshold of bubble size/number is required to affect the resonance behavior of fluids in tubes. Using a syringe to insert air bubbles into the fluid constrains the maximum size of bubble observed but with breakage/coalescence, the volume of individual bubbles and the volume distribution corresponding to each scan is not known.
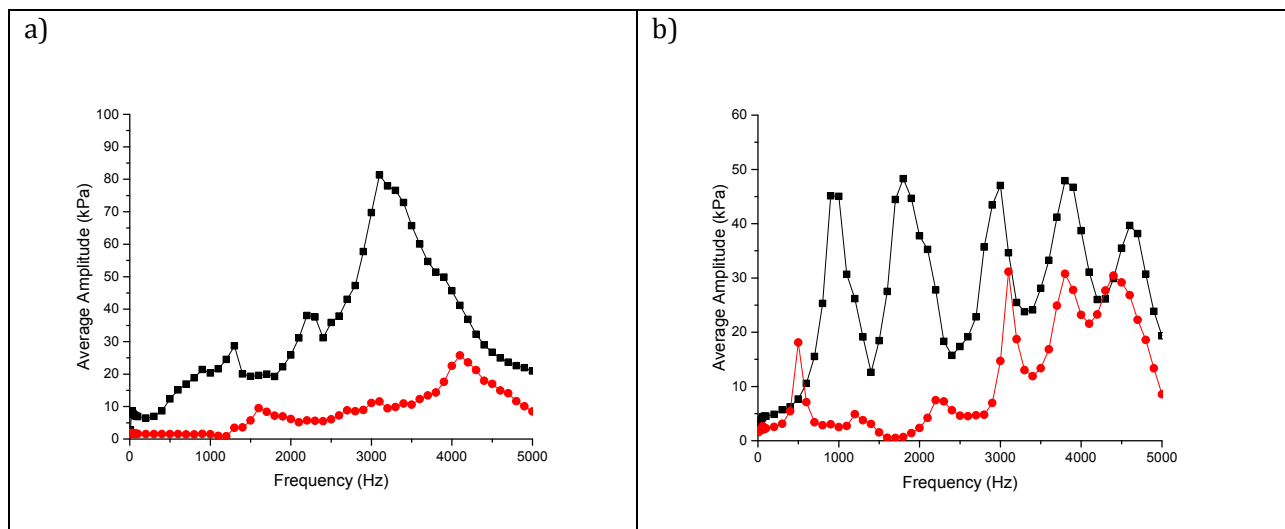
Figure 3-11: Average frequency response of a) boiled DIUF water in a 200 mm long tube actuated by 5 Vpp signal with no air bubble (▬■▬) and after the injection of a single ~3.3 mm diameter air bubble (▬●▬); b) tap water in a 690.5 mm long tube actuated by 5 Vpp signal with small bubbles from the tap water (▬■▬) and after the coalescence of the bubbles into one larger bubble (▬●▬).

In volatile fluids, pressure fluctuations can drop below the vapor pressure of the fluid and cause cavitation. The frequency response for a toluene filled tube and for toluene plus a small air bubble are shown in Figures 3-12a, and 3-12b respectively. As with the water and air bubbles experiments, the addition of the air bubble reduces the amplitude of the signal and shifts the resonant peaks to lower frequencies. Air bubble vibration also induces other bubbles, likely toluene vapor, to form. This increase in the number of small bubbles in the

tube further reduces the speed of sound in the fluid and shifts the frequency of the resonant peaks and reduces their amplitude. Bubble generation is illustrated in Figure 3-13 (Multimedia view). At the frequencies where the air bubble vibrates the most vigorously, small bubbles appear and move toward it. Slow motion video at these frequencies also allows the observation of how bubbles change shape. The frequency ranges where the air bubble oscillates most vigorously are 2900-3300 Hz and 3900-4500 Hz. These ranges align closely with the resonant peaks in the toluene + air bubble response and appear to be responsible for the dramatic reduction of amplitude at these frequencies. Thus the increased fluid compressibility and bubble resonance jointly contribute to the change in the frequency response of the apparatus.
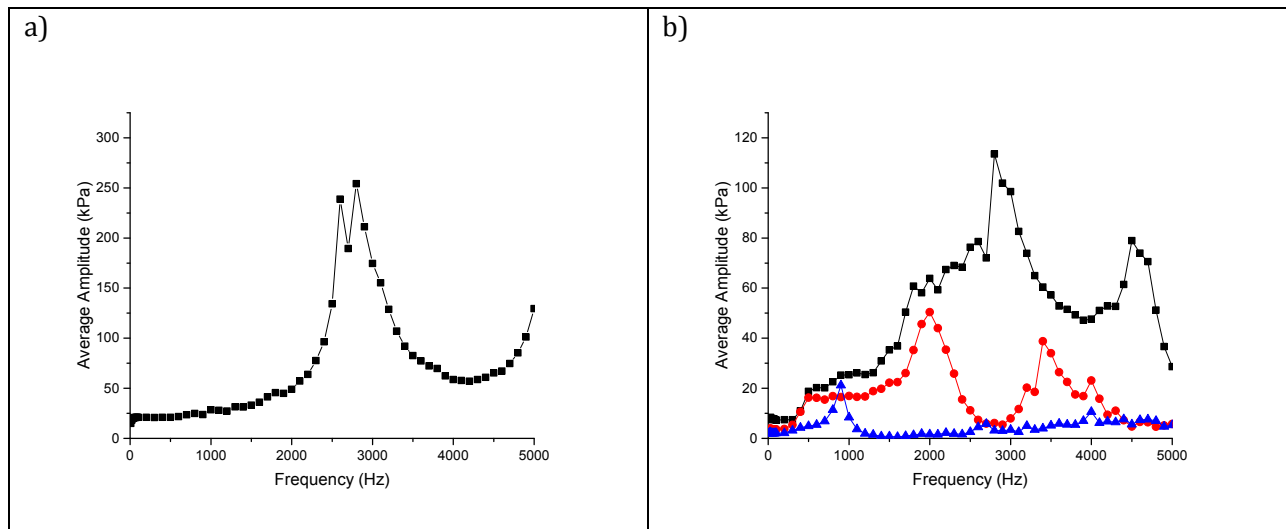
Figure 3-12: Frequency response in toluene actuated by 5 Vpp in a 200 mm tube with a) no visible bubbles averaged over 6 repeated frequency scans and b) air bubble motion causing bubble generation where ▬■▬ is the first response generated with the air bubble, ▬●▬ is an intermediate frequency response after some bubble generation and ▬▲▬ is the final response with many bubbles large enough to observe but few larger than 180 μm in diameter in the system.
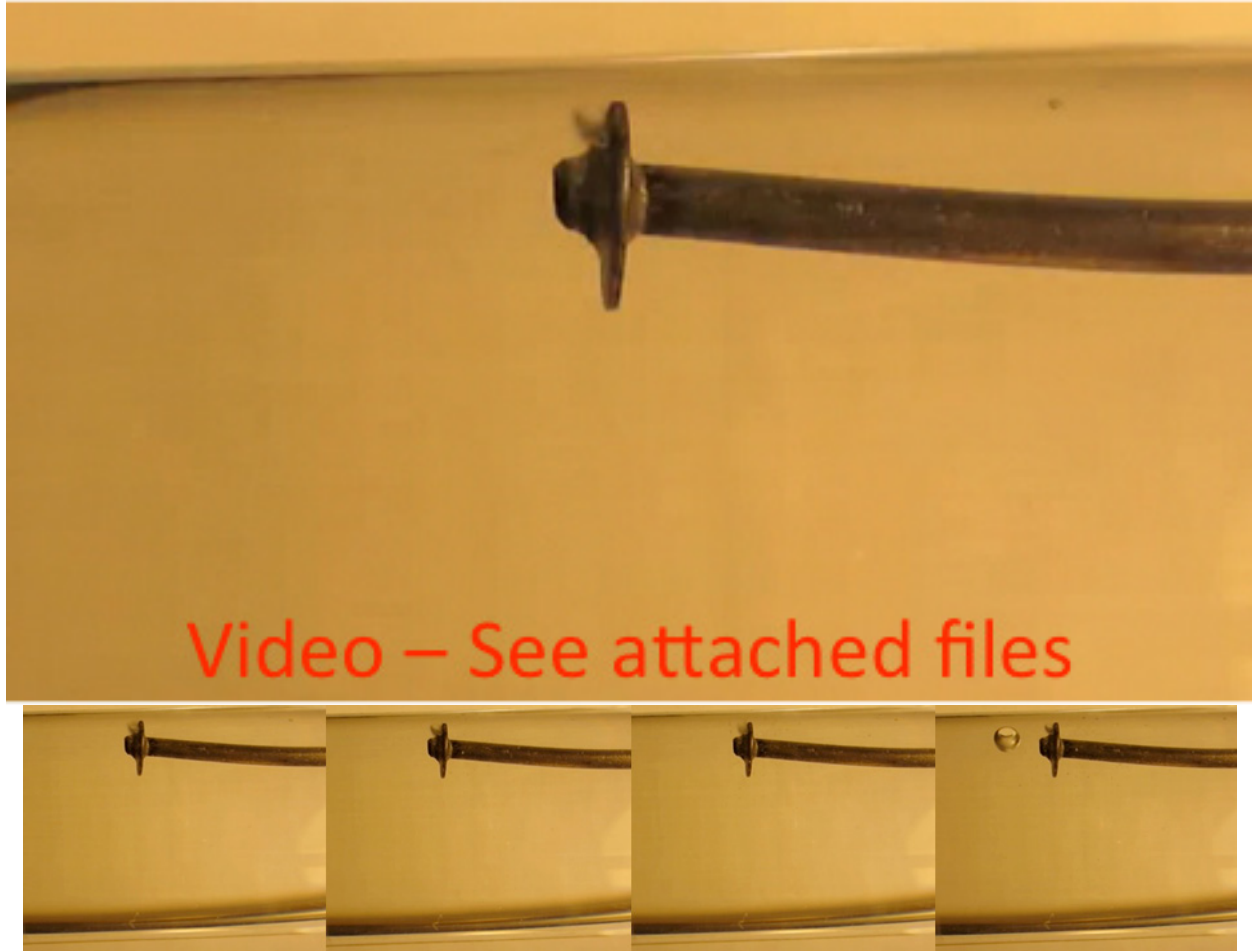
Figure 3-13: Video and still images of toluene with an air bubble and with bubble generation. For reference, the washer on the end of the fluid adjustment line is 4.79 mm in diameter. (Multimedia view) [URL: http://dx.doi.org/10.1063/1.4929460.2]

Input Voltage and Transmitted Pressure Amplitude—Stagnant Liquid Column

Figure 3-14 shows the response of the 200 mm tube filled with castor oil to 5, 10 and 20 Vpp inputs signals. Pressure amplitude increases with increasing voltage with the largest change at the system resonant frequency. For castor oil, the transmitted signal can be tuned by varying the input signal. 80 kPa peak-to-peak waves are accessible from 10 Hz – 5 kHz, and the dynamic range is larger, up to 500 kPa, near resonant frequencies. Achievable outcomes are comparable for other fluids. The applied voltage is limited to 20 Vpp because the glass tubes break at higher amplitudes. With thicker glass or sapphire tubes, the next

limitation in the system is the signal generator and amplifier combination, which has a maximum output amplitude of 7 Vpp with a 1.5 V offset. This imposes a maximum amplitude of 70 Vpp. With a 70 Vpp amplitude applied to the tube, substantially larger pressure amplitudes can be obtained with stronger tubes.
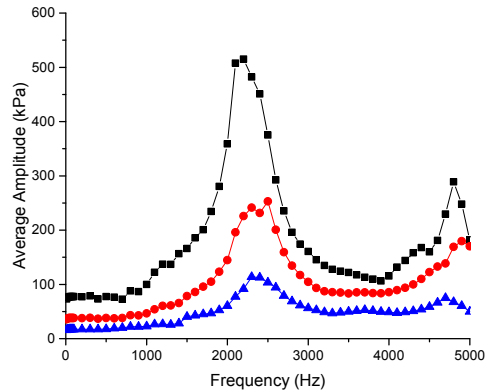
Figure 3-14: The average of 6 repeated frequency response scans of castor oil in a 200 mm tube at 5 Vpp (━■━), 10 Vpp (━●━) and 20 Vpp (━▲━).

Impact of Fluid Flow on System Response

Three flow rates were tested using as received pentane and the resulting frequency responses are shown in Figure 3-15. The difference between flowing fluid and stagnant fluid cases is attributed to the presence of bubbles. In stagnant pentane, cavitation occurs as shown in Figure 3-8a and 3-8b. With flow, bubbles are not only removed by entrainment but the pressure in the tube is a function of flow rate. Pump outlet pressure, Figure 3-15b, rises with flow rate. This increase in pressure reduces bubble size, at low flow rate, and suppresses bubble formation at higher flow rates.

Porous Media

Many of the applications of interest involve the interaction of fluids with and within porous media. Spherical silica beads were inserted into the tube to determine how the device performs with porous media. Paper filters were used to hold the beads in place with

stainless steel, O-ring sealed tubes supporting the filters. The length of the bead bed is 39 mm in water and 19 mm in toluene. Illustrative apparatus responses and images of the porous media in place comprise Figures 3-16 and 3-17. Figure 3-16a shows the frequency response through a water + air bubble filled silica bead bed. The low amplitude of the measured pressure wave is due to the attenuation of the sound through the beads and air bubbles trapped in the bead bed, as well as bead motion (Figure 3-17a). Figure 3-16b shows the frequency response through a toluene filled bead bed. The pressure fluctuations achieved for the bubble free but otherwise comparable toluene case (Figure 3-17b) are larger than those in the water + air bubble case due to the elimination of the attenuation caused by air bubbles trapped in the bed of beads but lower than achieved in the absence of porous media. Sound wave attenuation due to interaction with porous media is expected. However, output signal amplitudes consistent with those achieved in the absence of media can be achieved simply by applying larger voltages (Figure 3-17b). Bubble generation and bubble motion are readily detected from differences in amplitude and shifts in peak frequencies as per media free cases illustrated above. The motion and generation of bubbles within porous media is expected to have significant impacts on mass and heat transfer within packed beds. The quantification of the impacts of vibration, including bubble generation and motion, on mass transfer in packed beds are the focus of planned future work.
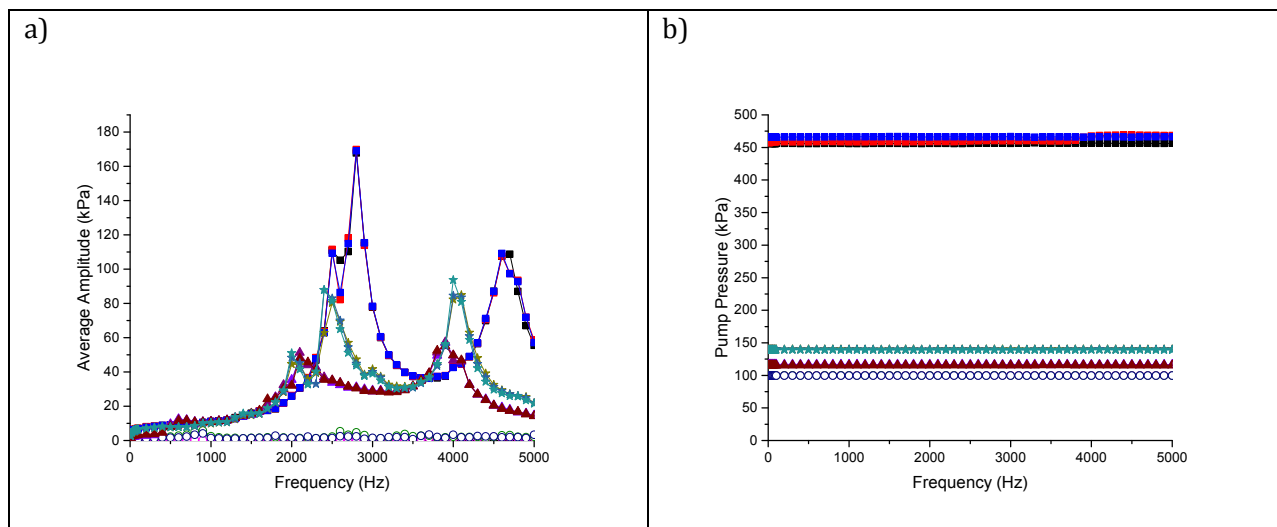
Figure 3-15: Frequency response of pentane actuated by 5 Vpp with flow through a 200 mm tube a) pressure response with flow rates of 200 mL/min (■), 50 mL/min (★), 5 mL/min (▲) and 0 mL/min (○), b) absolute pressure supplied by pump at flow rates of 200 mL/min (■), 50 mL/min (★), 5 mL/min (▲) and 0 mL/min (○).
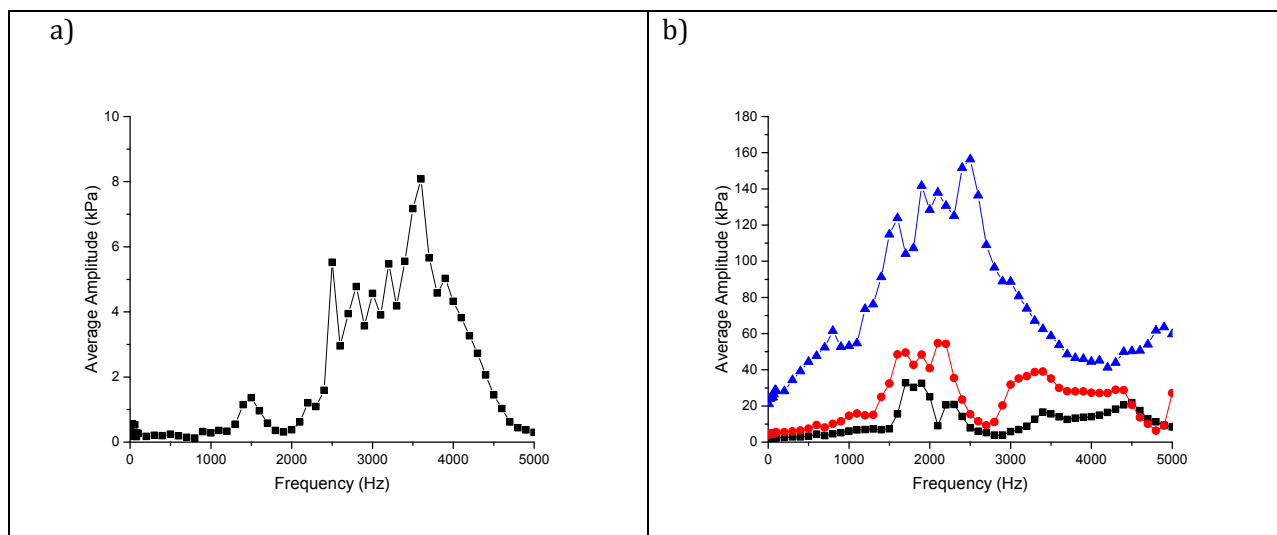
Figure 3-16: a) Average of 6 repeated frequency response scans of 250-330 μm spherical silica beads forming a 39 mm long bed in a 200 mm tube containing boiled DIUF water + air bubbles actuated by 5 Vpp, b) Average frequency response scans for 250-330 μm spherical silica beads forming an 18 mm long bed in a 200 mm tube filled with toluene actuated using a 5 Vpp (─■─), 10 Vpp (─●─) and 20 Vpp (─▲─) signal.
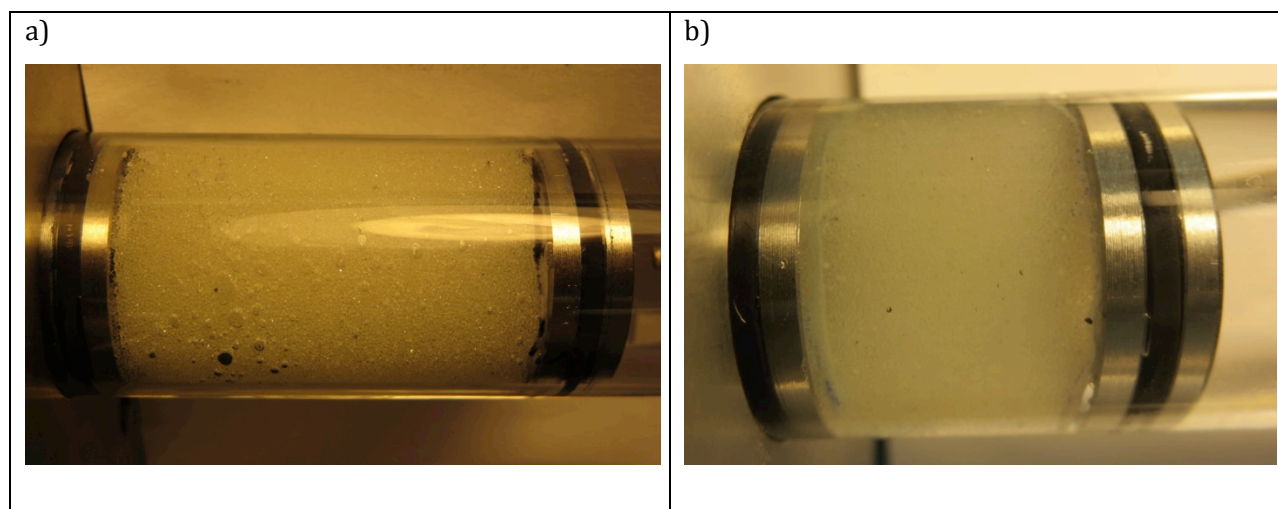
Figure 3-17: Images of a) 250-330 µm spherical silica beads forming a 39 mm long bed in a 200 mm tube containing boiled DIUF water + air bubbles, b) 250-330 µm spherical silica beads forming an 18 mm long bed in a 200 mm tube filled with toluene.

Conclusion

The design and operation of a Dynamic Pressure View Cell permitting the exploration of vibrations in fluids at industrially relevant frequencies from 10 to 5000Hz, and amplitudes of at least 80kPa and up to 500kPa is described. The DPVC fills a gap in the range of frequencies covered by existing apparatus. It is designed to facilitate visualization during assembly and operation and to permit controlled introduction or elimination of gas bubbles. Visualization of the impact of vibrations such as bubble formation, bubble motion and media motion is demonstrated down to length scale of 180µm. Flow through the transparent tubes and porous media allows for observation and control of fluid and fluid-fluid interfaces at up to 200ml/min, or greater than four tube volumes/min. Resonance was apparent and resonant frequencies are shown to depend on the fluid, the presence or generation of bubbles and the presence of porous media. Videos of fluid cavitation and the accompanying changes in the resonant response allow the device to be used to study micro bubble generation and their impact on non isotropic miscible mixtures and immiscible mixtures in porous media. Visualization and quantitative measurement of mass transfer and diffusion processes can be achieved using non-intrusive (e.g.: visible light, UV

fluorescence) and intrusive (e.g.: conductivity, resistivity) techniques. Achievement of higher amplitude pressure responses at low frequencies is an important next step as this would facilitate detailed evaluation of the impacts of large pressure variations relevant to aquifers and hydrocarbon reservoirs. Quantitative interpretation of transmitted signals is a second topic for ongoing apparatus development.

Acknowledgements

References

[1]   I. A. Beresnev and P. A. Johnson, "Elastic-wave Stimulation of Oil Production: A Review of Methods and Results," *Geophysics*, vol. 59, no. 6, pp. 1000–1017, Jun. 1994.

[2]   K. Naderi and T. Babadagli, "Pore-scale Investigation of Immiscible Displacement Process in Porous Media Under High-frequency Sound Waves," *J. Fluid Mech.*, vol. 680, pp. 336–360, May 2011.

[3]   *Guidelines for the Avoidance of Vibration Induced Fatigue Failure in Process Pipework.* Energy Institute (Great Britain), 2008.

[4]   T. Hamida and T. Babadagli, "Immiscible Displacement of Oil by Water in Consolidated Porous Media due to Capillary Imbibition Under Ultrasonic Waves," *J. Acoust. Soc. Am.*, vol. 122, no. 3, p. 1539-1555, Sep. 2007.

[5]   R. Spence and J. Amaral-Teixeira, "Investigation into Pressure Pulsations in a Centrifugal Pump using Numerical Methods Supported by Industrial Tests,"Comput. Fluids vol. 37, pp. 690–704, 2008.

[6]   M. T. Pittard, R. P. Evans, R. D. Maynes, and J. D. Blotter, "Experimental and Numerical Investigation of Turbulent Flow Induced Pipe Vibration in Fully Developed Flow," *Rev. Sci. Instrum.*, vol. 75, no. 7, 2004.

[7]   M. Qing, Z. Jinghui, L. Yushan, W. Haijun, and D. Quan, "Experimental Studies of Orifice-induced Wall Pressure Fluctuations and Pipe Vibration," *Int. J. Press. Vessel. Pip.*, vol. 83, no. 7, pp. 505–511, Jul. 2006.

[8]   "Piping Vibration Analysis & Integrity Assessment | BETA Machinery Analysis." [Online]. Available: http://www.betamachinery.com/services/piping-vibration-and-integrity-assessment.

[9]   C. V. Chrysikopoulos and E. T. Vogler, "Acoustically Enhanced Ganglia Dissolution and Mobilization in a Monolayer of Glass Beads," *Transp. Porous Media*, vol. 64, no. 1, pp. 103–121, Jul. 2006.

[10]   J. M. Thomas and C. V Chrysikopoulos, "Experimental Investigation of Acoustically Enhanced Colloid Transport in Water-saturated Packed Columns," *J. Colloid Interface Sci.*, vol. 308, no. 1, pp. 200–207, Apr. 2007.

[11]   P. M. Roberts and A. I. Abdel-Fattah, "Seismic Stress Stimulation Mobilizes Colloids Trapped in a Porous Rock," Earth Planet. Sci. Lett., vol. 284, pp. 538–543, Jul. 2009.

[12]   P. M. Roberts, I. B. Esipov, and E. L. Majer, "Elastic Wave Stimulation of Oil Reservoirs : Promising EOR Technology?," Lead. Edge, vol. May, pp. 448–453, 2003.

[13]   W. Li, R. D. Vigil, I. A. Beresnev, P. Iassonov, and R. Ewing, "Vibration-induced Mobilization of Trapped Oil Ganglia in Porous Media: Experimental Validation of a Capillary-physics Mechanism," *J. Colloid Interface Sci.*, vol. 289, no. 1, pp. 193–199, Sep. 2005.

 [14]   S. Abedi, H.-Y. Cai, S. Seyfaie, and J. M. Shaw, "Simultaneous Phase Behaviour, Elemental Composition and Density Measurement using X-ray Imaging," *Fluid Phase Equilib.*, vol. 158–160, pp. 775–781, Jun. 1999.

[15]   P. Licence, M. P. Dellar, R. G. M. Wilson, P. A. Fields, D. Litchfield, H. M. Woods, M. Poliakoff, and S. M. Howdle, "Large-aperture Variable-volume View Cell for the Determination of Phase-equilibria in High Pressure Systems and Supercritical Fluids," *Rev. Sci. Instrum.*, vol. 75, no. 10, pp. 3233–3236, Oct. 2004.

[16]   M. Khammar and J. M. Shaw, "Phase Behaviour and Phase Separation Kinetics Measurement using Acoustic Arrays," *Rev. Sci. Instrum.*, vol. 82, no. 10, Oct. 2011.

[17]   M. Cassiede and J. M. Shaw, "Non-Intrusive, High-Resolution, Real-time, Two-Dimensional Imaging of Multiphase Materials Using Acoustic Array Sensors," *Rev. Sci. Instrum.*, 2015.

[18]   J. W. Grate, C. Zhang, T. W. Wietsma, M. G. Warner, N. C. Anheier, B. E. Bernacki, G. Orr, and M. Oostrom, "A Note on the Visualization of Wetting Film Structures and a Nonwetting Immiscible Fluid in a Pore Network Micromodel using a Solvatochromic Dye," Water Resour. Res., vol. 46, no. 11, Nov. 2010.

[19]   K. Naderi and T. Babadagli, "Visual Analysis of Immiscible Displacement Processes in Porous Media under Ultrasound Effect," *Phys. Rev. E*, vol. 83, no. 5, pp. 1–14, May 2011.

[20]   L. A. James, "Mass Transfer Mechanisms During the Solvent Recovery of Heavy Oil," University of Waterloo, 2009.

[21]   B. T. Sturtevant, C. Pantea, and D. N. Sinha, "An Acoustic Resonance Measurement Cell for Liquid Property Determinations up to 250° C," *Rev. Sci. Instrum.*, vol. 83, 2012.

[22]   P. Rigord, Y. Caristan, and J. P. Hulin, "Analysis of Porous Media Heterogeneities Using the Diffusion of Pressure Waves," *J. Geophys. Res.*, vol. 98, pp. 9781–9791, 1993.

[23]   H. Muhamad, S. R. Upreti, A. Lohi, and H. Doan, "Performance Enhancement of VAPEX by Temporal Variation of Solvent Injection Pressure," *J. Pet. Sci. Eng.*, vol. 97, pp. 93–101, 2012.

[24]   E. Silberman, "Sound Velocity and Attenuation in Bubbly Mixtures Measured in Standing Wave Tubes," *J. Acoust. Soc. Am.*, vol. 29, no. 8, pp. 925–933, 1957.

[25]   R. H. Liu, J. Yang, M. Z. Pindera, M. Athavale, and P. Grodzinski, "Bubble-induced Acoustic Micromixing.," *Lab Chip*, vol. 2, pp. 151–157, Aug. 2002.

[26]   S. G. Hatzikiriakos, R. P. Gaikwad, P. R. Nelson, and J. M. Shaw, "Hydrodynamics of Gas-Agitated Liquid-Liquid Dispersions," *AIChE J.*, vol. 36, no. 5, pp. 677–684, 1990.

[27]   X. Ye, F. Pang, and A. Zhang, "Acoustic Radiation Induced by Bubble Motion in Compressible Fluid," *Appl. Math. Mech.*, vol. 35, no. 2, pp. 177–190, 2014.

[28]	B.-N. Kim, S. W. Yoon, B. K. Choi, and S.-K. Jung, "Gas Void Fraction Estimation in Gas-Bubble-Contained Sands with Difference Frequency Waves," *Jpn. J. Appl. Phys.*, vol. 51, Jul. 2012.

[29]	E. W. Lemmon, M. O. McLinden, and D. G. Friend, "NIST Chemistry WebBook, NIST Standard Reference Database Number 69," P. J. Linstrom and W. G. Mallard, Eds. Gaithersburg MD, 20899: National Institute of Standards and Technology.

[30]	B. E. Treeby, B. T. Cox, E. Z. Zhang, S. K. Patch, and P. C. Beard, "Measurement of Broadband Temperature-Dependent Ultrasonic Attenuation and Dispersion Using Photoacoustics," *IEEE Tansactions Ultrason. Ferroelectr. Freq. Control*, vol. 56, no. 8, pp. 1666–1676, 2009.

[31]	J. M. Shaw, "A Microscopic View of Oil Slick Break-up and Emulsion Formation in Breaking Waves," *Spill Sci. Technol. Bull.*, vol. 8, no. 5–6, pp. 491–501, 2003.

[32]	A. B. Wood, *A Textbook of Sound*. London: G. Bell and Sons Ltd., 1930.

[33]	S. N. Domenico, "Acoustic Wave Propagation in Air-bubble Curtains in Water- Part I : History and Theory," *Geophysics*, vol. 47, no. 3, pp. 345–353, 1982.

[34]	T. G. Leighton, J. Walton, and M. J. W. Pickworth, "Primary Bjerknes Forces," *Eur. J. Phys.*, vol. 11, pp. 47–50, 1990.

Chapter 4: On Vibration Induced Fluid and Particle Motion in Unconsolidated Porous Media—Observations and Dimensional Scaling Analysis

Robert A. Stewart, John M. Shaw.

Introduction

Fluid flow in porous media is a common aspect of industrial and environmental processes as well as the associated small-scale laboratory analogues used to study them. Single and multiphase flow in packed bed reactors and hydrocarbon reservoirs, contaminant plume movement in aquifers, and geological carbon dioxide sequestration comprise a sample of the range of applications. Vibrations at time scales causing bubbles to form or causing bubble and liquid motion can occur in all of these settings due to attached or near by machinery and flow as shown in Chapter three and [1]. Despite this, impacts of vibration on fluids within porous media (fluid movement, interfacial heat and mass transfer) have received limited attention [2–4]. Vibrations are imparted directly to fluids or are transmitted to them through supports and pipework at industrial sites, or in the case of environmental or geological applications through the solid medium. It is well known that vibrations at specific frequencies impact fluid flow and velocity profiles for cases as diverse as blood flow in arteries [5, 6] and oil flow in consolidated porous media [7, 8]. Both applied and naturally occurring vibrations, such as earthquakes, across a large range of frequencies have been the subjects of research related to hydrocarbon reservoirs [8–11].

Hydrocarbon reservoir studies have typically focused on consolidated media and the impact of vibration on displacement of entrapped liquid oil ganglia [7, 12–15] over a broad range of frequencies. Impacts of compressible fluids or bubbles on flow or mass transfer have not been explored in detail. Topics addressed to date related to the current work

include snap-off of non-wetting fluid ganglia in both pressure driven and gravity driven flow linked to behaviors in oil reservoirs, contaminant movement in aquifers and carbon dioxide sequestration [7, 16–20]. The dynamics of snap-off occur due to the different time scales associated with the balancing of interfacial forces and applied forces and is exhibited by the Haines jump phenomenon [18, 21]. These dynamics are influenced by seismic waves as well. Seismic events can dislodge trapped non-wetting fluids [12, 18]. Field experiments on enhanced oil recovery have covered a large range of vibration sources such as surface mounted oscillators, vibrations from nearby trains, earthquakes and even explosions [9, 22]. The results from these field experiments have been inconclusive with some reservoirs performing differently (both quantitatively and qualitatively) from others. Micro bubbles and gas content, neither controlled nor reported in these experiments, are present in many oil reservoirs and aquifers and their movement is important for applications as diverse as solution gas drive and carbon sequestration [20, 23]. The lack of clear outcomes from the vibrationally stimulated reservoir experiments may be attributable to impacts, or to the variability of the impacts of vibration induced bubble–fluid–solid medium interaction.

Unconsolidated media introduce additional variables and arise in diverse applications from packed bed reactors, to sediment layers important to hydrology, and in globally significant hydrocarbon reservoirs such as the Athabasca bitumen deposits in Alberta, Canada. The impacts of vibration on behaviors of fluids in unconsolidated porous media have received limited attention [22]. However, known impacts of vibration (in the 30-150 Hz range [25]) include enhanced interstitial velocity of colloidal particles where the largest observed change in colloidal transport occurred at 30 Hz. This outcome can be attributed to a change in the local flow pattern within the pore space as anticipated from the Womersley number [5–7] (Equation 4-1). An alternative potential attribution is media movement causing a peristaltic like pumping effect between particles. Vibrating cylindrical columns, with up to 25 volume % solids at 30 to 60 Hz have been shown to reduce gas bubble rise velocity and to enhance gas–fluid mass transfer [25, 26]. Bubbles or a gas phase present in a consolidated porous medium facilitate drainage of viscous liquids when the medium is

vibrated between 1 and 100 Hz [22, 27]. This phenomenon can also be expected to occur in unconsolidated media.

Brief Review of Bubble–Fluid Interactions in Porous Media

While it is well known that vibrations in liquids cause bubbles to form, to oscillate in size and shape, and to move, the impacts of these phenomena _collectively_ on dynamic force balances in porous media have not been evaluated systematically in the open literature. In this brief review of bubble–fluid interactions in porous media, system dimensions or continuous phase dimensions are assumed to be much larger than the diameter of individual pores. Drop and bubble leading dimensions are expected to be of the order of pore diameters, although larger dispersed fluid domains are not specifically precluded in the analysis. Known impacts of vibration on fluids in bulk liquids and porous media along with relevant dimensionless groups and key dimensional variables are illustrated in Figure 4-1. Vibration can alter the velocity profile of a liquid flowing through a porous medium, the shape of a trapped second liquid phase, the size of bubbles and the static nature of the solid medium itself. Characteristic times resulting from comparisons among forces acting on the system of interest are used to determine relevant frequency (period of vibration) and length scales where specific mechanistic impacts arise [7]. The pore scale can be viewed as a characteristic length scale for phenomena acting within a porous medium. The periods of vibrations can be used as the time scale of interest as seen in Chapter three. Characteristic times can be made non-dimensional using the period of the applied frequency but for visualizing comparisons among the different mechanisms and vibration sources it is useful to keep them dimensional. These characteristic times define limits for the impacts of specific mechanisms. The frequency range of vibrations commonly found in industrial and natural environments covers a range from 10 Hz to 5000 Hz. As this range spans the range of frequencies known to impact flow in porous media [9, 22], their presence and amplitude influence outcomes from otherwise similar laboratory facilities through to oil and gas reservoirs and aquifers. Definitions for the characteristic parameters referred to in Figure 4-1 and elsewhere in this work include:

Womersley number [5, 6]

$$Wo = D \sqrt{\frac{\omega \rho_0}{\mu}}$$

Equation 4-1

Viscous diffusion time [7]

$$\tau_{viscous\ diffusion} = \frac{\rho D^2}{\mu}$$

Equation 4-2

Viscous response time [7]

$$\tau_{viscous\ response} = \frac{\mu D}{\sigma}$$

Equation 4-3

Inertial response time [7]

$$\tau_{inertial\ response} = \sqrt{\frac{\rho D^3}{\sigma}}$$

Equation 4-4

Bubble resonant frequency [28]

$$f_{bubble} = \frac{1}{\pi D} \sqrt{\frac{3kP_0}{\rho_0}}$$

Equation 4-5

Sound intensity attenuation [29]

$$I = I_0 exp\ (-2\alpha x)$$

Equation 4-6

where D is the bubble or tube diameter, ω is the angular frequency of the oscillation, ρ and ρ_0 are the densities of a liquid drop and the continuous liquid phase respectively, μ is the dynamic viscosity of the liquid, σ is the interfacial tension between two liquids, k is the ratio of specific heats of the gas bubble, P_0 is the average pressure in the continuous fluid, α is the attenuation coefficient, x is the distance from the location of a known sound intensity I_0.

Impact of Vibration on the Velocity Profile of a Single Phase Fluid

Dimensional analysis of a single-phase fluid in a channel exposed to an oscillatory pressure gradient, leads to a dimensionless group analogous to Reynolds number (ratio of inertial and viscous momentum transfer in a flowing fluid) but for oscillatory flow. The Womersley number, Equation 4-1 [5, 6], is related to viscous diffusion time, Equation 4-2, and indicates whether or not a stable velocity profile has time to develop in a time dependent pressure gradient. A Womersley number much less than 1 means the fluid in a pore has time to respond to the instantaneous pressure gradient resulting in a quasi-steady state parabolic velocity profile expected for laminar flow with a similar magnitude static pressure gradient [7]. For Womersley numbers greater than 1, the applied frequency has a period shorter than the time required to establish a stable velocity profile, and a more plug like velocity profile develops within pores. The plug shape develops because there is not enough time for momentum to increase in the center of the channel before the applied pressure gradient is removed.

Impact of vibration on:	Low Frequency/short length scales	High Frequency/ long length scales	Characteristic parameter
a) Velocity profile of a single phase fluid			Womersley number Eq. 4-1, and viscous diffusion time Eq. 4-2 [5, 6]
b) Drop deformation in a continuous liquid phase			Viscous and inertial response times Eq. 4-3,4- 4 [7, 12]
c) Bubble compression and motion			Bubble resonant frequency Eq. 4-5 [28]
d) Unconsolidated Media motion			Force balance
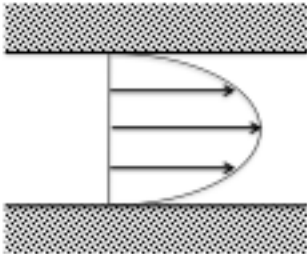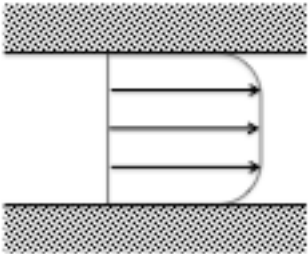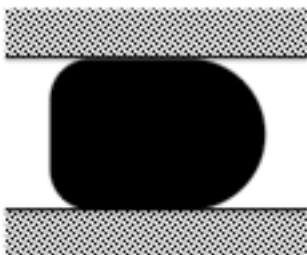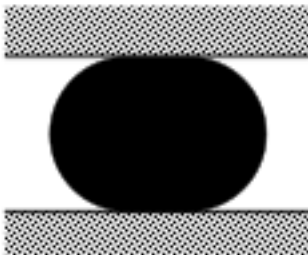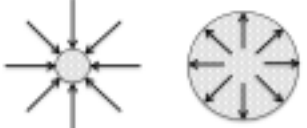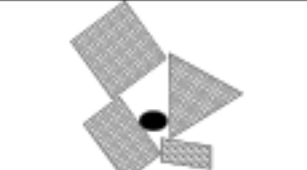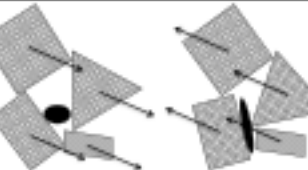
Figure 4-1: Phenomena known to occur in fluid media systems exposed to vibration: a) velocity profile variation, b) dispersed fluid drop shape change, c) size oscillation of gas bubbles, d) local unconsolidated medium acceleration.

Impact of Vibration on Drop Deformation

The shape and motion of incompressible liquid drops within a bulk fluid are governed by: interfacial forces, internal and external viscous forces, inertial forces and gravitational forces. Interfacial forces attempt to minimize external surface area. Small drops

surrounded by a continuous liquid are spherical. In porous media drops are often forced into non-spherical shapes by the pore walls. The dispersed liquid drop is viscous and therefore changing the shape of the drop causes energy dissipation. Drops have inertia that must be overcome to change their shape and location. If a drop diameter is significantly smaller than the wavelength of the applied vibration, the applied pressure can be considered as a constant but time varying value [30]. Drops are also subject to gravity.

A disturbing force, in this work introduced by vibration, must overcome interfacial, viscous, inertial and gravitational forces to cause a change in drop shape or location. Gravity acts in a certain direction relative to the plane of reference where as viscous and inertial forces resist all changes of motion. Interfacial or capillary forces resist increasing surface area. Under a sustained pressure gradient drops deform and achieve new steady state conditions. When exposed to an oscillating pressure gradient, drop deformation occurs via the same mechanisms but due to the oscillatory nature of the pressure, the shape change achieved is dependent on the frequency and amplitude of the pressure fluctuation. The time it takes to deform must be smaller than the duration of the applied pressure for the same deformation to occur in a dynamic pressure gradient as occurs in a static pressure of the same magnitude. The ratio of the restoring interfacial tension to the viscous force and to inertia provide a viscous response time, Equation 4-3, and an inertial response time, Equation 4-4, respectively. For a pressure fluctuation to cause a change in drop shape, the period of the oscillation must be much larger than the viscous and inertial response times [7]. Oscillatory pressure forces with a period much larger than both response times have been observed to overcome capillary pressure allowing an oil ganglia to move through pore constrictions [12]. This is important because high amplitude oscillatory pressure gradients can be generated under conditions where static pressure gradients cannot be sustained due to flow constraints. Vibratory stimulation aligns well with capillary theory where fluid drops move over time in alternating steps by rheons or Haines jumps and isons. Morrow describes Haines jumps (rheons) as periods of fluid redistribution driven by surface energy reduction at constant saturation and isons as periods of pressure driven displacement between rheons [21]. Vibration causes an oscillating pressure driven deformation of drops (isons), illustrated in Figure 4-1b, that is followed by rheons when the drops change shape

due to a redistribution of surface energy. Isons and rheons can also push drops away from the source of a vibration.

Impact of Vibration on Bubble Compression and Motion

Bubbles have negligible internal mass and viscosity compared to liquid drops but they are compressible and oscillate in size as the surrounding pressure fluctuates. Bubbles have a resonant frequency, Equation 4-5, related to the average pressure and density of the surrounding fluid. Bubbles smaller than the resonant frequency compress and expand in phase with the applied pressure, and in standing waves they move up the pressure gradient due to the Primary Bjerknes force [31]. In non-standing waves, all bubbles are pushed away from the source. Resonant bubbles have the largest change in size over a period of oscillation. This causes the greatest dampening of the applied vibration and the energy dissipated causes bubbles to heat. In sonochemistry, the applied pressure gradient is large enough to cause the fluid to vaporize during the low-pressure part of the wave. Small bubbles grow by rectified diffusion and heat as they approach the resonant frequency [29]. With large enough pressure amplitudes, bubbles can collapse. Bubbles closer to resonance are more likely to collapse. This collapse can cause localized impingement on a surface through jetting and in the bulk fluid causes localized heating [29]. Bubble generation, growth and collapse are known collectively as vibration or sonic induced cavitation. Cavitation can be used for cleaning and to cause reactions and is commonly achieved with ultrasound. The use of ultrasound is limited to short distances from a source because the sound intensity decreases with the square of the frequency and exponentially with distance from the source as shown in Equation 4-6 [29, 32].

Unconsolidated Media Motion

In fluid-filled consolidated-solid media, one rotational wave and two dilational waves travel though the media due to stress strain relationships in the coupled liquid–solid system, as described by Biot theory [32]. Biot theory was developed for consolidated media and therefore assumes any motion of the media is a strain due to an applied stress. In unconsolidated media, the applied stress can cause particles to translate or rotate. This

introduces additional attenuation mechanisms and interactions with the fluid that are not observed in consolidated media. These additional degrees of freedom permit additional phenomena and additional interactions among phenomena to occur.

The instantaneous applied force acting on an individual particle is the integral of the local pressure over the surface area imparted by the pressure wave. The resulting instantaneous acceleration can be compared to that of gravity to obtain a qualitative comparison. This comparison is also useful in considering motion of particles within the fluid. For further qualification, the acceleration can be characterized by the displacement of a wall in the system, similar to the cone in a sound system speaker. With a known displacement and frequency, the acceleration of the system can be calculated. This is useful for quantifying local accelerations using non-intrusive measurements as well as for understanding what phenomena are possible at certain length and time scales. By adding vibration induced acceleration to gravitational acceleration in the Bond number, a comparison between gravitational and interfacial forces governing separation kinetics, is one way to leverage existing phenomenological understanding to vibrating systems.

Integrated Perspective on the Impacts of Vibration in Unconsolidated Porous Media

Interactions among the effects of vibration on flow in unconsolidated porous media introduce significant complexity to modeling and experimental studies, even if common variables such as media size distribution and shape variation, media surface property heterogeneity/variability, surfactants and fluid composition uncertainty, and thermal gradients are ignored or held constant. The relative importance of the phenomena outlined in Figure 4-1 is best illustrated using examples based on relevant length scales within unconsolidated media at time scales related to vibration frequencies of interest. The particulars of the examples presented in Figures 4-2 – 4-6 link with the pore size range, fluid properties, and frequency ranges relevant to the experimental section of this work and should be considered illustrative. The scaling procedure used is a general one and it can be used to visualize active transport phenomena in other applications. The boundaries indicated by dimensionless groups or response times are not precise, they provide order of

magnitude estimates for transitions between regimes. If a particular application falls within an order of magnitude of a boundary, the system response is intermediate. This is similar to how Reynolds numbers are interpreted in pipe flow. In pipes, Reynolds numbers between 2300 and 10000 are considered transitional between fully laminar (below 2300) and fully turbulent (above 10,000) flow [33].

The locus of frequencies and length scales where the Womersley number is equal to one, based on the properties of liquid water at 298K, are presented in Figure 4-2 along with the pore diameter of interest, in this case $\sim$ 100 μm. In small pores, the continuous fluid phase has time to develop a parabolic profile irrespective of frequency. In large pores, the velocity profile does not have sufficient time to develop a parabolic profile irrespective of frequency. For pores with a diameter of $\sim$ 100 μm velocity profiles are expected to deviate from a laminar profile above $\sim$ 10 Hz. At higher frequencies plug like flow develops because there is insufficient time for the larger momentum change along the centerline of the channel to occur [5]. This is of significant interest because boundary layer thickness and velocity gradients within a boundary layer impact interfacial mass transfer.

Figure 4-3 shows the viscous response time, Equation 4-3, and inertial response time, Equation 4-4, equal to the period of the applied vibration (1/frequency) for a 1-methylnaphthalene (1MN) drop in liquid water at 298 K. The interfacial tension between the two liquids, measured using a Ramehart Model 250 goniometer, is 37.2 mN/m at 298 K and 1.01 bar. The viscosity and density of 1MN, 2.8 mPa*s and 1016.3 kg/m^3 respectively, were obtained from the DIPPR database [34]. The viscous response and inertial response curves together suggest that 1MN drops with a diameter equal to the pore diameter, $\sim$100 μm, have interfacial forces large enough to overcome both the inertial and viscous forces. The viscous and inertial response curves suggest that below $\sim$4000 Hz 1MN drops have time to respond completely to the applied oscillating pressure gradient. This means that 1MN drops oscillate around a static equilibrium shape up to $\sim$4000 Hz; at high frequencies 1MN drops do not respond to vibration [7, 12].

Figure 4-4 shows that the resonant frequency of an air bubble in water at 298 K and 1.01 bar is much larger than the pore scale over the frequency range of interest. Bubbles within ∼ 100 μm pores are expected to oscillate in phase with the applied frequency and to move away from the vibration source [31]. Large bubbles spanning multiple particles and pores can and do form in particulate porous media. Resonant frequencies, estimated using Equation 4-5, assume that bubbles are spherical and surrounded by liquid, and that they compress isothermally. Equation 4-5 is inaccurate for non-spherical gas bubbles and bubbles attached to nucleation sites. Consequently, it is only expected to provide order of magnitude estimates for bubbles of comparable volume formed in a particulate porous medium. The validity of this assertion requires further testing—a subject of a future work.

Figure 4-5 shows the vibration amplitudes (displacements) required to generate a 1 g acceleration (9.81 m/s^2). Clearly, motion of particles in unconsolidated media is expected unless low frequency and low amplitude vibrations are applied. The particles of interest in this work possess diameters of the order 100 μm. Thus, local accelerations greater than 1 g arise at frequencies above ∼ 50 Hz, even if the amplitude of the applied vibration is below ∼ 100 μm.

Attenuation of the applied vibration can be calculated using Equation 4-6 with the attenuation coefficient, α, dependent on the attributes of the system and applied frequency [29]. The phenomena described above contribute to the attenuation, highlighting this dependence. Vibrations with frequencies between 0.2 and 80 Hz are regularly used for local seismology over distances of hundreds of meters [35] and ultrasound with frequencies in the MHz range are used for solid component non-destructive testing on the order of a few centimeters [36]. This suggests that vibrations with frequencies from a few hertz to megahertz may play a role in experimental apparatus while, due to higher attenuation of high frequency vibration, only lower frequencies up to a few hundred hertz are important at geological length scales.

These phenomena are superimposed in Figure 4-6 and the frequency and length scale ranges where they overlap and can potentially interact are shown. Clearly, in industrial

and laboratory settings vibrations can cause variable velocity profiles, dispersed drop deformation, bubble oscillation and motion to occur in porous media. Unconsolidated media motion can also occur over broad ranges of applied frequency and amplitude. While the details vary with fluid properties, the calculation approach and conceptual outcomes are valid irrespective of the application. Typically each of these phenomena is investigated in isolation. Investigation of how they interact at the pore scale, the identification of which phenomenon dominates and what new phenomena occur for given sets of fluid properties and conditions within unconsolidated media, as a function vibration frequency and amplitude, comprises a whole field of study with numerous open questions. The balance of this contribution focuses on observation of bubble–fluid–media interactions. Experimental observation of these interactions required the development of equipment, observation techniques and procedures. Each is described, and bubble–fluid–media observations are interpreted based on the analysis presented above with an emphasis on phenomena arising far from, near, and at, bubble resonance.

Experimental

Materials
97+% 1MN, was supplied by ACROS Organics. 1MN fluoresces (blue) under ultraviolet light. De-ionized ultra-filtered water was prepared in the laboratory. 99+% pentane was supplied by Sigma Aldrich. Pyranine, a water-soluble fluorescent (green) dye, was extracted from commercially available highlighters.

The unconsolidated medium comprised black Exo Terra Desert Sand. The particle size distribution was determined using sieve analysis and is shown in Figure 4-7. The sieves (W.S. Tyler mesh sizes 48, 60, 65, 100, 140, 200 and 53 µm) and Rotap sieve shaker (W. S. Tyler, RX-29-Can) were operated for 5 minutes with three separate samples of sand, each measured three times. The small variation among all of the measurements suggests that the measurements are both repeatable and reproducible. Figure 4-7 shows that the D50

(sieve size where 50% of cumulative mass has passed through) of the sand is between 210 and 250 μm. This is close to the D50 of high grade Athabasca oil sands which has a peak in the particle size distribution at 180 μm [37].
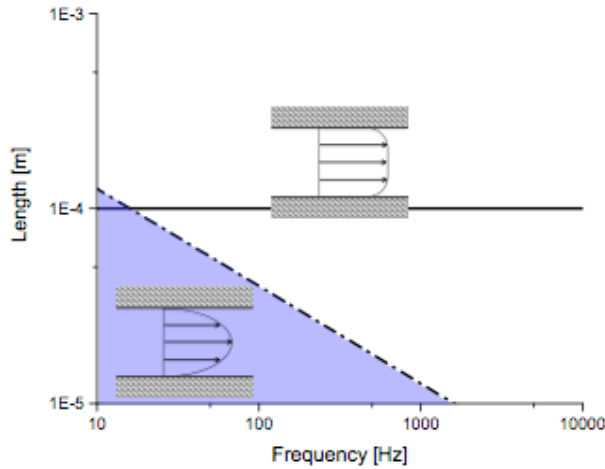
Figure 4-2: Combinations of length scale and frequency corresponding to the boundary between parabolic and plug like velocity profiles based on the properties of liquid water at 298 K and 1.01 bar and a Womersley number (Equation 4-1) equal to one (−•). The horizontal solid line indicates the nominal pore scale (100 μm).
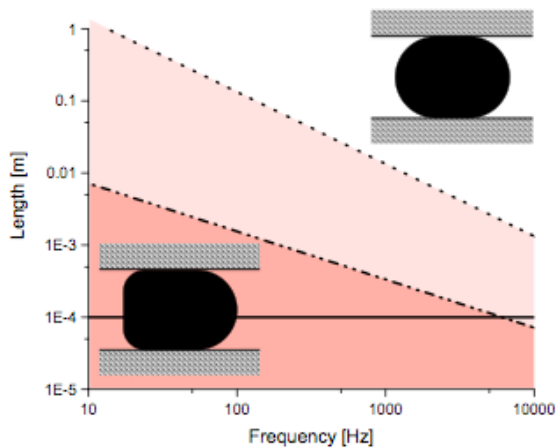
Figure 4-3: Dispersed drop shape regimes defined by viscous response time (•••) (Equation 4-3) and inertial response time (−••) (Equation 4-4) for a 1MN drop within a continuous liquid water phase at 298 K. The horizontal solid line indicates the nominal pore scale (100 μm).
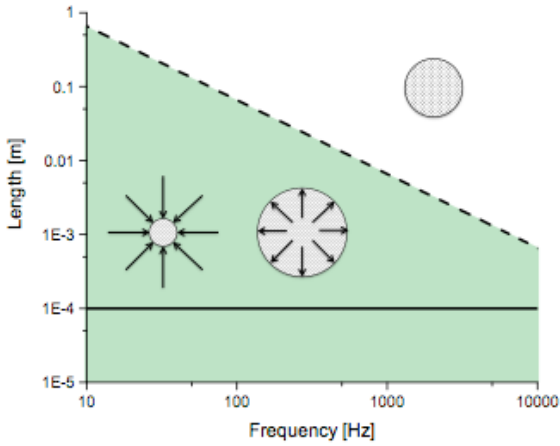
Figure 4-4: The resonant diameter of an air bubble in water at 298 K and 1.01 bar (−−−) (Equation 4-5). The horizontal solid line represents the pore scale of 100 μm. Below the bubble resonant diameter, bubbles oscillate in phase with the applied frequency. Above the resonant diameter bubbles oscillate out of phase and deform non-uniformly.
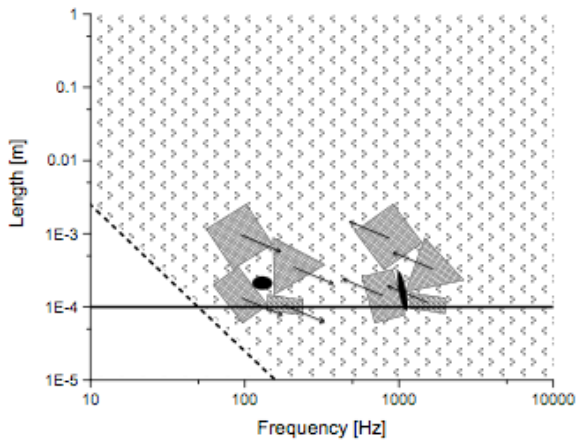
Figure 4-5: Displacements generating accelerations greater than 1 g (shaded area), displacements generating 1 g (---). The horizontal solid line represents a particle diameter of 100 μm.
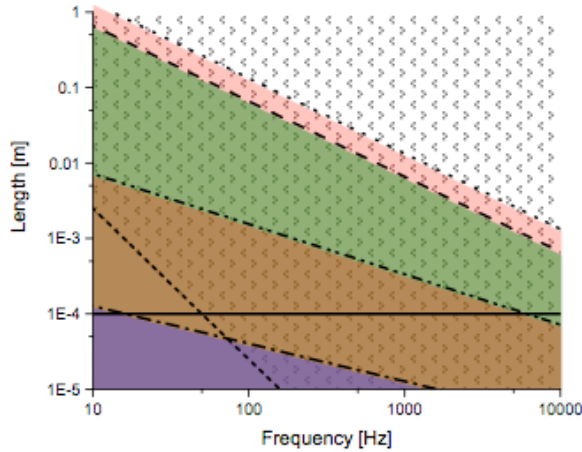
Figure 4-6: Length scale and frequency ranges where displacement mechanisms shown in Figure 4-1 a-d and elaborated in Figures 4-2 – 4-5 overlap for water, and 1MN drops and air bubbles in water at 298 K and 1.01 bar. The horizontal solid line indicates the nominal pore scale (100 μm).
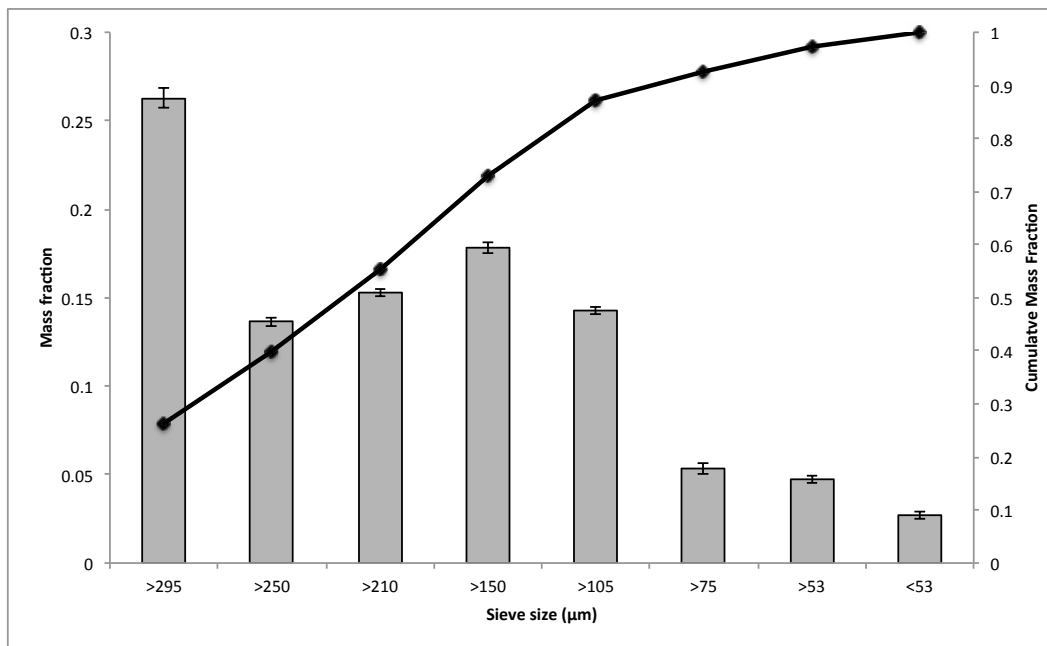
Figure 4-7: Cumulative (black curve) and sieve bin (histogram) particle size distributions for black Exo Terra Desert Sand. The error bars reflect the maximum and minimum measured values.

Apparatus

Experimental studies of fluid flow with and without vibration in porous media typically focus on 2 dimensional micro-models or consolidated media [11, 38, 39]. Some studies with unconsolidated media make use of Magnetic Resonance Imaging, ultrasound and x-ray tomography [39]. These techniques have limited spatial or time resolution relative to the phenomena noted in Figure 4-1. Planar Laser Induced Fluorescence (PLIF) is a very useful tool as it allows real time 3-D imaging provided stringent index of refraction matching is feasible [40, 41]. PLIF is best used for studies testing specific hypotheses in detail with well-known system parameters.   For exploratory work, visual models are usually the easiest to implement but significant customization is required to image miscible phases at the pore scale, or to target specific frequency ranges. The general design features and operation of the Dynamic Pressure View Cell (DPVC) are described in detail in Chapter three. Briefly, the DPVC consists of a glass tube with a set of actuated bellows at one end and a pressure sensor at the other end. In our prior work, we used a piezoelectric actuator to generate high-pressure amplitude sound waves from 500-5000 Hz. As the frequencies of interest in this study also include 10-500 Hz, additional components were added to broaden the frequency range, to hold and compact a bed of unconsolidated media, and to provide UV fluorescent imaging of fluid movement and flow within porous media. These new features are described here. To obtain frequencies in the 10-120 Hz range, the piezoelectric transducer (Physiks Instruments, P840.40) described in Chapter three, was replaced with a solenoid pump (Fluid-o-Tech, Mono Series IF coil) that was modified to allow it to connect to the DPVC stand and bellows. The induction coil and piston were the only components of the solenoid pump used. O-rings and steel spacers replaced the springs to limit the displacement amplitude of the vibration. Metal plates were used on the end of the induction coil to contain the piston, O-rings and spacers. The modified solenoid pump was driven by a single-phase Variable Frequency Drive (VFD) (Eaton, PowerXL DC1-S17DONN-A20N). The actuator drives the bellows from 0 Hz up to the upper operating limit of the VFD (120 Hz). Example peak-to-peak frequency responses are shown in Figure 4-8.

An insert was constructed to hold the sand bed in place as well as to compact the bed. The insert comprises two plugs with wire mesh screens connected by a screw, as shown in Figure 4-9. Each plug is made of seven parts: a steel ring with an O-ring groove on the OD and two threaded holes drilled axially, a wire mesh screen with a passing size of 30-35 μm (Belleville Wire Cloth, SS304L 80x700 mesh) with two holes for the connecting screws and a central hole for the main screw, a second ring with unthreaded holes for the connecting screws, and an end piece with a central threaded hole for the main screw and two unthreaded holes at the ends for connecting screws, an O-ring, and two connecting screws. The main screw connects the plugs with a central screw and it is used to compact the bed by reducing the gap between plugs during assembly. The central screw can have a hole drilled through it to allow a fluid adjustment line access to the bellows side of the bed.

A custom UV fluorescence system was developed and implemented to capture the interactions among the solid media, fluids and bubbles. Two high bay light fixtures (Lithonia, IBZT8 4) with 4 black light T8 bulbs each (Symban, 48", F32T8/BLB) were fastened to a stand at 90 degrees to each other and 45 degrees from horizontal. A camera was placed between the fixtures. Visible light was blocked by placing the apparatus in a custom blackout tent. To prevent reflection of the fluoresced light black felt was placed behind and over the frame of the DPVC. Time lapsed images of the bed were captured using a Nikon D810 digital camera with an AF-S 105/2.8 macro lens tethered to a PC using a USB 3.0 cable. Image capture control was adjusted using DigiCamControl, version 1.2.89.0. Images were captured and stored every 6 seconds (upper limit of the data transfer rate). Nikon software (ViewNX 2, version 2.10.0) was used to view the images and to convert the RAW file format to 16 bit Tiff images used for image processing and stop-motion time-lapse video creation. A custom MatLab (R2014a) code was written to crop images, to separate out blue, green and red images from the RGB image, to subtract intensity distributions in an image from a reference image, to remap the intensities of individual colours onto an RGB image to highlight fluorescence gradients. Example images of 1MN and dyed water are shown in Figure 4-10. Examples of 1MN + water + air bubble images and their rescaled counterparts are shown in Figure 4-11. The selection of fluids and solids was made with fluorescence imaging in mind. 1MN, fluoresces (blue) under UV

light. Pyranine a green fluorescent dye, was added to water to maximize the contrast with 1MN and to facilitate the use of colour separated images. The black sand prevented transmission of fluoresced light and increased image contrast.
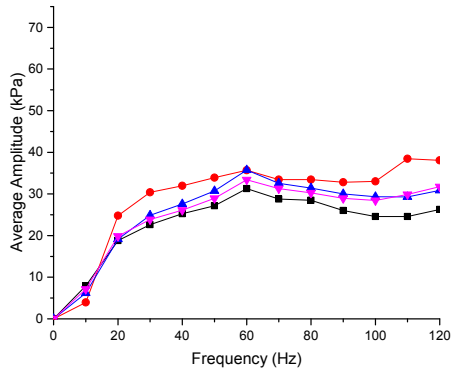
a)
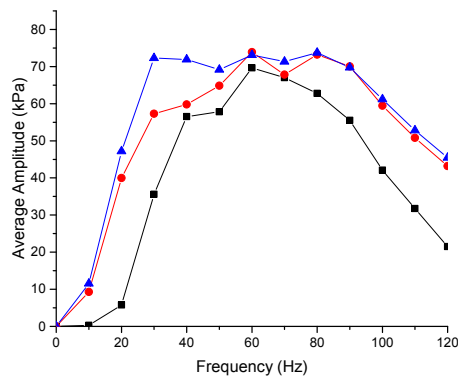
b)
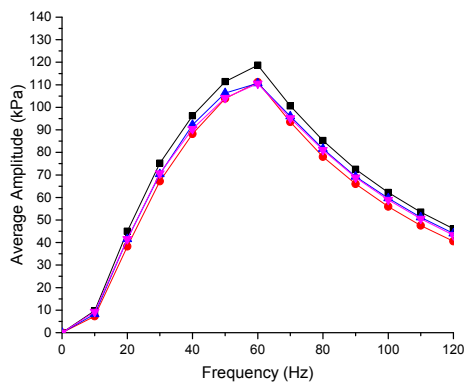
c)

Figure 4-8: Transmitted Peak-to-peak pressure signals obtained using the solenoid actuator and VFD with a 200 mm long tube in the DPVC filled with a) pentane, b) De-Ionized Ultra-Filtered (DIUF) water, and c) castor oil.
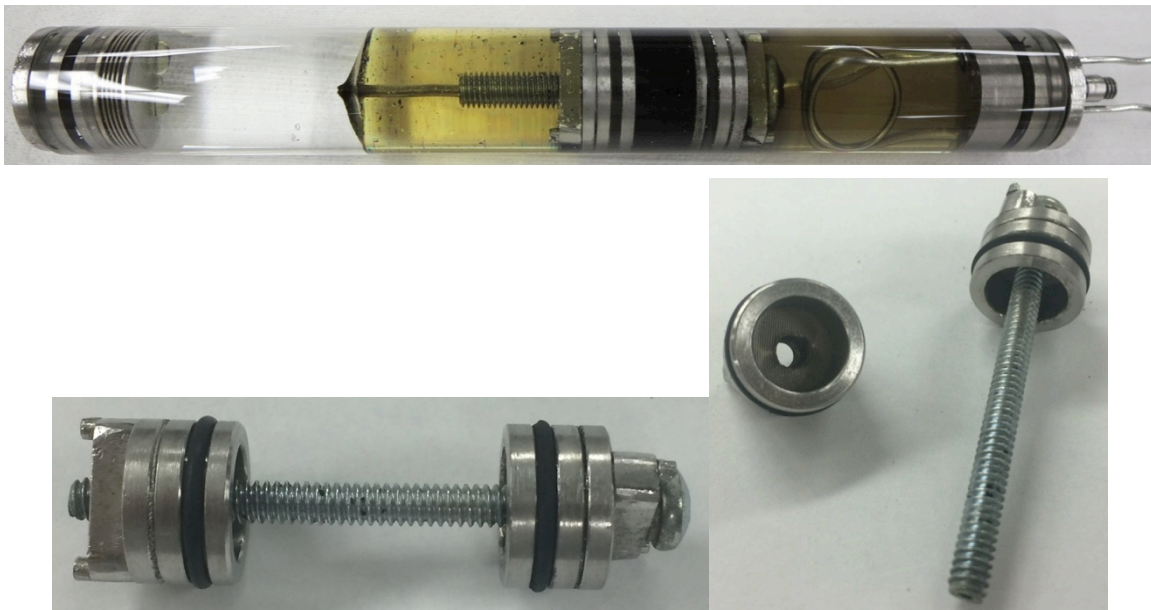
Figure 4-9: DPVC tube insert prior to insertion and inside the tube filled with, from left to right, water, 1MN, compacted black sand saturated with 1MN, and 1MN.
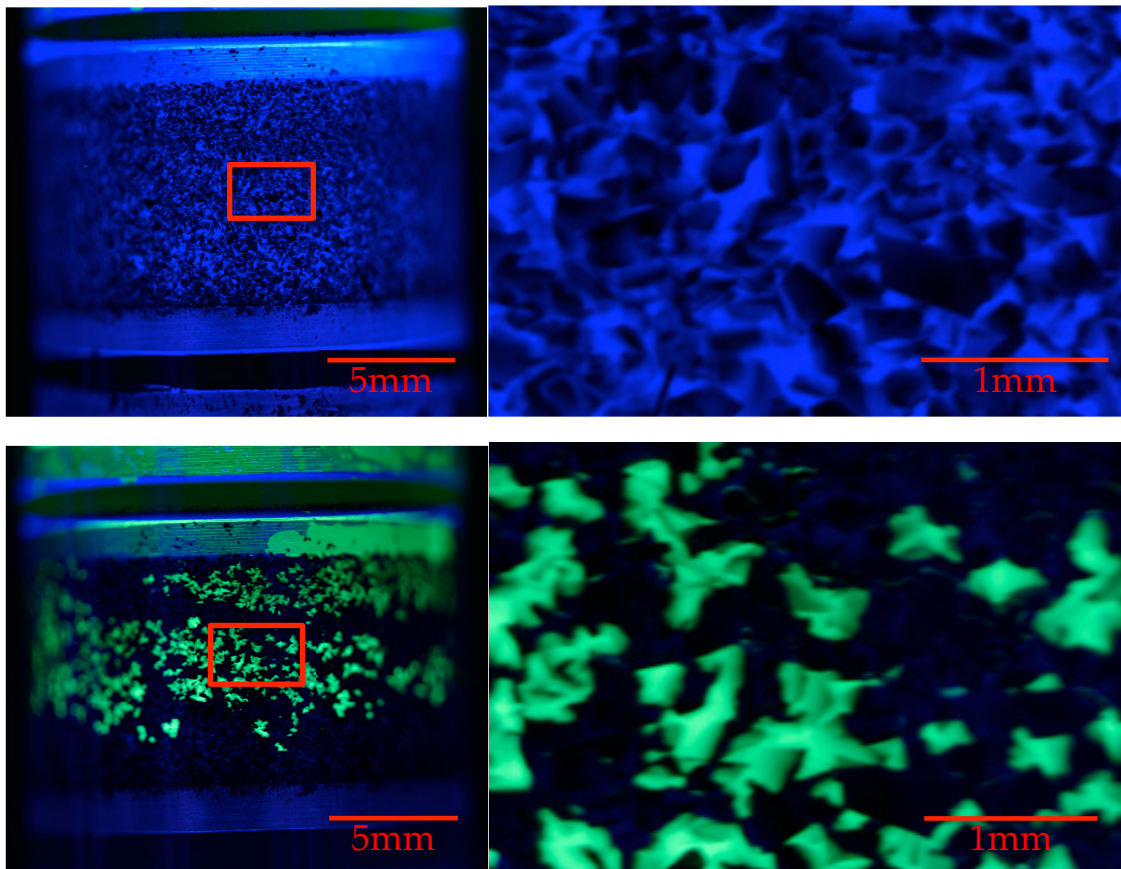
Figure 4-10: Low and high magnification UV fluorescence images of 1MN (blue) and pyranine dyed water (green) in black sand.
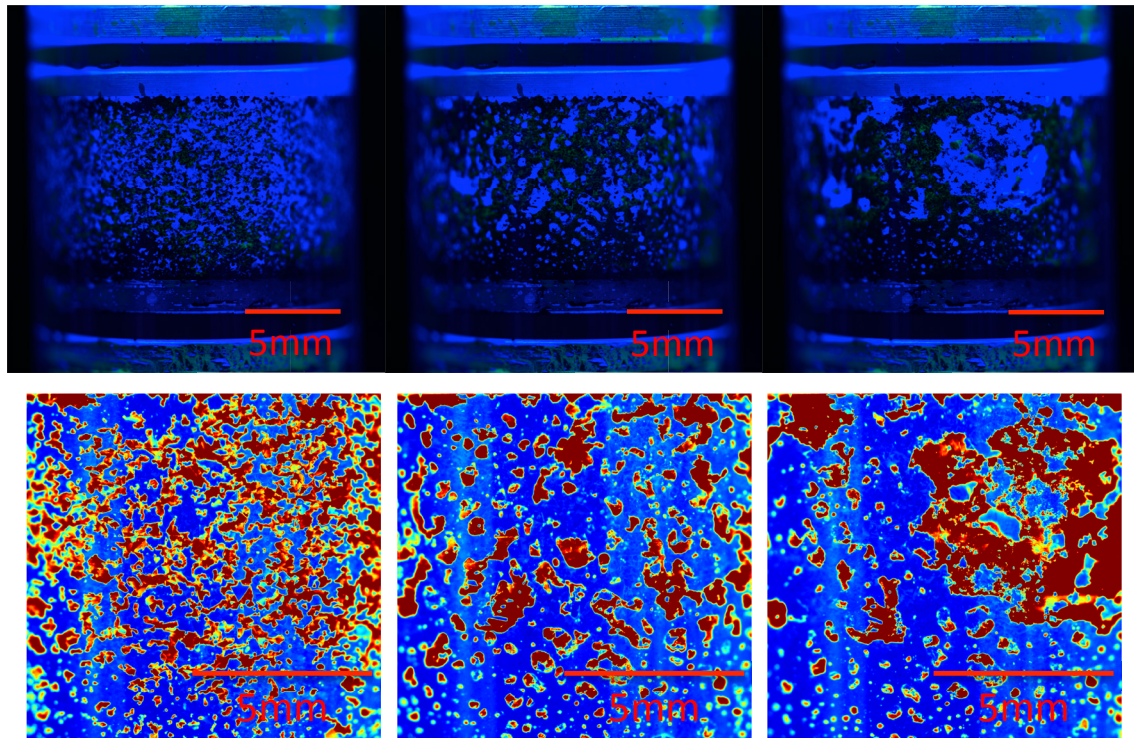
Figure 4-11: Bubbles moving through a water wetted sand pack that was then saturated with 1MN. The top row of images are RGB images, taken 6 minutes apart. The lower row of images are the same images with the blue component rescaled over an RGB colour map (MatLab R2014a, jet colour map) to highlight the local changes in intensity of 1MN with time. In the lower row, red corresponds to high intensity fluorescence for 1MN with reduced fluorescence intensity mapped across the colour spectrum to blue representing non-fluorescing areas (sand grains).

Unconsolidated Medium Preparation and Properties

Care was taken to prepare a compacted bed of sand filled with and surrounded by a specific fluid. The bellows were immersed in a desired fluid then inserted into the tube to avoid having air bubbles attach to them. The bed of sand was prepared by inserting one of the two insert plugs, Figure 4-9, into the open end of the tube. The insert was then fully assembled using the main screw but leaving the maximum distance between the two plugs with one plug remaining outside of the tube to allow sand to be added. A mass of sand was measured and deposited into the tube on top of the inserted plug. The second plug as then

inserted into the tube. The entire insert with un-packed sand between the plugs was pushed into the fluid inside the tube. Additional fluid was added on top of the plug to ensure it was entirely covered with fluid. Trapped air was removed by shaking the tube from side to side, allowing bubbles to escape. The screw was then tightened to compact the bed. The measured porosity of the bed was in the range 0.4 to 0.45 prior to compaction. The compacted porosity is somewhat lower. The pressure required to push the fluid through the bed was determined by subtracting the pressure drop through the empty tube from the pressure drop through the bed at the same flux. The range of permeability values obtained is shown in Figure 4-12. The relationship between permeability and pore velocity suggests that the medium changes structure in response to the flow rate. This can be thought of as channeling. Vibration appears to reduce channeling. The permeability values and trends are repeatable and fall into the expected range for sand packs [42–45].

Pressure waves are transmitted from the bellows through the packed bed and to the pressure transducer at the opposite end of the tube. The transmitted time domain pressure data were transposed into period domain data using an algorithm described in Chapter three. The maximum difference between points on the average curve defines the peak-to-peak amplitude of the transmitted pressure wave. The transmitted pressure waves, with ~12 kPa amplitudes, shown in Figure 4-13 are from the same test and time section of data as the permeability measurements at the lowest flow rate and 2 Vpp in Figure 4-12. The variability around the average appears to increase with the number of cycles. The origin of this behavior and its evaluation are subjects for future work. The magnitude of this cycle-to-cycle variation is noted in the results section for all experiments.
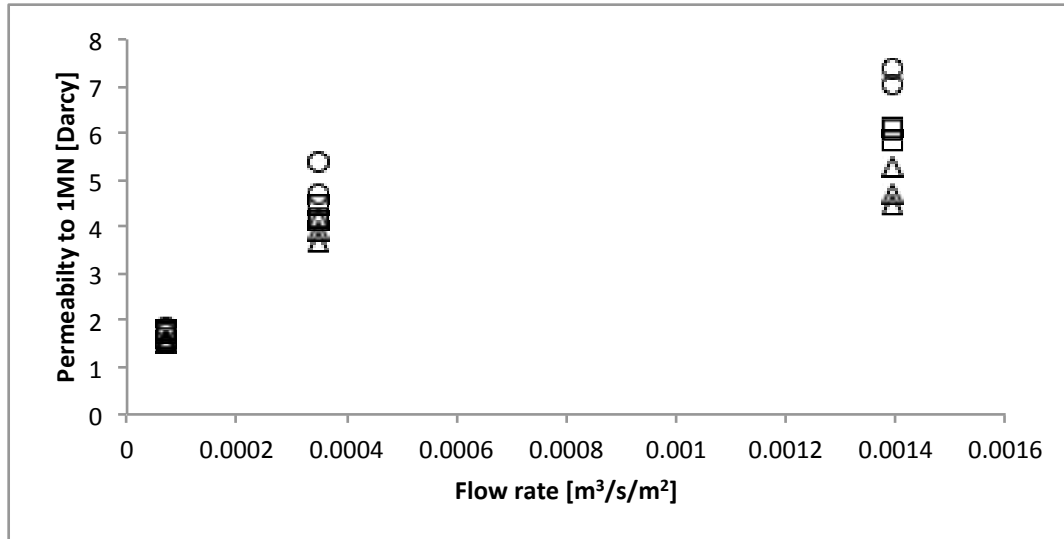
Figure 4-12: Permeability of sand pack to 1MN as a function of flux. No vibration (O), 500 Hz at 1 Vpp (□) and 500 Hz at 2 Vpp (△) are parameters.
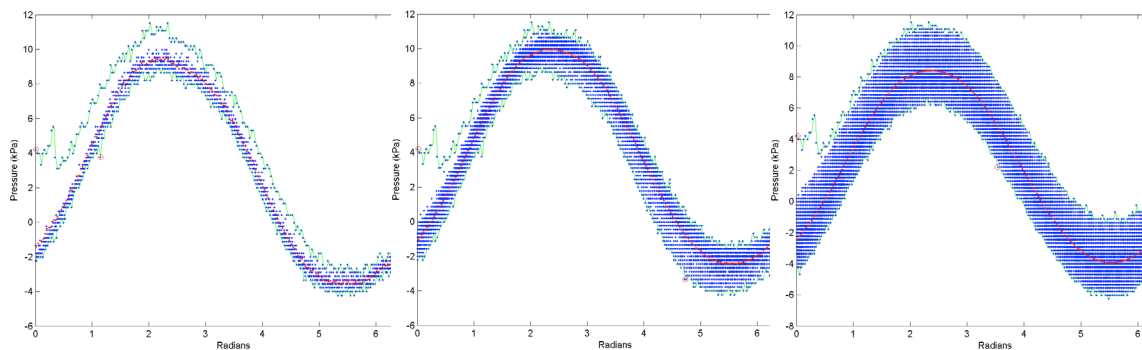
Figure 4-13: Sand pack saturated with 1MN with a flow rate of 20 mL/min exposed to 500 Hz with 2 Vpp: a) First 10 cycles, b) first 100 cycles, c) 5 minutes of exposure.

Results and Discussion

Observations of Bubble–Fluid–Media Interactions

Observations of interactions among sand grain motion, miscible interface motion, gravity drainage, and bubble dynamics, in the presence of forced vibration, are presented and

discussed in this section. Numerous forced vibration studies were completed with and without attributes for the phenomena described above. The presence of bubbles caused much larger observable changes than any of the other phenomena and therefore these were the focus of detailed study. Four forced vibration case studies with bubbles are discussed here in detail. In each one, it was possible to observe impacts with and without bubbles present because bubbles were either added to the unconsolidated sand bed or formed within the unconsolidated sand bed after some time. The experimental matrix is illustrated in Figure 4-14. Impacts of bubbles far from resonance (case 1 at 50 Hz) and approaching resonance (case 2 at 500 Hz and case 3 at 50 Hz), and bubble generation and growth to resonance (case 4 at 500 Hz) were investigated. Impacts of bubbles on single and two-phase liquids were considered. These experiments were set up in a similar fashion to obtain comparable starting conditions. To initiate these experiments water, less dense than 1MN and more dense than pentane and immiscible with both, was layered between the two miscible hydrocarbons. The tube was then re-oriented to create an interface between 1MN and pentane to permit them to mix directly. Bubbles were then generated or inserted in a desired location as described on a case-by-case basis below. Bubbles of pentane vapour and air did not wet the sand grains in either water or 1MN + pentane sand packs as expected from available contact angle data for water or hydrocarbons with air on quartz surfaces [46]. Experimental observations for all four cases are reported in Figures 4-15 – 4-18, respectively, as a series of video and still images. For each case, there is a period of time before bubbles are introduced during which vibration induced grain motion is clearly evident, as anticipated from Figure 4-5 and noted in Chapter three. Local particle accelerations exceeding 1 g are readily induced and observed. Some sand grains stop moving once they possess a stable orientation, while other grains continue to vibrate until this motion is dominated by motion caused by bubbles. Drop motion and drop shape change (Figure 4-3) were not observed, and the spatial resolution of the optical technique did not permit observation of fluid velocity profiles (Figure 4-2). However, they are expected to be "flat" as opposed to "parabolic" in shape over the range of conditions explored.
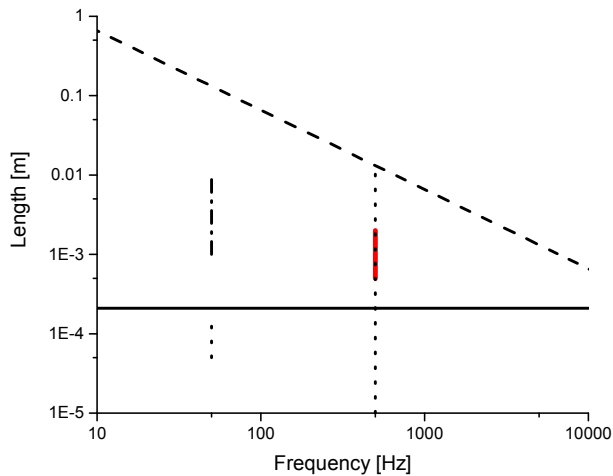
Figure 4-14: Illustration of the experiment matrix. The horizontal solid line depicts the mean size of the sand grains, 210 μm. The angled dashed line is the resonant frequency of air bubbles in water (Equation 4-5) (−−−). Case 1: bubbles far from resonance (••• at 50 Hz). Case 2: near resonant bubbles (| at 500 Hz). Case 3: near resonant bubbles, (−• at 50 Hz). Case 4: bubble generation and growth to resonance (- - - at 500 Hz).

Bubbles far from Resonance - Vibration Facilitates Density Based Fluid Segregation

Pore scale bubbles may be formed when a vessel is depressurized, when reservoir pressure is reduced, when a fluid including volatile constituents is heated, or as a result of chemical reaction. Figure 4-15 shows pore scale pentane vapour bubbles formed in the sand bed by reducing the pressure to the vapour pressure of pentane. In the absence of vibration these bubbles are at equilibrium and the capillary forces balance the gravitational forces. Vibration at 50 Hz with peak-to-peak amplitudes of ∼ 40kPa (Case 1, with period to period variations not exceeding 20 kPa) transmitted from below the bed causes pentane bubbles to oscillate in size and shape, in phase with the vibration. Oscillation combined with buoyancy overcomes the capillary forces and the bubbles rise within the bed allowing water to flow back into the bed under gravity driven flow. Flow only occurs because the bubbles are liberated by vibration. This example illustrates how vibration causes bubbles to oscillate and move allowing density based fluid segregation of surrounding fluids to

occur in an open system under conditions where flow and segregation would not otherwise be expected to occur.

Near Resonant Bubbles— Induced Mixing of Unconsolidated Media

Figures 4-16 and 4-17 show large bubbles that are close to their resonant frequencies (Cases 2 and 3 respectively). For these cases, the bubbles were generated below the bed by allowing the pentane to flash (Case 2) or by injecting air (Case 3). These bubbles remain static in the absence of vibration. However, mixing of the particles in the bed is readily achieved at 500 Hz (Case 2, ~ 140 kPa peak-to-peak where the period-to-period variations do not exceed 40 kPa) and at 50 Hz (Case 3, ~40 kPa peak-to-peak where the period to period variations do not exceed 20 kPa). In both cases the bubbles are pushed away from the vibration source and cause the bed to rotate. Clearly, the nature of the motion, if not the scale, is dictated by the equipment geometry. The video attached to Figure 4-16 tracks the intensity of the blue image spread onto an RGB scale so that the local variation of hydrocarbon concentration, with time, becomes visible. Red corresponds to high concentration, green to intermediate and blue to low concentration. Figure 4-17 shows water-wet sand containing 1MN that is exposed to vibration at 50 Hz with air bubbles approaching resonance. The sound source is below the bed. The water-wet sand sticks together due to surface energy reduction as the bubbles are pushed through the bed by the vibration. These two examples show that near resonant bubbles are large relative to the pore scale. They move through the bed, when subject to vibration, and cause the bed to mix over a broad range of applied frequencies.

The trade off between bubble size and sound wave attenuation, a topic addressed elsewhere [2, 28, 47] is critical to understanding the implications and potential applications of near resonant bubbles. Resonant bubbles absorb and dissipate vibrational energy. This reduces the distance a sound wave can travel in a porous medium.

Bubble Generation and Growth to Resonance—Disruption of Bed

If bubbles are not present initially, they can be formed by vibration if during part of the period of oscillation the pressure drops below the liquid bubble pressure. Figure 4-18 comprises a time lapsed video with a 500 Hz vibration (Case 4, ~25 kPa peak-to-peak amplitude and period-to-period variations less than 5 kPa) applied on the left hand side of a 1MN saturated packed sand bed while more volatile pentane is added on the right. It is important to remember that the pressure amplitude measured is after transmission through the bed and therefore the amplitude is higher than the measured value as the source is approached. In this experiment, it is only when the pentane approaches the source (left side of the image) that the large amplitude pressure changes needed to form a bubble arise. As the bubble grows it approaches resonance, perhaps through rectified diffusion, its oscillation amplitude increases and resonant behavior develops. The bubble is pushed rapidly through the bed, generating sand grain motion, displacement of 1MN, and compaction of the bed itself. This observation shows that in a system that includes a volatile fluid or one where a volatile liquid is introduced, exposure to vibration can cause a bubble of resonant size to develop over time leading to significant impacts on local physical properties of a bed (porosity, permeability) and hydrodynamic behavior (fluid and particle movement).

These preliminary observations show that bubble related vibration effects have the greatest impact on flow outcomes, and particle movement for single and two-phase liquids in unconsolidated media. Other effects, noted in Figure 4-1, are minor by contrast if bubbles are present. This suggests that when considering global impacts of vibration in porous media the first matter is to determine if bubbles are present or are likely to be generated over time. If bubbles are present then their behaviors and impacts dominate. Thus, the summative induced flow/particle movement map, Figure 4-6, does not translate readily into a simple response map. It possesses a minimum of two principal prototypes: one dictated by bubble behaviors that liberate dispersed fluid phases, induce fluid and particle movement and alter medium permeability irrespective of the details of the forced vibration conditions applied; and another, dictated in the absence of bubbles, by subtler interactions of the body motions and interfacial behaviors induced by the vibration under

106

specified conditions. Steady state and episodic vibration variants, and temporal transitions from one principal prototype to the other must also be considered for dynamic processes. Further, variants impacted by wettability (particle–bubble, particle–dispersed liquid) and other process variables can also be envisaged. The range of possible system responses to vibration is vast and this helps explain, for example, the variability of outcomes observed with reservoirs subject to stimulation noted in the introduction. Few variables are monitored or controlled in field experiments.
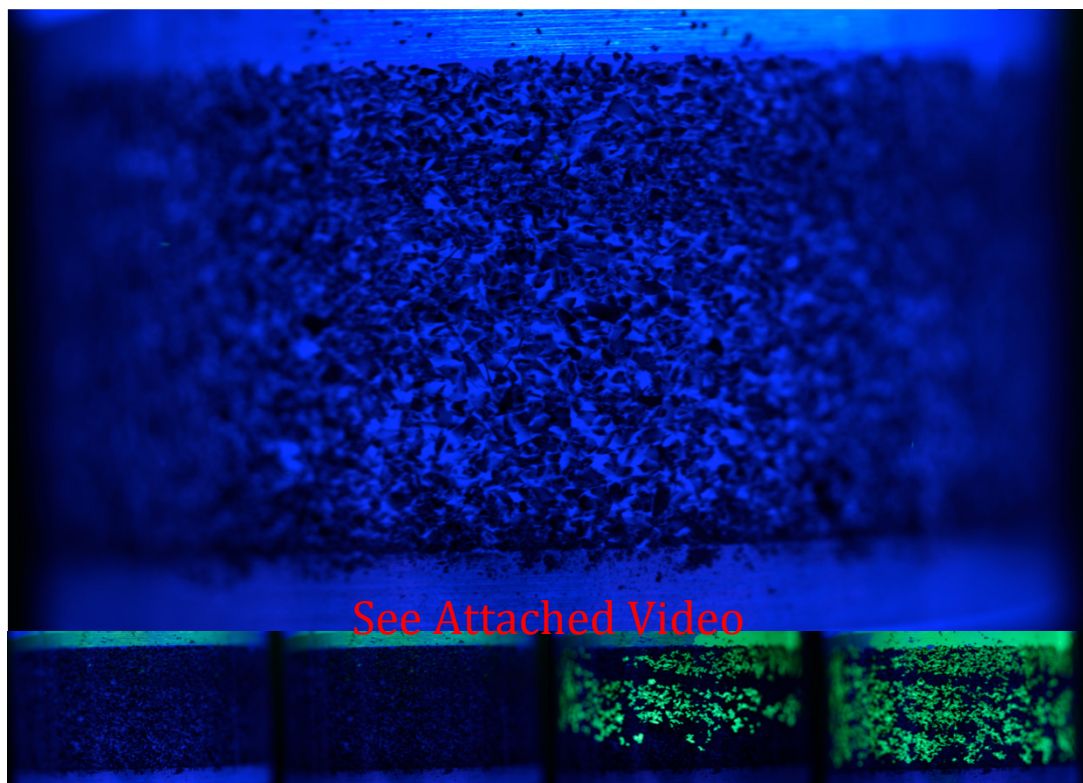
Figure 4-15: Video and video stills for Case 1 (50 Hz with a peak-to-peak amplitude of ~40 kPa) showing pentane vapour bubbles being liberated from the sand bed due to vibration permitting water (green) to flow back into the unconsolidated sand bed. (Multimedia view) [URL: https://drive.google.com/file/d/0ByeSAoO1fKJDVmJVbFI1aWt5ZkE/view?usp=sharing]
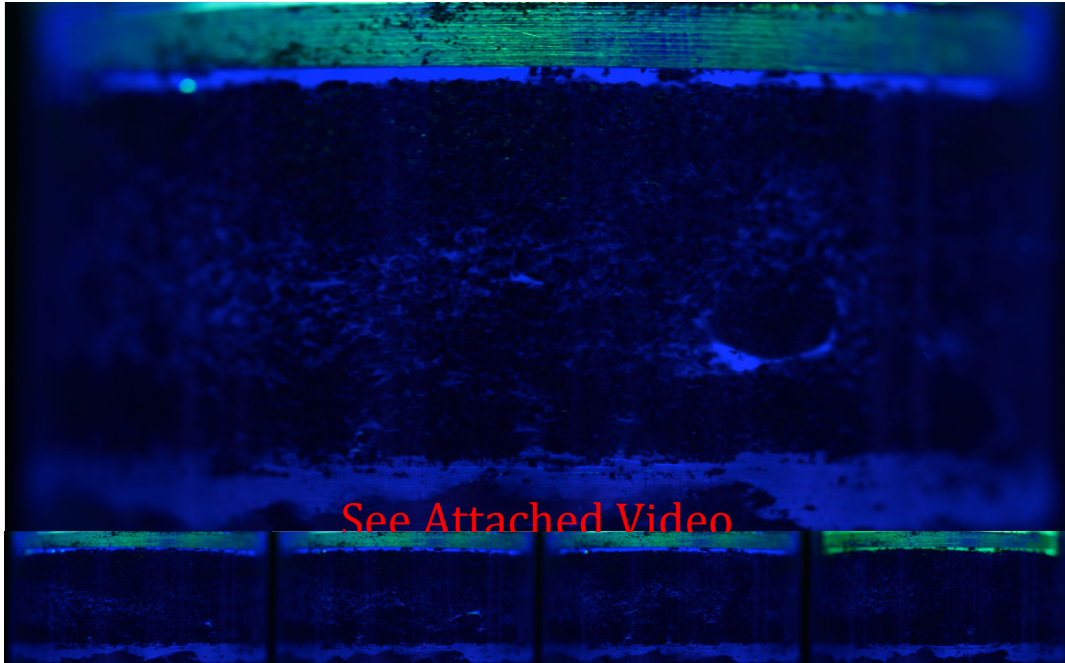
Figure 4-16: Video stills of Case 2 showing oscillating pentane vapour bubbles moving through a sand bed saturated with 1MN + pentane mixture due to vibrations at 500 Hz with a peak-to-peak amplitude of ~140 kPa generated below the bed. Bubble motion causes the sand grains to mix. (Multimedia view) [URL: https://drive.google.com/file/d/0ByeSAoO1fKJDaUs5MUFMdEQydUE/view?usp=sharing]
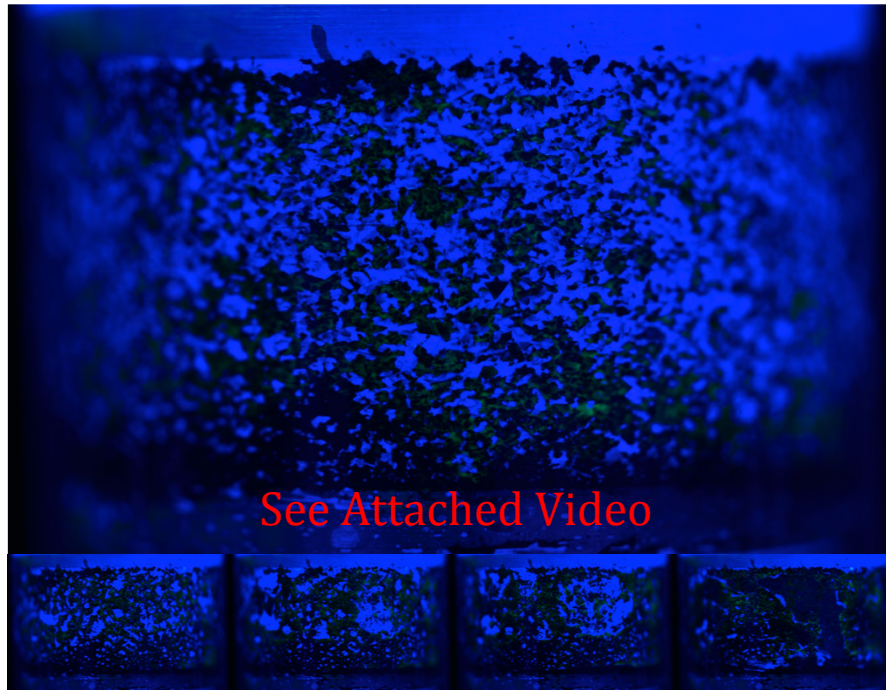
Figure 4-17: Video stills of Case 3 showing water wet media (dark green) exposed to 50 Hz vibration with a peak-to-peak transmitted pressure wave amplitude of ~40 kPa. Air bubbles larger than the pore scale below the bed are forced up through the bed by vibration (the source is below the bed). Water wet media rich zones align over time to reduce interfacial area. (Multimedia view) [URL: https://drive.google.com/file/d/0ByeSAoO1fKJDeHkzd1JHLVhHbkU/view?usp=sharing]

Figure 4-18: Video and still images for case 4 showing the development of near resonant pentane vapour bubbles over time in a bed of sand saturated with 1MN exposed to 500 Hz (~25 kPa peak-to-peak amplitude with a maximum period to period variability of ~5 kPa). Pentane reduces the fluorescence along the top of the tube and vapourizes as the vibration source (left side of the images) is approached. The near resonant bubble then oscillates through and disrupts the bed. (Multimedia view) [URL: https://drive.google.com/file/d/0ByeSAoO1fKJDd2tKbjFWWUlGTTg/view?usp=sharing]

Potential Industrial and Environmental Applications of, and Concerns Related to Vibration in, Unconsolidated Porous Media

The conceptual understanding developed through cases 1-4 provides a basis for assessing outcomes in open or enclosed industrial and natural environments and for speculating on how to manipulate interactions among bubbles, liquids and consolidated or unconsolidated media to achieve specific process outcomes using vibration. For example:

(1) Bubble induced media or liquid movement could be used to break drainage films and permit stranded liquids to flow in oil or natural gas reservoirs—an effect illustrated in Figure 4-17. Bubbles could be injected/formed in situ and pushed from one section of a porous medium to another while entraining desired fluids—an effect illustrated in Figures 4-15 or 4-16. In the proposed steam assisted gravity drainage (SAGD) + solvent processes for heavy oil production [43, 44, 48] this effect, if exploited, could improve well pair connectivity and solvent delivery to undisturbed heavy oil in the reservoir.

(2) Dispersed liquids or solids that attach to bubble surfaces can be transported within a porous medium using vibration, as exemplified for water transport by bubbles in Figure 4-17. Such materials could initiate phase separation, aid in a reaction or provide chemicals for microscopic organism control. Nanoparticles could also be attached to bubbles and dispersed in a porous medium for use as active heating/cooling elements, remote sensing of specific chemicals or for some reactive/catalytic process. Bubbles could be used to remove surface-active contaminants from a porous medium such as contaminants in soils, aquifers or a product in a mining operation.

(3) Vibration improves gas–liquid mass transfer in porous media through enhancements to "snap-off"—an effect similar to vibration enhanced gas–liquid mass transfer in liquid–gas contactors subject to vibration [19, 49, 50]. A vibration source would push bubbles through the particle bed, as shown in Figures 4-16 and 4-17—reducing boundary layer thickness and exposing the bubbles to larger composition differentials. Potential applications of this effect range from enhancing carbon dioxide sequestration rates to reactant gas delivery or product gas removal rates in industrial processes within porous media.

(4) The location of bubbles within a medium can be controlled through generation of standing waves in closed systems, such as a vessel, or open systems with geological boundaries. Standing waves produced at a system resonant frequency push bubbles to nodes and antinodes [31]. The impacts of bubble interaction with surrounding media and fluids can then be localized at desired planes within a porous medium.

(5) Dissonance in performance among laboratory, pilot, and field or industrial scale processes may be traced to differential impacts of vibration, or the absence of vibration, at the different sites and process scales. Significant effort is typically expended during the design of large-scale industrial facilities to minimize the potential damage to equipment and structures caused by vibration. Such analyses are typically not performed for laboratory or pilot scale facilities. As seen in Figures 4-15 – 4-18, bubbles produce qualitatively and quantitatively different outcomes from bubble free cases and introduce a range of additional variables. In vibrating systems possessing different combinations of frequency, amplitude and gas content, the impacts on flow, mass transfer, etc. may be significant or insignificant.

(6) Purposeful introduction of vibrations would require significant prior engineering analysis to ensure that the vibrations do not cause undesirable over all outcomes. Vibration may be beneficial in one part of a process, but introduce detrimental effects elsewhere. Vibration isolation may be key to successful implementation. Use of the scaling analysis provides a starting point for investigations into the impacts of specific vibrations.

(7) Vibration induced unconsolidated media motion alters bed permeability, Figure 4-12, and can cause preferential or detrimental media abrasion, Figure 4-18, such as reduction in coke particle size and catalyst particle abrasion respectively. These impacts, illustrated in Figure 4-12, become important if bubbles are not present.

Conclusions

The impacts of vibration on bubble–fluid–unconsolidated porous media systems were reviewed. A scaling procedure including the Womersly number, viscous diffusion time, viscous and inertial response time, bubble resonant frequency, and a particle force balance was presented and then applied to the mechanisms (velocity profile modification, drop

deformation, bubble compression and motion and unconsolidated porous media motion) known to arise in porous media. All of the mechanisms were identified as active for overlapping frequency and length scale domains, based on model single and two-phase liquids, and low-density gas bubbles possessing broadly applicable properties. For single-phase liquids, flat as opposed to parabolic velocity profiles are expected in micro porous media at frequencies exceeding $\sim$ 10 Hz. The unconsolidated porous medium is expected to become mobile at frequencies greater than $\sim$ 50 Hz. Dispersed micro-scale liquid drops are expected to deform from near 0 Hz to more than 1000 Hz. Size dependent bubble movement is expected at all frequencies. Interactions among the mechanisms were not resolved by analysis, and experiments were conducted at 50 Hz and 500Hz to observe which one or ones dominate. Drop deformation and velocity profiles were not observed experimentally. However, particle movement and local particle bed compaction/channel formation were readily observed at both 50 Hz and 500 Hz. Bubbles whether present or generated in situ disrupted behaviors otherwise observed. They compacted the sand bed, caused unconsolidated porous media motion, displaced the non-wetting liquid phase (if present), and caused particle mixing among other effects. The observed dominance of the combination of bubbles plus vibration on the behavior of bubble–fluid–porous media systems presents many areas of application for future study, from the impact of episodic seismic activity on aquifer properties, to vibration enhanced hydrocarbon production and carbon dioxide sequestration technology development, to the resolution of dissonance in performance between lab, pilot and industrial scale processes where vibrations and gas content is not carefully controlled.

Acknowledgements

References

[1]   *Guidelines for the Avoidance of Vibration Induced Fatigue Failure in Process Pipework*. Energy Institute (Great Britain), 2008.

[2]   A. B. Wood, *A Textbook of Sound*. London: G. Bell and Sons Ltd., 1930.

[3]   R. H. Liu, J. Yang, M. Z. Pindera, M. Athavale, and P. Grodzinski, "Bubble-induced Acoustic Micromixing.," *Lab Chip*, vol. 2, pp. 151–157, Aug. 2002.

[4]   B.-N. Kim, S. W. Yoon, B. K. Choi, and S.-K. Jung, "Gas Void Fraction Estimation in Gas-Bubble-Contained Sands with Difference Frequency Waves," *Jpn. J. Appl. Phys.*, vol. 51, Jul. 2012.

[5]   B. Y. J. F. Hale, D. A. Mcdonald, and J. R. Womersley, "Velocity Profiles of Oscillating Arterial Flow, with some Calculations of Viscous Drag and the Reynolds Number," *J. Physiol. - London*, no. 23, pp. 629–640, 1955.

[6]   J. R. Womersley, "Method for the Calculation of Velocity, Rate of Flow and Viscous Drag in Arteries when the Pressure Gradient is Known," *J. Physiol.*, vol. 127, pp. 553–563, 1955.

[7]   D. R. Graham and J. J. L. Higdon, "Oscillatory Flow of Droplets in Capillary Tubes. Part 1. Straight Tubes," *J. Fluid Mech.*, vol. 425, pp. 31–53, Dec. 2000.

[8]   I. A. Beresnev and P. A. Johnson, "Elastic-wave Stimulation of Oil Production: A Review of Methods and Results," *Geophysics*, vol. 59, no. 6, pp. 1000–1017, Jun. 1994.

[9]   V. N. Nikolaevskii, "Rock Vibration and Finite Oil Recovery," *Izvestuya Ross.*, no. 5, pp. 689–696, 1993.

[10]   T. Hamida and T. Babadagli, "Immiscible Displacement of Oil by Water in Consolidated Porous Media due to Capillary Imbibition under Ultrasonic Waves.," *J. Acoust. Soc. Am.*, vol. 122, no. 3, p. 1539, Sep. 2007.

[11]   K. Naderi and T. Babadagli, "Pore-scale Investigation of Immiscible Displacement Process in Porous Media under High-frequency Sound Waves," *J. Fluid Mech.*, vol. 680, pp. 336–360, May 2011.

[12]   I. Beresnev, W. Gaul, and R. D. Vigil, "Direct Pore-level Observation of Permeability Increase in Two-phase Flow by Shaking," *Geophys. Res. Lett.*, vol. 38, no. 20, Oct. 2011.

[13]   W. Li, R. D. Vigil, I. A. Beresnev, P. Iassonov, and R. Ewing, "Vibration-induced Mobilization of Trapped Oil Ganglia in Porous Media: Experimental Validation of a Capillary-physics Mechanism," *J. Colloid Interface Sci.*, vol. 289, no. 1, pp. 193–199, Sep. 2005.

[14]   P. P. Iassonov and I. A. Beresnev, "Mobilization of Entrapped Organic Fluids by Elastic Waves and Vibrations," no. December, pp. 465–473, 2008.

[15]   C. V. Chrysikopoulos and E. T. Vogler, "Acoustically Enhanced Ganglia Dissolution and Mobilization in a Monolayer of Glass Beads," *Transp. Porous Media*, vol. 64, no. 1, pp. 103–121, Jul. 2006.

[16]   R. J. Glass and L. Yarrington, "Mechanistic Modeling of Fingering, Nonmonotonicity, Fragmentation, and Pulsation within Gravity/Buoyant Destabilized Two-phase/Unsaturated Flow," *Water Resour. Res.*, vol. 39, no. 3, p. 1058, 2003.

[17]   I. A. Beresnev and W. Deng, "Theory of Breakup of Core Fluids Surrounded by a Wetting Annulus in Sinusoidally Constricted Capillary Channels," *Phys. Fluids*, vol. 22, no. 2010, p. 012105, 2010.

[18]   W. Deng and M. B. Cardenas, "Dynamics and Dislodgment from Pore Constrictions of a Trapped Nonwetting Droplet Stimulated by Seismic Waves," *Water Resour. Res.*, vol. 49, no. October 2012, pp. 4206–4218, 2013.

[19]   W. Deng, M. B. Cardenas, and P. C. Bennett, "Extended Roof Snap-off for a Continuous Nonwetting Fluid and an Example Case for Supercritical CO2," *Adv. Water Resour.*, vol. 64, pp. 34–46, 2014.

[20]   K. E. Lapo, L. M. Hinkelman, M. S. Raleigh, and J. D. Lundquist, "Influence of Dynamic Factors on Nonwetting Fluid Snap-off in Pores," *Water Resour. Res.*, vol. 51, pp. 1–8, 2015.

[21]   N. R. Morrow, "Physics and Thermodynamics of Capillary Action in Porous Media," *Ind. Eng. Chem.*, vol. 62, pp. 32–56, 1970.

[22]   I. A. Beresnev and P. A. Johnson, "Elastic-wave Stimulation of Oil Production : A Review of Methods and Results," *Geophysics*, vol. 59, no. 6, pp. 1000–1017, 1994.

[23]   H. Sheikha and M. Pooladi-Darvish, "Micro Bubbles in Solution–Gas Drive in Heavy Oil: Their Existence and Importance," *Transp. Porous Media*, vol. 93, no. 3, pp. 495–516, Mar. 2012.

[24]   J. M. Thomas and C. V Chrysikopoulos, "Experimental Investigation of Acoustically Enhanced Colloid Transport in Water-saturated Packed Columns," *J. Colloid Interface Sci.*, vol. 308, no. 1, pp. 200–207, Apr. 2007.

[25]   C. O. Vandu, J. Ellenberger, and R. Krishna, "Hydrodynamics and Mass Transfer in an Upflow Monolith Loop Reactor," *Chem. Eng. Process. Process Intensif.*, vol. 44, pp. 363–374, 2005.

[26]   J. Ellenberger, J. M. van Baten, and R. Krishna, "Intensification of Slurry Bubble Columns by Vibration Excitement," *Catal. Today*, vol. 79–80, no. August, pp. 181–188, 2003.

[27]   W. I. Meldin, L. Masse', and G. L. Zumwalt, "United States Patent 4417621," 1983.

[28]   E. Silberman, "Sound Velocity and Attenuation in Bubbly Mixtures Measured in Standing Wave Tubes," *J. Acoust. Soc. Am.*, vol. 29, no. 8, pp. 925–933, 1957.

[29]   T. J. Mason and J. P. Lorimer, "Applied Sonochemistry The Uses of Power Ultrasound in Chemistry and Processing," 2002.

[30]   I. A. Beresnev, "Theory of Vibratory Mobilization on Nonwetting Fluids Entrapped in Pore Constrictions," *Geophysics*, vol. 71, no. 6, 2006.

[31]   T. G. Leighton, J. Walton, and M. J. W. Pickworth, "Primary Bjerknes Forces," *Eur. J. Phys.*, vol. 11, pp. 47–50, 1990.

[32]   M. A. Biot, "Theory of Propagation of Elastic Waves in a Fluid-Saturated Porous Solid. I. Low-Frequency Range," *J. Acoust. Soc. Am.*, vol. 28, no. 2, 1956.

[33]   F. M. White, *Fluid Mechanics*, 6th ed. New York: McGraw Hill, 2008.

[34]   *DIPPR Project 801 - Full Version*. Design Institute for Physical Property Research/AIChE, 2012.

[35]   P. Bormann, New Manual of Seismological Observatory Practice - NMSOP, no. 2002. 2009, p. 1162.

[36]   "Introduction to nondestructive testing," The American Society for Nondesctructive Testing, 2016. [Online]. Available: https://www.asnt.org/MinorSiteSections/AboutASNT/Intro-to-NDT. [Accessed: 24-May-2016].

[37]   K. Takamura, "Microscopic Structure of Athabasca Oil Sand," *Can. J. Chem. Eng.*, vol. 60, no. 4, pp. 538–545, Aug. 1982.

[38]   C. Zhang, M. Oostrom, T. W. Wietsma, J. W. Grate, and M. G. Warner, "Influence of Viscous and Capillary Forces on Immiscible Fluid Displacement: Pore-Scale Experimental Study in a Water-Wet Micromodel Demonstrating Viscous and Capillary Fingering," *Energy & Fuels*, vol. 25, no. 8, pp. 3493–3505, Aug. 2011.

[39]   C. J. Werth, C. Zhang, M. L. Brusseau, M. Oostrom, and T. Baumann, "A Review of Non-Invasive Imaging Methods and Applications in Contaminant Hydrogeology Research," *J. Contam. Hydrol.*, vol. 113, no. 1–4, pp. 1–24, Apr. 2010.

[40]   C. D. Montemagno and W. G. Gray, "Photoluminescent Volumetric Imaging : A Technique for the Exploration of Multiphase Flow and Transport in Porous Media," *Geophys. Res. Lett.*, vol. 22, pp. 425–428, 1995.

[41] M. Stohr, K. Roth, and B. Jahne, "Measurement of 3D Pore-scale Flow in Index-Matched Porous Media," *Exp. Fluids*, vol. 35, no. 2, pp. 159–166, Aug. 2003.

[42] D. D. Sparlin, "Sand and Gravel - A study of their Permeabilities SPE 4772," in *Offshore Technology Conference*, 1974.

[43] R. M. Butler, G. S. Mcnab, and H. Y. Lo, "Theoretical Studies on the Gravity Drainage of Heavy Oil During In-situ Steam Heating," *Can. J. Chem. Eng.*, vol. 59, no. August, pp. 455–460, 1981.

[44] S. G. Dunn, E. H. Nenniger, and V. S. V. Rajan, "A Study of Bitumen Recovery by Gravity Drainage using Low Temperature Soluble Gas Injection," *Can. J. Chem. Eng.*, vol. 67, pp. 978–991, 1989.

[45] J. E. Nenniger, "How Fast is Solvent Based Gravity Drainage?," in *Canadian International Petroleum Conference*, 2008.

[46] R. Wallach, M. Margolis, and E. R. Graber, "The Role of Contact Angle on Unstable Flow Formation During Infiltration and Drainage in Wettable Porous Media," *Water Resour. Res.*, vol. 49, no. October, pp. 6508–6521, 2013.

[47] S. N. Domenico, "Acoustic Wave Propagation in Air-bubble Curtains in Water- Part I : History and tTheory," *Geophysics*, vol. 47, no. 3, pp. 345–353, 1982.

[48] R. Butler and I. Mokrys, "A New Process (VAPEX) For Recovering Heavy Oils Using Hot Water And Hydrocarbon Vapour," *Journal of Canadian Petroleum Technology*. 1991.

[49] R. Krishna, J. Ellenberger, M. I. Urseanu, and F. J. Keil, "Utilisation of Bubble Resonance Phenomena to Improve Gas-liquid Contact," *Naturwissenschaften*, vol. 87, pp. 455–459, 2000.

[50]   C. O. Vandu, H. Liu, and R. Krishna, "Mass Transfer from Taylor Bubbles Rising in Single Capillaries," *Chem. Eng. Sci.* , vol. 60, pp. 6430–6437, 2005.

Chapter 5: Interface Renewal and Concentration Shock Through Sloughing—Accounting for the Dissonance Between Production Models and Measured Outcomes for Solvent Assisted Bitumen Production Processes

Robert A. Stewart, John M. Shaw.

Introduction

The key to producing heavy oil and bitumen is to reduce their viscosity so that they flow at economic rates. This can be achieved by heating, the basis of the Steam Assisted Gravity Drainage process (SAGD) that is practiced industrially, by diluting the hydrocarbon resource with a low viscosity solvent, or by a combination of the two. All three process prototypes have been subjects of investigation for some time. The first publications on solvent-assisted bitumen production appeared in 1989 [1, 2]. Butler and Mokrys proposed a liquid solvent assisted production system and predicted that rates would be 1/100th that of a steam assisted process but they did not consider all changes in fluid properties arising from solvent addition [1]. In 1989, Dunn and E. Nenniger proposed a condensing solvent process that used the heat of vaporization of the solvent to heat the bitumen as well as to dilute it. They modeled their process using a Steam Assisted Gravity Drainage (SAGD) analogy [2] and suggested the process would be uneconomic due to low molecular diffusion rates. However, their model underestimated experimental production rates by two orders of magnitude. Their process was later named NSolv and patents addressed details such as gas compositions required to prevent the solvent process from being poisoned by non-condensable gases released into the solvent chamber. Later, Butler and Mokrys [3] proposed a production technique that included vaporized solvents and hot water, coined VAPEX, where a vaporized solvent would increase density gradients and

potentially de-asphalt the oil as well during production. Predictive, semi-analytical models continue to suffer from multiple orders of magnitude differences between predicted rates and actual production rates. The dissonance was attributed to mass transfer rates that were higher than expected from molecular diffusion [2, 4–7]. There are now many variants of solvent assisted bitumen production processes with a combination of solvents and steam [8] but a lack of understanding regarding the mechanisms allowing for higher mass transfer rates than anticipated from molecular diffusion limits persists.

The semi-analytical process models for solvent enhanced bitumen production processes follow similar sets of arguments and equations as found in SAGD models. They assume that the produced fluid flows in a continuous film following Darcy's law. The very low rate of solvent diffusion through the flowing film and into the undiluted bitumen is the main reason for low predicted production rates. In 2008, J. Nenniger published a correlation between production outcomes (based on laboratory scale experiments in packed beds and Hele-Shaw cells) and a variable, comprising bitumen viscosity divided by the product of bed permeability and bed void fraction depicted in Figure 5-1 [6]. The mutual diffusion coefficient does not appear, directly, in this log-log relationship. However, as noted by J. Nenniger, mutual diffusion coefficients in liquids can be predicted using liquid viscosity, which does appear in the expression, through relations such as the Wilke-Chang correlation [6, 9]. If the diffusion coefficient is represented by viscosity then other parameters in the correlation may have alternate attributions.   For example, permeability and void fraction, typically associated with Darcy's Law, are often used to define a characteristic length for a porous medium, which in turn can be related to the surface-to-volume ratio of the porous medium.

J. Nenniger suggested that the reason that production rates are higher than expected is due to a 'concentration shock' at the interface between the undiluted bitumen and solvent vapour. High concentration gradients and therefore high rates of mass transfer are maintained at the interface. This is similar to the interfacial renewal mechanism proposed by Das and Butler [4] who suggested that low-viscosity diluted bitumen adjacent to the interface flows away from the interface faster than fluid diffuses into the bitumen. Their

perspective is supported by images from their measurements showing striations—reproduced hear as Figure 5-2 [4]. The interface renewal or concentration shock mechanism is not included in production rate models. Other researchers have advocated that convection occurs at the pore scale and have proposed increasing the mass transfer coefficient quantitative fits for the semi-analytical models [10]. However, such high relative and absolute rates of mass transfer have only been measured at bitumen/solvent interfaces, in the absence of porous media, and in the presence of high shear at the interface [11]. Clearly, the concentration shock or interface renewal mechanism differs fundamentally from convective mass transfer and must be understood and modeled separately.

Interrogating production model assumptions and revisiting fundamental system dynamics through dimensionless group analysis provides qualitative understanding and a basis for constructing process models based on more fundamental principles. For example, in the laboratory experiments, the glass walls of the Hele–Shaw cells are oil-wet and there is no porous medium. In the field, the porous medium is water-wet or partially water-wet; and the presence of a porous medium introduces much larger surface area to volume ratios that introduces additional flow mechanisms. Testing whether convection is possible in a porous media can be addressed using the Archimedes number. The unknown fluid dynamics in the porous media limits the value of commonly used velocity based dimensionless groups such as Reynolds number or Capillary number and associated correlations due to the limiting assumptions required to obtain a velocity. The interface renewal or concentration shock mechanism requires detailed exploration and definition based on other dimensionless groups: such as the Bond, Fourier and Schmidt numbers. In this work, the Archimedes number (Equation 5-1), Bond number (Equation 5-2), Film thickness (Equation 5-3), 1-D mass diffusion (Equation 5-4), Fourier number (Equation 5-5), Mass diffusion time (Equation 5-6), Prandtl number (Equation 5-7) and Schmidt number (Equation 5-8) are briefly reviewed and used to interrogate the basic assumptions in the semi-analytical models for solvent assisted bitumen production. The outcomes from these analyses provide a description of interface renewal that can account for the high production rates observed experimentally.

Brief Review of Forces, Dimensionless Groups and Time Scales Associated with In Situ Solvent/Bitumen Interfaces

During thermal or solvent assisted bitumen production processes there are two interdependent phenomena. The flow of a film, drop or slug of diluted bitumen is related to the rate of thermal or solvent diffusion into the bitumen. The relationship between the two phenomena must be captured correctly to determine how fast bitumen is mobilized. This relationship can be determined using force balances, descriptive dimensionless groups and rate equations for specific phenomena present in the two production environments. For example, forced convection at an interface enhances interfacial mass transfer by up to two orders of magnitude but stringent conditions must be met, imposed by the Archimedes number, for natural convection to occur at length scales arising within porous media. Continual interface renewal, assumed as the cause for increased experimental rates over semi-analytical models [5, 6], presents a fundamentally different bitumen/solvent boundary layer both spatially and temporally and the relevant dimensionless groups are the Bond, Fourier and Schmidt numbers. The Prandlt and Schmidt numbers permit high-level comparisons between thermal and mass transfer in viscous flow. Five phenomena: natural convection, drop formation, film flow, thermal and mass diffusion related to these mechanisms, are illustrated in Figure 5-3. These phenomena are explored individually using relevant dimensionless groups whose values are based on measured fluid properties for bitumen + solvent mixtures, water and the properties of relevant porous media where possible. Before delving into the details of individual mechanisms, the definitions of the dimensionless groups and their applications are rehearsed.

There are three primary forces acting on a drop/slug or film of fluid within a porous medium. Gravity, interfacial tension and viscous forces balance the rate of change of momentum. During gravity drainage the interfacial tension holding a drop or film of fluid in place must be overcome by gravity to cause the fluid to move. Only once the fluid is moving does viscosity come into play. In a porous medium, the pore space is filled with

water-rich and bitumen-rich liquids and water-rich and hydrocarbon-rich gases. The forces related to density differences and the interfacial tensions among these fluids and with the surrounding porous medium must become unbalanced for flow to occur. Dimensionless groups such as the Archimedes and Bond numbers describe the ratio between these forces and can be used to determine conditions where natural convection and interface dynamics dominate.

The Archimedes number (Equation 5-1) is the ratio of the difference in gravitational forces arising from density variation within a fluid (buoyancy) and viscous forces. The Archimedes number is commonly converted into a Grashoff number to determine whether thermal density differences cause natural convection, Figure 5-3a. In determining dominant heat transfer mechanism, natural convection vs. conduction, the Grashoff number is commonly combined with the Prandtl number to obtain the Rayleigh number. Here the Archimedes number is used directly to evaluate whether natural convection occurs in bitumen + solvent mixtures within a porous medium. A mass transfer Rayleigh number, while potentially valuable in simplifying an analysis, reduces clarity that is achieved through keeping phenomena decoupled until fundamentals are understood.

The Bond number (Equation 5-2) is the ratio of gravitational forces (buoyancy) to interfacial forces and is commonly used to characterize interface stability associated with drop formation and drop shape, Figure 5-3b. The Capillary number (Equation 5-2b) is useful in pressure driven flows or displacement type flows and reverts to the Bond number for gravity drainage flows if Darcy's law is used to determine flow velocity.

Film flow, Figure 5-3c, is a well understood and can be described in 2 dimensions using a flat surface, a surface angle, fluid viscosity, fluid density and one additional known—film thickness, fluid velocity or flow rate. Equation 5-3 describes the film thickness based on the average velocity remote from the surface. Film thickness can be compared to pore dimensions. If it is less than the pore radius then the top surface of the film is free flowing and the equation can be used to obtain an estimate of the film thickness. If the film thickness exceeds the pore radius then the equation cannot be applied at the pore scale. If

the film is multiple pore radii thick then the film may be described by something between film flow and Darcy's law. Understanding fluid flow determines the nature of the coupled mass transfer mechanism.

Mutual diffusion of fluids, such as an organic solvent and bitumen, is generally described using Fick's law (1-D Equation 5-4), and bitumen + solvent mixtures are commonly treated as pseudo binaries [9]. The composition dependence of the diffusion coefficient is one concern, as is the applicability of Fick's law at low solvent mass fractions [9, 12]. However, to develop comparative time scales the exact value of the diffusion coefficient is not required. Figure 5-3d shows a 1-D mutual diffusion concentration profile as it changes with time. The dimensionless number that describes a solution to the binary diffusion problem, analogous to thermal conduction, is the Fourier number (Equation 5-5).   This dimensionless time scale permits comparison among diffusion problems with differing length scales and diffusion coefficient values. A characteristic time for the diffusion process can be separated from the Fourier number as Equation 5-6. It describes the rate of a diffusion process. In this work, enhanced mass transfer through concentration shock and interface renewal is built directly from Fick's law. The large spatial gradients of concentration persist, whether the displacement of fluid from the interface is episodic or continuous.

The coupled film flow and mutual diffusion case, Figure 5-3e, is assessed in an effort to gain insights into the mechanisms underlying the solvent assisted bitumen production process concept. By comparing the transfer of mass and heat to momentum transfer through the Prandtl and Schmidt numbers respectively it is also possible to compare thermal and solvent based bitumen production methods.   For example, large Prandtl or Schmidt number values suggest that the viscous boundary layer is larger than the thermal or mass diffusion boundary layers respectively. Thus large Prandtl or Schmidt numbers indicate that momentum transfer is fast relative to heat and mass transfer. For the comparative analysis as a whole, it is useful to think in terms of the relative values of time scales for momentum, heat or mass transfer respectively. This allows the rate-limiting factor in solvent, thermal or combined solvent thermal processes to be identified. Deficiencies in the analogies between thermal and solvent processes embedded in the semi-analytical models

for solvent assisted bitumen production processes are elucidated and a theoretical basis for an interface renewal concept [4], applicable to solvent assisted bitumen production to be developed.

Archimedes number
$$Ar = \frac{gL^3 \rho_l (\rho - \rho_l)}{\mu^2}$$
Equation 5-1

Bond number
$$Bo = \frac{\Delta \rho g L^2}{\sigma}$$
Equation 5-2

Capillary number
$$Ca = \frac{\mu v}{\sigma}$$
Equation 5-2b

Film thickness [14]
$$\delta = \sqrt{\frac{3\mu v}{\rho g cos\theta}}$$
Equation 5-3

1-D concentration driven diffusion
$$\frac{\partial C_a}{\partial t} = D\frac{\partial^2 C_a}{\partial y^2}$$
Equation 5-4

Fourier number [15]
$$Fo = \frac{Dt}{L^2}$$
Equation 5-5

Mass diffusion time
$$\tau_{mass\ diffusion} = \frac{L^2}{D}$$
Equation 5-6

Prandtl number
$$Pr = \frac{c_p \mu}{k}$$
Equation 5-7

Schmidt number
$$Sc = \frac{\mu}{\rho D}$$
Equation 5-8

where δ is the film thickness, μ is the dynamic viscosity of the liquid, v is the average velocity, ρ and ρ_l are the densities of a liquid (drop or film) and the continuous liquid phase respectively, θ is the angle of incline at which the film is flowing, C_a is the concentration of

component *a* in a fluid, *D* is the mass diffusion coefficient, *t* is time from the initiation of diffusion, σ is the interfacial tension between two fluids, C_p is the specific heat of the system, *k* thermal conductivity of the system.
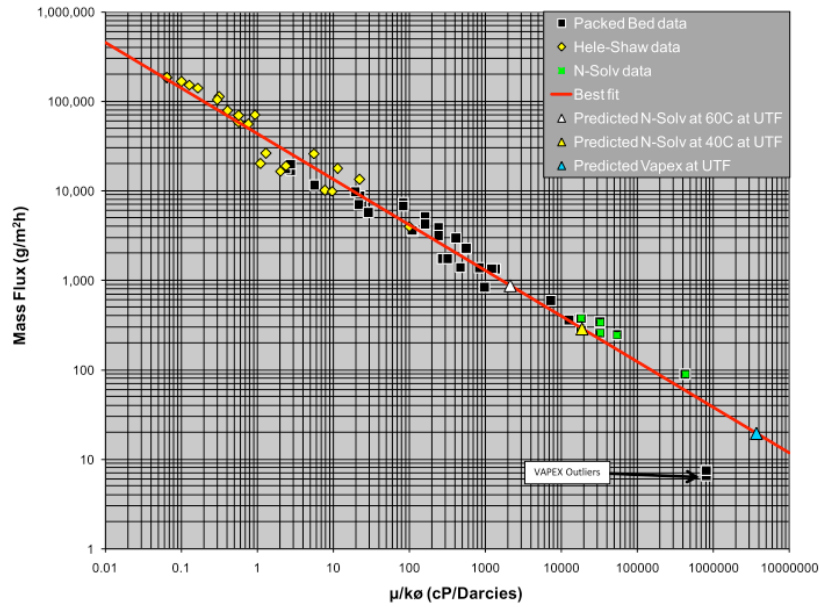
Figure 4: Solvent Based Gravity Drainage Correlation

Figure 5-1:   Reported production rate from experiments plotted against J. Nenniger's scaling parameter where μ is dynamic viscosity in cP, *k* is permeability in Darcy, $\varnothing$ is porosity or void fraction [6].
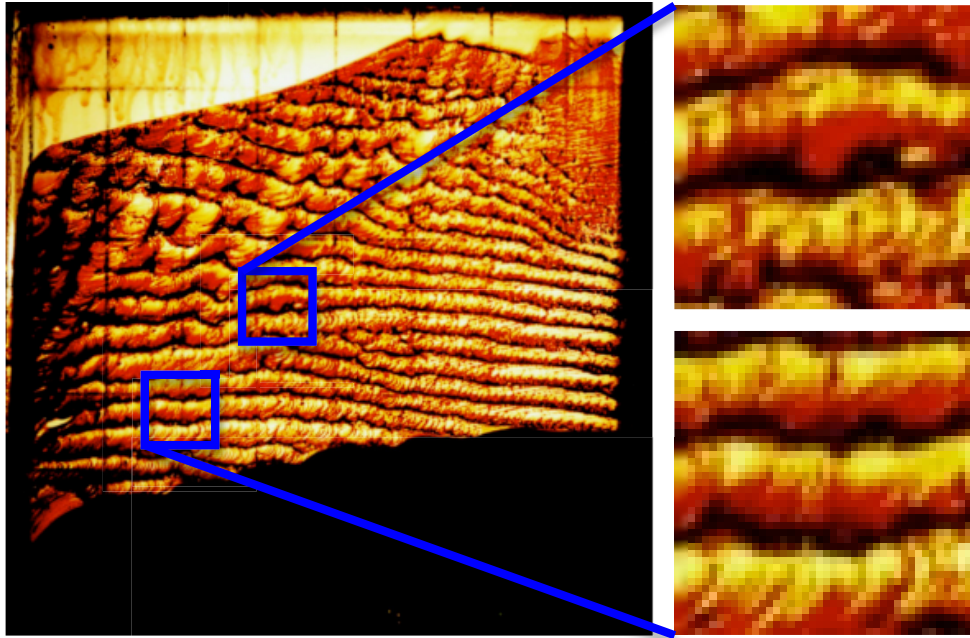
Figure 5-2: Video still from a VAPEX experiment showing repeated interfacial renewal events from a Hele–Shaw cell [4]. The grids are at 1 cm x 1 cm; the thickness of the fluid between the glass plates is 254 micrometre; and the solvent is propane [15]. There is no porous medium and the glass walls are oil wet.

Phenomena	Schematic		Relationships
a) Natural convection mass transfer			Archimedes number Eq. 5-1
b) Drop mobilization (snap off)			Bond number Eq. 5-2
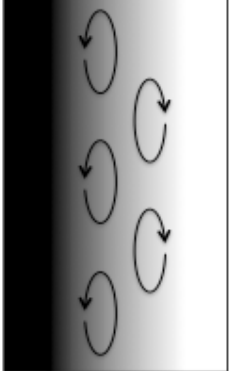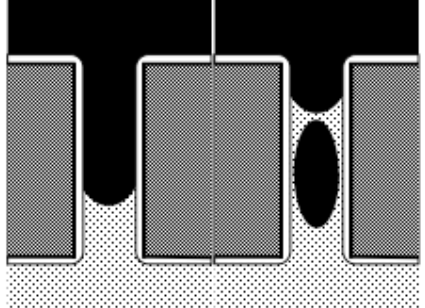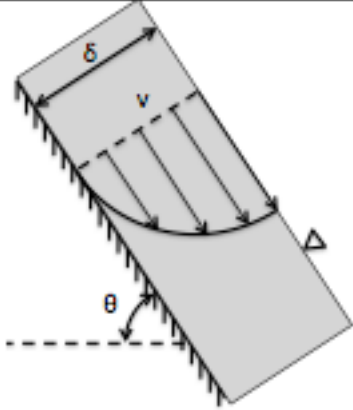
c) Film flow		Film thickness Eq. 5-3
d) 1-D diffusion with time (Thermal or mass)		1-D Fickian diffusion Eq. 5-4 Fourier number Eq. 5-5 Time scale of diffusion Eq. 5-6
e) Boundary layer thickness comparison		Heat transfer Prandtl number Eq. 5-7 Mass transfer Schmidt number Eq. 5-8
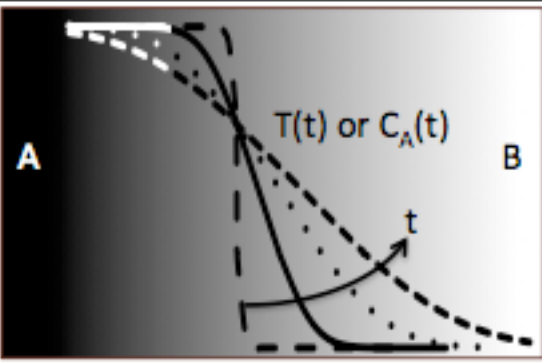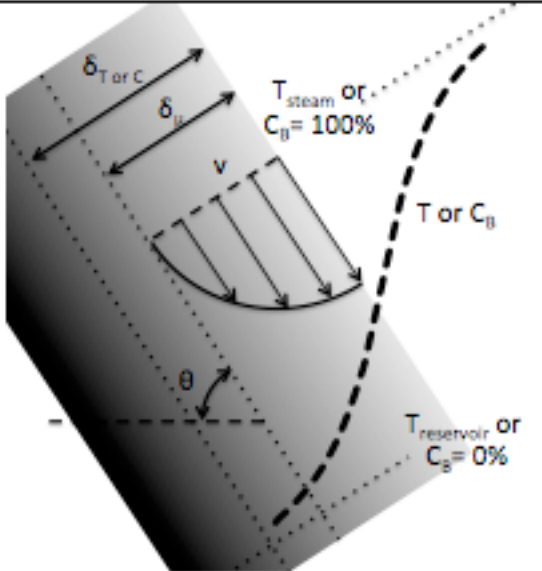
Figure 5-3: Phenomena interrelated in solvent or thermal bitumen production techniques.

Results and Discussion

Application of Dimensionless Group Analysis to Solvent Assisted Gravity Drainage Processes

The application of dimensionless group analysis to solvent assisted gravity drainage production processes for bitumen must be done judiciously because properties of solvent + bitumen mixtures, connate water, and the porous medium vary with time at fixed position and with position at fixed time. Gas bubbles and two liquid phases may also co-exist. With three fluid phases, multiple dimensionless groups may overlap spatially, and temporally as noted in Chapter 4, and phenomena linked to only one phase or one combination of phases may dominate. Further, property data, especially relevant interfacial tension values, are lacking and numerous assumptions must be made. Selecting appropriate length scales for the dimensionless groups is also challenging in the absence of known flow profiles. These complexities have hampered the use of dimensionless groups in this application to date.

To prevent limited data sets including interfacial tension, density and viscosity values [16] from constraining the generality of the discussion, computed values are treated as order of magnitude approximations. Force ratios must be much larger or much smaller than 1 to assure that a specific phenomenon linked to a specific phase dominates. To complete the dimensionless group analysis, a length scale must be assigned to the porous medium. The pore length scale has been related to the permeability as $L=\sqrt{(k/\phi)}$, where k is the permeability and ϕ the porosity [17], but there are other equations for this relationship [18]. The length scale required for convection must also be established or estimated. Thus it is necessary to examine a range of length scales to determine where natural convection and capillary forces dominate buoyancy forces.

Archimedes and Bond Numbers

Figures 5-4 – 5-6 show impacts of bitumen + solvent mixture composition and temperature on the value of the Archimedes number (Equation 5-1). Three cases are considered. Figure 5-4 addresses convection within diluted bitumen using a density difference between different compositions of diluted bitumen. Figure 5-5 addresses convection of pure solvent within diluted bitumen and Figure 5-6 the convection of diluted bitumen within pure solvent. At the length scales of interest, ~100 μm, buoyancy is much less important than viscous forces and consequently, natural convection does not occur irrespective of the assumptions made regarding fluid properties. The largest value of the Archimedes number at this length scale is 10^{-8}. Natural convection does not occur within these fluids in porous media. Viscous forces within the bitumen-rich phase dominate. At larger length scales natural convection may occur at high solvent concentrations as seen experimentally [10] but these large length scales do not arise in heavy oil or bitumen deposits [19]. Something other than convection must occur within solvent assisted bitumen production experiments to account for high rates of mass transfer.

Figures 5-7 and 5-8 show Bond number (Equation 5-2) values over the same length scales. Two cases are considered. The Bond number shown in Figure 5-7 is for the interfacial tension between process water, assumed to be the pore wall wetting fluid, and diluted bitumen. The density difference is between the pure solvent and diluted bitumen. Figure 5-8 shows the Bond number for density differences and interfacial tensions between undiluted bitumen and process water. The largest Bond number value at ~ 100 μm is 10^{-2}. Interfacial forces dominate buoyancy and cannot be neglected. Yang and Gu [20] calculated Bond number values for diluted Lloydminster heavy oil and proposed VAPEX solvents using interfacial tension measurements at 23.9°C [20]. They converted permeability (*k*) and porosity (*ø*) to a length scale using *k=ør²/24*. Their results, reproduced as Figure 5-9, also suggest that interfacial tension dominates buoyancy under the reported conditions.

At the length scale of interest, interfacial forces and viscous forces are more important than buoyancy. Once fluid is mobilized, buoyancy is the presumed driving force for flow (assuming there isn't an interfacial area reduction driving force that could occur in oil-wet

media with solvent) and therefore it cannot be neglected either. As viscous forces only come into play once the fluid is mobilized, interfacial tension must be overcome by buoyancy in order for the fluids to flow. Thus, all three forces play important roles. Interfacial tension is normally excluded and phenomena of importance may therefore be missing from process models. How interfacial tension may impact mass transfer rates, in general, how interfacial tension changes with the addition of solvent, and how solvent assisted bitumen production environments differ from steam assisted bitumen production environments in this respect is addressed in the next section.
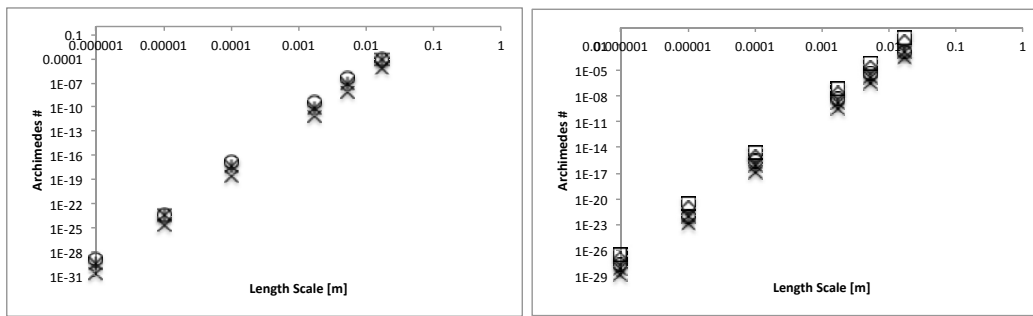
Figure 5-4: Archimedes number versus length scale for convection within diluted bitumen due to density differences between different compositions of diluted bitumen: a) 0 and 5.1 wt. % pentane b) 5.1 and 10.3 wt. % pentane. The density of the surrounding fluid is the average of 5.1 wt. % and 10.3 wt. % pentane. The viscosity used is the average of 5.1 wt. % and 10.3 wt. % pentane. Temperature is a parameter: 343 K ✕, 363 K ✶, 383 K ○, 403 K ◇, 423 K ▢ [16].
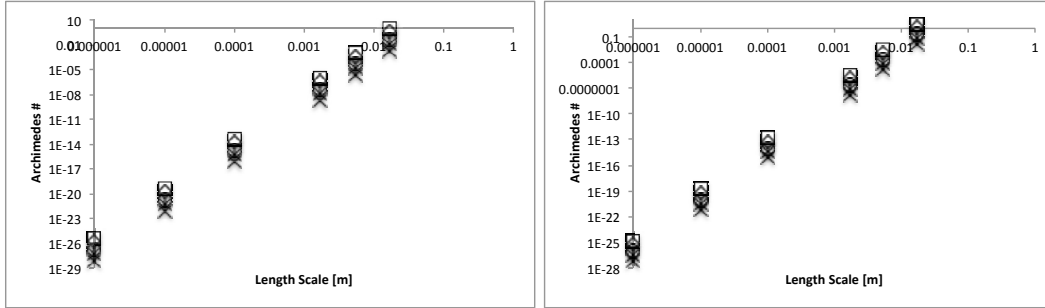
Figure 5-5: Archimedes number versus length scale for convection of solvent within diluted bitumen. Density difference between a) 5.1 wt. % pentane and pure pentane b) 10.3 wt. % pentane and pure pentane. The density of the surrounding fluid is that of bitumen. The viscosity used is that of bitumen. Temperature is a parameter: 343 K ×, 363 K ✳, 383 K ○, 403 K ◇, 423 K □ [16].
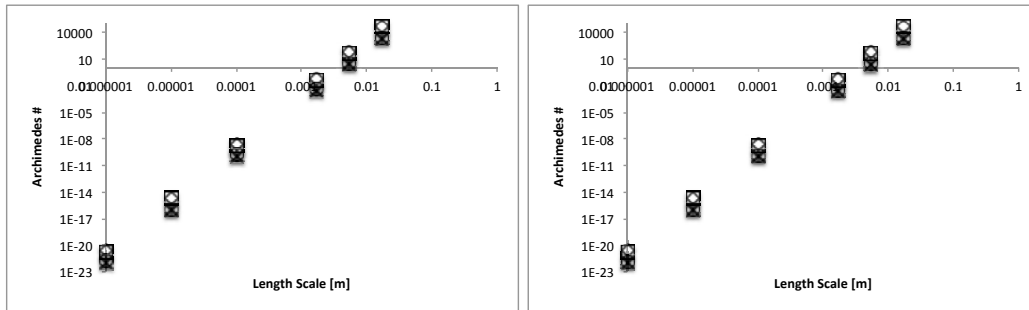
Figure 5-6: Archimedes number versus length scale for convection of bitumen within pentane. Density difference between a) 5.1 wt. % pentane and pure pentane b) 10.3 wt. % pentane and pure pentane [16]. Density of the surrounding fluid is of the solvent (pentane). Viscosity used is of the solvent (pentane)[21]. Temperature is a parameter: 343 K ×, 363 K ✳, 383 K ○, 403 K ◇, 423 K □ [16].
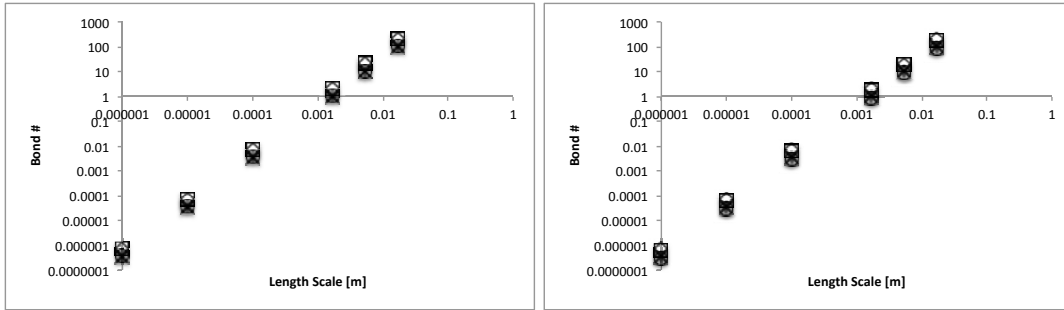
Figure 5-7: Bond number versus length scale. Density difference between a) 5.1 wt. % pentane and pure pentane b) 10.3 wt. % pentane and pure pentane. The interfacial tension used is between diluted bitumen and process water. Temperature is a parameter: 343 K ×, 363 K ✶, 383 K ○, 403 K ◇, 423 K □ [16].
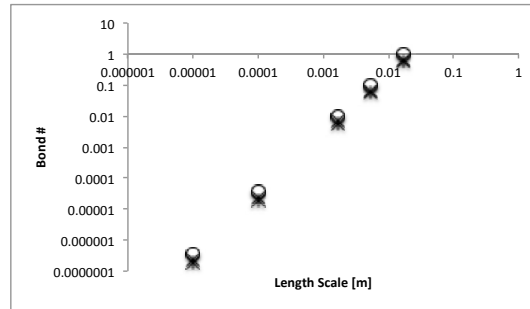
Figure 5-8: Bond number ranges for water and undiluted bitumen. The density difference and interfacial tension values are for undiluted bitumen and process water. Temperatures of 343 K ×, 363 K ✶, 383 K ○ [16].
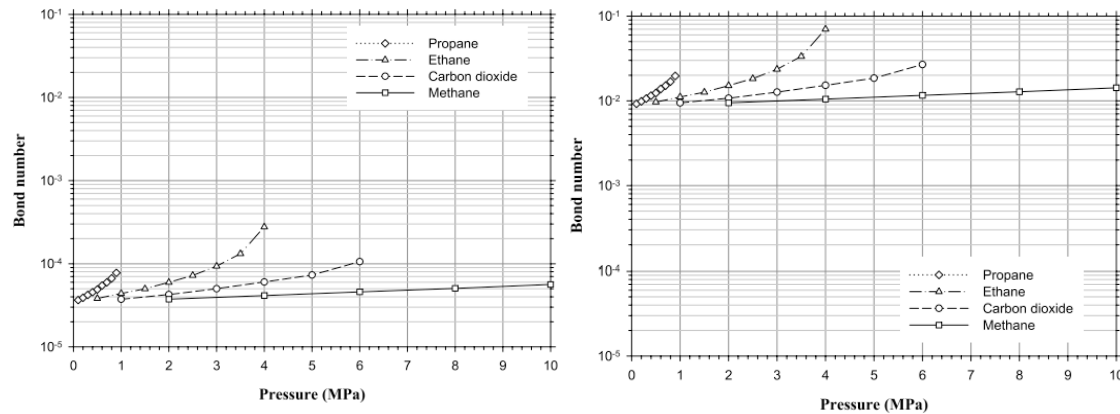
Figure 5-9: Bond number ranges for Lloydminster heavy oil plus propane, ethane, carbon dioxide and methane at 23.9°C. The density difference and interfacial tension values are for undiluted bitumen and the proposed VAPEX solvents: a) for a permeability of 3 μm² and 32% porosity, and b) a permeability of 830 μm² and a porosity of 35%, reproduced from Yang and Gu [20].

Fourier, Prandtl and Schmidt Numbers

Time scales for many phenomena can be calculated by inverting dimensionless groups. For example, the diffusion equation yields a characteristic time that is dependent on the length scale of interest and the diffusion coefficient. During transient diffusion of heat and mass the Fourier number is a dimensionless time. The characteristic time for a given case can be determined from the length scale and the value of the diffusion coefficient. The Fourier number and the associated characteristic time, Equations 5-5 and 5-6 respectively, are dependent on the square of the length scale. For the single file diffusion mechanism, the characteristic time is dependent on the length scale to the power 4. If solvent diffuses through a flowing film whose thickness is determined by viscosity and hence composition to a stagnant and Fickian boundary layer then the semi-analytical models would capture this. However, thin layers of fluid change composition much more quickly than thicker layers irrespective of diffusion mechanism. If the flow were to arise from a different mechanism or if the boundary layer was thinner, then the mass transfer through that thinner layer would occur more rapidly than anticipated from the process models.

The Prandlt and Schmidt numbers, Equations 5-7 and 5-8, are similar in nature but the ratios are for momentum transfer to heat and mass transfer respectively as depicted in Figure 5-3e. Prandtl and Schmidt number values provide relative time scales for thermal and solvent assisted bitumen production processes. For SAGD conditions, Prandlt numbers between 4.25 and 125 are obtained, while for solvent assisted bitumen production processes Schmidt numbers between 50,000 and 500,000 are obtained. These calculations are predicated on a viscosity range of 0.1-0.01 Pa*s—realized for SAGD processes operating between 230 and 260°C, ConocoPhillips Surmont SAGD (Athabasca) [22], Shell Canada Ltd. Orion SAGD (Cold Lake)[23]), bitumen density ($\rho \sim 1000$ kg/m^3), a mutual diffusion coefficient ($D \sim 2.0$ x 10^{-10} m^2/s), a heat capacity (0.85 < C_p < 1.25 kJ/kg/K), porous media thermal conductivity 1 x 10^{-3} < k < 2 x 10^{-3} kW/m/K [9], [24]. The Prandlt number value suggests that during SAGD production heat transfer occurs through the flowing fluid and into the static reservoir as shown in Figure 5-3e. The Schmidt number values for solvent diffusion into bitumen compared to produced fluid viscosities in the range 0.1-0.01 Pa*s, suggest that the time taken for the gravitational potential to begin to move a segment of diluted bitumen is much less than the time taken for the same segment to change composition significantly. A segment of diluted bitumen with a certain composition flows away faster than the segment adjacent to it can reach the same composition. This result supports the interface renewal concept proposed by Das and Butler [4]. Flow at the bitumen–solvent interface is not continuous—invalidating a key assumption in semi-analytical models. The concept of local episodic interface renewal or fluid "snap off" at an interface is not new and is associated with flows where interfacial forces overcome a slow moving fluid [25, 26]. This concept ties back to the Bond number and underscores the importance of interfacial forces in these environments. Gravity over comes viscous and interfacial forces locally. Drops or slugs of fluid flow away from the interface episodically. With high concentration gradients after each event, a mechanism for both interface renewal and concentration shock [2, 5, 6] that can account for the difference between the outcomes from semi-analytical models and experimental measurements can be quantified.

To determine the frequency of interface renewal events the flow mechanism must be revisited. Interfacial tension values between the fluids present in a porous medium determine the type of flow arising in the pore space. Figure 5-10 shows two scenarios valid for water-wet media. Oil-wet media analogues are readily prepared. Both scenarios are driven by interfacial energy minimization. Drop mobilization occurs when $\sigma_{WD} < \sigma_{DP} + \sigma_{WP}$ and film mobilization when $\sigma_{WD} > \sigma_{DP} + \sigma_{WP}$ where σ_{WD} is the interfacial tension between the wetting fluid and the displacing fluid, σ_{DP} is the interfacial tension between the displacing fluid and the produced fluid, σ_{WP} is the interfacial tension between the wetting fluid and the produced fluid. Fluid flow type in solvent + bitumen production processes may be different from flow type in steam assisted production process. Flow type may also vary for different solvents and for different geologies. The flow types for both SAGD and solvent-assisted processes are both unknown because interfacial tension data at reservoir conditions are unavailable. However, both film and drop mobilization are intermittent processes. There must be enough fluid head to overcome the interfacial tension forces before the fluid can flow—discrete quantized volumes flow locally. Interfacial effects are not captured in models based on continuous solvent analogues to the SAGD process. Interfacial tension must be accounted for explicitly in solvent assisted bitumen production experiments to properly capture production outcomes and to translate them to the field scale.

Continual interface renewal increases the mass transfer rate relative to conventional continuous concentration profiles [4, 5]. The time average concentration gradient is larger, leading to faster solvent penetration into the bitumen. Interface renewal, supported by visualizations such as Figure 5-2 from a Hele–Shaw cell, is independent of flow type. The uniformity of the patterns of asphaltene deposition, at $\sim$ 2.5 mm intervals, betray their episodic occurrence. Deposition of asphaltenes only occurs in zones where there are high concentrations of solvent. The pattern of governing physical phenomena is clearly repeated. This occurs in segments because the interfacial tension holding the diluted bitumen in place must be overcome locally before it can flow, even if the viscosity is low enough for flow to occur. The flow of added solvent and diluted bitumen is then co-current (downward) in pores. To overcome interfacial tension locally requires a head of fluid.

These episodic events, similar in principle to why beads of water forming on a vertical glass surface don't flow until they reach a certain size, is referred to as sloughing in the text that follows.

Sloughing – Concentration Dependent Gravity Driven Snap-off

Sloughing, a repeated pattern of diffusion leading to a segment of fluid disengaging from the interface is similar to snap-off observed in low capillary number displacement flows [25]. Snap-off is effectively a redistribution of fluid driven by surface energy minimization, consistent with the concept of Haines jumps or rheons [27]. Gravity driven snap-off has been observed in water-wet media where a hydrocarbon is flowing due to gravity into a permeable material [28]. Figure 5-11 outlines a three-step process in a 2-D channel. The length of interface material that sloughs off is dependent on the viscosity, solvent diffusivity, and interfacial forces.

The depth of material that sloughs off is dependent on local surface area generation, viscosity and buoyancy. As all properties and most significantly viscosity, are dependent on composition, the volume of material that sloughs off is very dependent on local parameters such as pore shape. In a uniform porous medium, Figure 5-2, characteristic lengths are uniform because medium properties are invariant.

An energy balance can be used to determine a limit for the onset of sloughing. The assumptions for this simplified analysis are that the external pressure is constant and the system is isothermal. In N. R. Morrow's analysis [27] equilibrium thermodynamics can be applied whereas in this situation the material is not at mechanical or chemical equilibrium. Changes in chemical potential drive mass transfer in the boundary layer. The time scales for sloughing and mass transfer differ. Sloughing is faster than mass transfer therefore the relevant local compositions can be assumed constant.

For the material to flow either as a film or a drop, new interface must be created. In film flow there is a single interface between the displacing and producing fluid. Figure 5-12

shows how during drop mobilization two interfaces are created and one destroyed. Assuming that the drop is an elongated body such that its ends do not add significant surface area to the total, then the three areas are roughly equal. The limiting criterion for sloughing is when there is enough energy available from the buoyancy term to overcome the interfacial energy generation requirement. The buoyancy term can be determined from the displacement of an equal volume of producing fluid with displacing fluid, shown in Figure 5-12. The potential for this exchange is the height between the center of mass for each finite volume. There is a relationship between the height and a finite volume of fluid (drop or film) but it is dependent on the fluid distribution and pore shape. There is also a relationship between the interfacial area generated and the finite fluid volume— the porous medium surface area to volume ratio. The results for the energy balance are Equation 5-9 for film mobilization and Equation 5-10 for drop mobilization. Viscosity does not play a role in the limit as it is related to fluid motion that can only happen once the sloughing criteria are met. The excess energy available from the buoyancy potential goes into momentum and viscous dissipation. Once the interface has been created the buoyancy potential is balanced by the inertial and viscous dissipation terms alone, causing liquid to move away from the interface faster than new surface is generated. The energy requirement to generate surface area is what causes the sloughing to be slower than the movement of mobilized fluid away from the interface. The limit for sloughing is found by setting the change in energy of the system, the left hand side of Equations 5-9 or 5-10, equal to zero.

The criteria for sloughing introduces a dimensionless number similar to the Bond number, Equations 5-11 and 5-12, but the length scales are specific for sloughing and relate to the surface area to volume ratio for the porous medium. This reliance on a Bond number aligns with gravity driven snap-off in other fluid systems [28]. The distance the material moves to generate the new interface(s), z, is related to the interface depth that solvent has penetrated and directly links to the rate at which the fluid is produced. Therefore, interfacial tension is important but it also does not appear in the work by Nenniger. Thus, it is not the rate-limiting step.

Temperature and pressure may impact the rate of sloughing significantly as the larger the Bond number the more potential energy there is available to be converted into momentum. Operating with specific solvents, surfactants or conditions that impact these numbers would be beneficial for the process. For example, the interfacial tension of a solvent vapour with its liquid approaches zero at the critical point. If the interface between the bitumen and solvent, assumed to be saturated, is maintained at the critical point of the solvent this would significantly reduce the interfacial tension and hasten liquid removal from the interface. The solvent would need to diffuse less between sloughing events and the overall production rate would increase.

This concept can be applied to the Hele–Shaw cell experiments of Das and Butler shown in Figure 5-2 with a surface area to volume ratio described by a rectangular prism with only 2 sides requiring scission from the bulk $\Delta V/\Delta A = L^2W/4LW = L/4$, where L is the length and height of the visible rectangle of fluid and W is the width of the cell. Assuming that the potential $z \sim L$ and a solvent–bitumen interfacial tension of 20 mN*m [20], L where the Bond number is equal to one can be solved for and is found to be ~2.8mm. This suggests that the buoyancy forces on rectangles > 2.8mm can overcome interfacial tension holding them in place allowing them to flow. This value aligns very closely with the observed striation spacing ~ 2.5 mm in Figure 5-2.

Film mobilization energy $$\Delta E = \sigma_{DP}\Delta A + gz(\rho_D - \rho_P)\Delta V$$ **Equation 5-9**

Drop mobilization energy $$\Delta E = (\sigma_{WD} + \sigma_{DP} - \sigma_{WP})\Delta A + gz(\rho_D - \rho_P)\Delta V$$

Equation 5- 10

Bond # film mobilization $$Bo_{film} = \frac{gz(\rho_P - \rho_D)}{\sigma_{DP}}\frac{\Delta V}{\Delta A}$$ **Equation 5-11**

Bond # drop mobilization $$Bo_{drop} = \frac{gz(\rho_P - \rho_D)}{(\sigma_{WD} + \sigma_{DP} - \sigma_{WP})}\frac{\Delta V}{\Delta A}$$ **Equation 5-12**
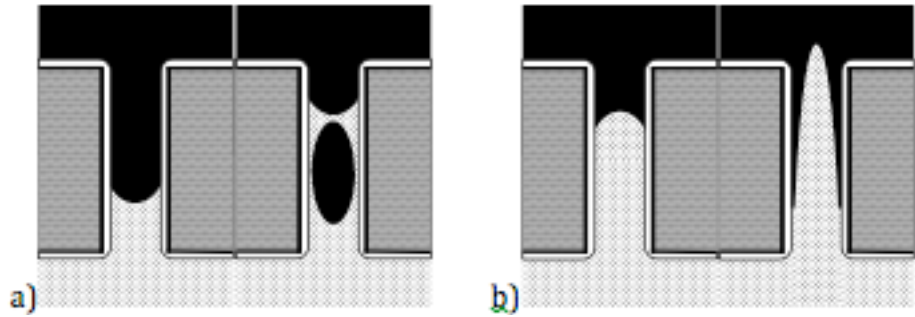
Figure 5-10: Gravity drainage due to a) drop mobilization and b) film mobilization. Wetting fluid (connate water) [white], produced fluid (diluted bitumen) [■], and displacing fluid (solvent) [▒].

1) Diffusion into bulk bitumen

2) Gravity overcomes capillary forces

3) Interface sloughs off revealing fresh interface
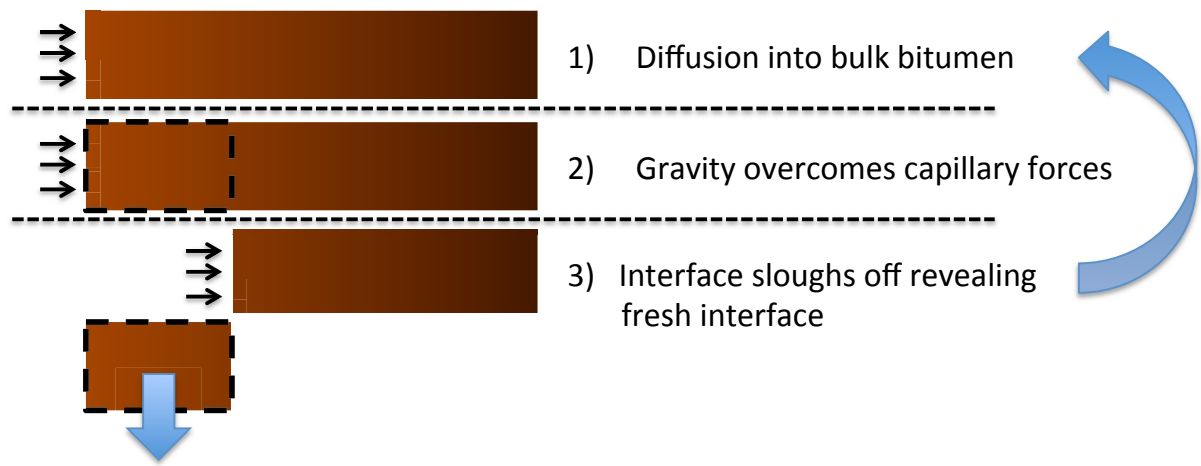
Figure 5-11: Concept of interface sloughing.
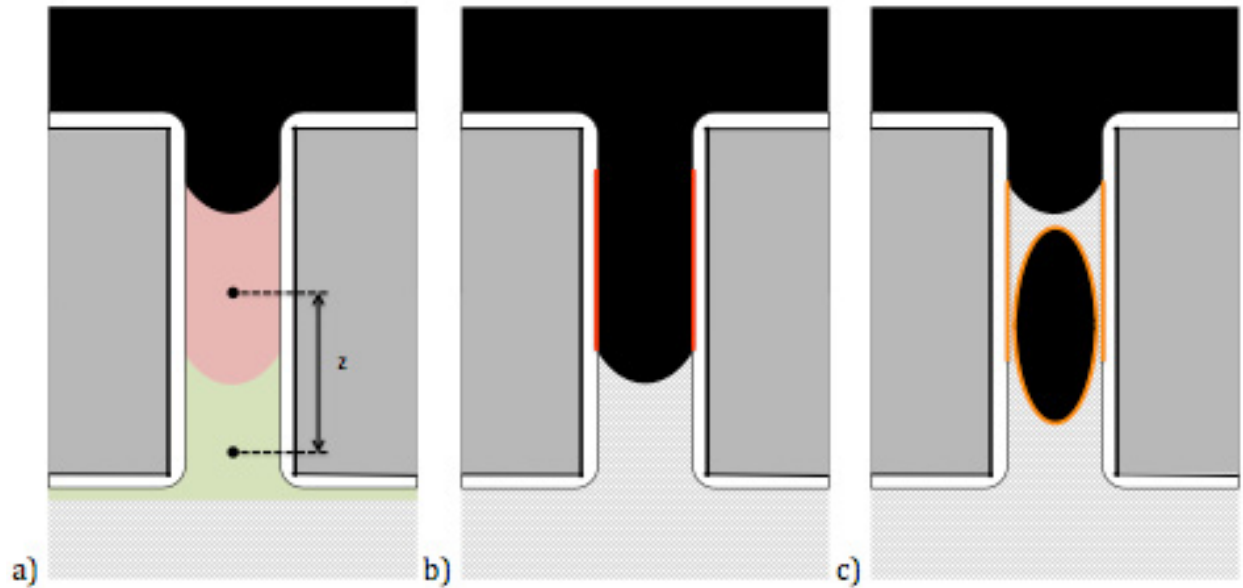
Figure 5-12: Buoyancy and interfacial area change during drop mobilization. a) Shows displacing fluid volume (green) and producing fluid volume (pink) and the potential difference in height, *z*. b) shows the interface between wetting and producing fluid that is destroyed (red) and the interface generated between displacing fluid and both producing fluid and wetting fluid (orange).

Approximation of Sloughing Enhanced Penetration Rates

In the absence of detailed information on the properties of the system, it is beneficial to look at augmented interface movement from a more general standpoint. A comparison between standard 1-D diffusion composition vs. depth profiles with an infinite boundary condition and a numerical solution where the concentration profile is set to pure solvent above a specified composition, reflecting sloughing, is instructive. An example is shown in Figure 5-13 a and b. The composition profile, arising from Fick's law, Equation 5-13, diverges further from the profile arising for an interface with a defined composition, Equation 5-14, with each sloughing event. Figure 5-13c compares interface locations based on the motion of an interface with a specific composition following episodic sloughing events, vs. Fick's law. The numerical values are purely illustrative (the composition of the interface, C_a = 0.8 mass fraction solvent, mobilization (0.25 mass fraction solvent yields a viscosity of ~10 mPa*s), and sloughing distance (1 mm), and mutual diffusion coefficient

$D = 2*10^{-10}$ m²/s [9]). Penetration rates and depths much larger than diffusion are realized following only a few sloughing events.

Solution to diffusion problem for infinite boundary

$$\frac{C_a}{C_{as}} = 1 - erf\left(\frac{y}{2\sqrt{Dt}}\right)$$

Equation 5-13

Location of given concentration from interface

$$y_{C_a} = 2\sqrt{Dt} * erfinv\left(1 - \frac{C_a}{C_{as}}\right)$$

Equation 5-14

a)　　　　　　　　　　b)　　　　　　　　　　c)
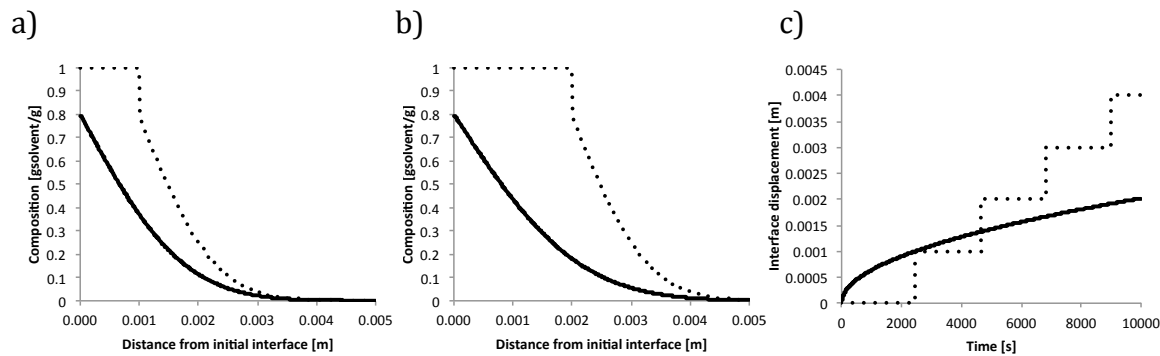
Figure 5-13: Computed composition profiles for 1-D Fickian diffusion (−) and sloughing (•••) following the first sloughing event (a) at 2450 s and the second (b) at 4648 s; c) illustrative interface displacements following successive sloughing events.

This primitive 1-D model over simplifies the 3-D geometry. There is no time lag locally between sloughing events and diffusion re-start (fluid removal is instantaneous). At elevations below the highest point of contact, episodic downward movement of diluted bitumen interferes with the solvent-bitumen contact. At higher elevations penetration proceeds more rapidly than at lower elevations. At some elevation, the interface is continuously covered by diluted bitumen and no interface movement occurs. As laboratory experiments are performed at a small scale, this critical elevation may not be identified. Field scale production rates are likely to be over predicted based on laboratory outcomes. Incorporating the impact of these effects by integrating over the height of a reservoir could

produce a relationship similar to that shown in Figure 5-1. However, such a calculation would be contingent on assumptions related to interfacial tensions, surface area to volume ratios, composition related viscosity effects, etc. and is therefore of limited value. The conditions of the experiments summarized in Figure 5-1 may reflect similar interfacial tension conditions and therefore similar conditions for sloughing. These may not be optimal for production and other conditions with lower interfacial tension should be tested.

Open Questions and Starting Points for Future Work

The scale of sloughing events plays a key role in the bitumen production rate calculation. From the Bond numbers for sloughing (Equations 5-11 and 5-12), there are a number of parameters that impact this length scale. As seen in the sample calculation based on experiments performed in a Hele–Shaw cell [4] it is possible to estimate the sloughing length scale with known system parameters. The "permeability" term in J. Nenniger's correlation may represent this length scale because other parameters, such as interfacial tension, are similar for all experiments plotted. If the sloughing can be predicted accurately from the Bond number, the production process can then be approximated using diffusion times in conjunction with the scale of sloughing events. Further experimental and computational work is required to test this possibility.

Diffusion is modeled as Fickian above but non-Fickian (Single File) and mixed mode diffusion have been observed at low solvent concentrations in bitumen [9, 12]. The consequence of this is that the power on the length scale in both the Fourier number and mass diffusion time scale is uncertain and shifts from two to four at low solvent concentrations. This solvent specific transition arises over a narrow range of asphaltene contents. As solvent penetrates more rapidly when driven by Fickian diffusion than single file diffusion, this could be the origin for the concentration shock mechanism proposed by Nenniger [6]. It would be a natural location for interface renewal with the higher concentration section sloughing from the interface leaving the single file diffusing layer in place.

Detailed application of scaling laws to thermal and solvent assisted production experiments is key to understanding their performance differences. The differences between them are governed by impacts of operating conditions on the length scale of the boundary layer. In tests where both thermal and solvent parameters are used, care must be taken to ensure the boundary conditions of the experiment reflect reservoir conditions to avoid performance dissonance arising with process scale.

The height of the pay zone in a reservoir is also important as taller sections encounter larger flows than the shorter sections. Flows spanning multiple pores are expected. Simulation or experimentation related to this topic is required to determine whether solvent assisted production processes are effective if interfaces are continuously covered in diluted bitumen that would appear to prevent solvent reaching the interface.

Interfacial tension is an important determinant of the size of the sloughing volumes and as zero interfacial tension is preferred, operating at or near the critical point of solvents should be explored. The solubility of bitumen in near critical solvents is also high [29]. The downside of operating near a critical point would be that the vapour is more-dense and the impact of the buoyancy driving force is reduced. Once interfacial tension data is collected for solvents of interest, dimensional analysis can be used to suggest whether the reduction in buoyancy force is consequential to process operation. Surfactant addition with solvent may achieve similar results to operating near the critical point of the solvent except that the mass transfer will remain primarily solvent into the bitumen. This offers some exciting possibilities for future process development using near critical solvent + water mixtures.

Finally, any method to speed up the sloughing events would benefit the overall rate of the process. Vibration, shown to significantly impact liquid gas interfaces in Chapter 4, offers a method of providing momentum to the system and potentially causing pre-mature sloughing. This enhancement would cause shorter times between sloughing events and

faster overall rates. It may also cause micro mixing to occur between solvent and bitumen at lower elevations permitting thicker reservoirs to be produced via sloughing.

Conclusions

There are two to three orders of magnitude mismatches between experimental measurements and production rates for solvent assisted production of bitumen predicted using semi-analytical models. The models are based on flawed analogies with steam assisted gravity drainage processes and do not include relevant physics.

Dimensional analysis based on the Archimedes number shows that this is not due to buoyancy driven natural convection within diluted bitumen, of solvent within diluted bitumen or of diluted bitumen within solvent.

The Bond numbers for fluid pairs diluted bitumen and solvent, and diluted bitumen and process water show that interfacial forces are much larger than buoyancy forces. Impacts of interfacial tension are not included in the semi-analytical models.

The inclusion of the impacts of interfacial tension in laboratory and field scale measurements, and their incorporation into phenomenological models is critical to the development of successful solvent assisted bitumen production processes.

The Schmidt number in the solvent assisted production process is much larger than the Prandtl number in the thermal process suggesting a different relationship between viscosity reduction and flow mechanisms in the two processes. This is another aspect where the analogy between SAGD and solvent assisted production processes fails.

A new discrete flow and diffusion mechanism, sloughing, that can account for the two to three orders of magnitude mismatch between experiments and semi-analytical models is proposed. It is based on an understanding of gravity driven snap-off in other fluid–porous

media systems and the concept of interfacial renewal or concentration shock of Das and Butler, and Nenniger. Sloughing continually introduces high concentration gradients at the interface.

Sloughing is a process where the buoyancy force on a small volume of diluted bitumen overcomes interfacial forces causing snap-off. By decreasing interfacial tension, smaller volumes of diluted bitumen become mobile thereby increasing the of rate solvent penetration and hence of production. The concept of sloughing is supported by the observed spacing of asphaltene striations in solvent assisted bitumen experiments.

More detailed understanding of interfacial tension among all phase pairs present under reservoir conditions may permit the development of a new solvent assisted bitumen production method. Conditions exhibiting near zero interfacial tensions should be investigated as potential process operating points.

Possible roles for vibration enhanced mass transfer should also be explored.

References

[1]   R. M. Butler and I. J. Mokrys, "Solvent Analog Model of Steam - Assisted Gravity Drainage," *AOSTRA J. Res.*, vol. 5, no. 1, pp. 17–32, 1989.

[2]   S. G. Dunn, E. H. Nenniger, and V. S. V. Rajan, "A Study of Bitumen Recovery by Gravity Drainage using Low Temperature Soluble Gas Injection," *Can. J. Chem. Eng.*, vol. 67, pp. 978–991, 1989.

[3]   R. Butler and I. Mokrys, "A New Process (VAPEX) For Recovering Heavy Oils Using Hot Water And Hydrocarbon Vapour," *Journal of Canadian Petroleum Technology*. 1991.

[4]   S. K. Das and R. M. Butler, "Mechanism of the Vapor Extraction Process for Heavy Oil and Bitumen," *J. Pet. Sci. Eng.*, vol. 21, no. 1–2, pp. 43–59, Sep. 1998.

[5]   S. K. Das and R. M. Butler, "Extraction of Heavy Oil and Bitumen Using Vaporized Hydrocarbon Solvents," *Pet. Sci. Technol.*, vol. 15, no. 1–2, pp. 51–75, 1997.

[6]   J. E. Nenniger, "How Fast is Solvent Based Gravity Drainage?," in *Canadian International Petroleum Conference*, 2008.

[7]   S. R. Upreti, A. Lohi, R. A. Kapadia, and R. El-Haj, "Vapor Extraction of Heavy Oil and Bitumen: A Review," *Energy & Fuels*, vol. 21, no. 3, pp. 1562–1574, May 2007.

[8]   M. T. Al-Murayri, "Experimenal Investigation of Expanding Solvent Steam Assisted Gravity Drainage using Multicomponent Solvents," 2012.

[9]   H. Fadaei, J. M. Shaw, and D. Sinton, "Bitumen–Toluene Mutual Diffusion Coefficients Using Microfluidics," *Energy & Fuels*, vol. 27, no. 4, pp. 2042–2048, Apr. 2013.

[10]   L. A. James, "Mass Transfer Mechanisms During the Solvent Recovery of Heavy Oil," University of Waterloo, 2009.

[11]   A. Sadighian, M. Becerra, A. Bazyleva, and J. M. Shaw, "Forced and Diffusive Mass Transfer between Pentane and Athabasca Bitumen Fractions," *Energy & Fuels*, vol. 25, no. 2, pp. 782–790, Feb. 2011.

[12]   M. Alizadehgiashi and J. M. Shaw, "Fickian and Non-Fickian Diffusion in Heavy Oil + Light Hydrocarbon Mixtures," *Energy & Fuels*, vol. 29, pp. 2177–2189, 2015.

[13]   R. B. Bird, W. E. Stewart, and E. N. Lightfoot, *Transport Phenomena*. John Wiley and Sons, 1960.

[14]   F. P. Incropera, D. P. Dewitt, T. L. Bergman, and A. S. Lavine, *Fundamentals of Heat and Mass Transfer*, 6th ed. John Wiley and Sons, 2006, p. 1024.

[15] S. K. Das and R. M. Butler, "Effect of Asphaltene Deposition of the VAPEX Process: A Preliminary Investigation Using a Hele–Shaw Cell," *J. Can. Pet. Technol.*, vol. 33, no. 6, 1994.

[16] F. J. Arguelles-Vivas, T. Babadagli, L. Little, N. Romaniuk, and B. Ozum, "High Temperature Density , Viscosity , and Interfacial Tension Measurements of Bitumen – Pentane – Biodiesel and Process Water Mixtures," *J. Chem. Eng. Data*, vol. 57, pp. 2878–2889, 2012.

[17] A. Yazdani J. and B. B. Maini, "Effect of Drainage Height and Grain Size on the Convective Dispersion in the Vapex Process : Experimental Study," SPE Symposium on Improved Oil Recovery, 2004.

[18] S. Taheri, S. Ghomeshi, and A. Kantzas, "Permeability Calculations in Unconsolidated Sands," in *GeoConvention 2014: FOCUS*, 2014, pp. 1–4.

[19] K. Takamura, "Microscopic Structure of Athabasca Oil Sand," *Can. J. Chem. Eng.*, vol. 60, no. 4, pp. 538–545, Aug. 1982.

[20] C. Yang and Y. Gu, "Effects of Heavy-Oil / Solvent Interfacial Tension on Gravity Drainage in the Vapor Extraction (Vapex) Process," in *SPE/PS-CIM/CHOA International Thermal Operations and Heavy Oil Symposium*, 2005.

[21] E. W. Lemmon, M. O. McLinden, and D. G. Friend, "NIST Chemistry WebBook, NIST Standard Reference Database Number 69," P. J. Linstrom and W. G. Mallard, Eds. Gaithersburg MD, 20899: National Institute of Standards and Technology.

[22] "ConocoPhillips Surmont SAGD In Situ Performance Data 2013," 2013. [Online]. Available: http://www.aer.ca/documents/oilsands/insitu-presentations/2013AthabascaConocoSurmontSAGD9426.zip. [Accessed: 22-Feb-2015].

[23] "Shell Canada Limited Orion SAGD In Situ Performance Data 2013," 2013. [Online]. Available: http://www.aer.ca/documents/oilsands/insitu-presentations/2013ColdLakeShellOrionSAGD10103.zip. [Accessed: 22-Feb-2015].

[24] M. R. Cervenan, F. E. Vermeulen, and F. S. Chute, "Thermal Conductivity and Specific Heat of Glasses," *Phys. Rev. B*, vol. 36, pp. 7620–7624, 1987.

[25] W. Deng, M. B. Cardenas, and P. C. Bennett, "Extended Roof Snap-off for a Continuous Nonwetting Fluid and an Example Case for Supercritical CO2," *Adv. Water Resour.*, vol. 64, pp. 34–46, 2014.

[26] K. E. Lapo, L. M. Hinkelman, M. S. Raleigh, and J. D. Lundquist, "Influence of Dynamic Factors on Nonwetting Fluid Snap-off in Pores," *Water Resour. Res.*, vol. 51, pp. 1–8, 2015.

[27] N. R. Morrow, "Physics and Thermodynamics of Capillary Action in Porous Media," *Ind. Eng. Chem.*, vol. 62, pp. 32–56, 1970.

[28] R. J. Glass and L. Yarrington, "Mechanistic Modeling of Fingering, Nonmonotonicity, Fragmentation, and Pulsation within Gravity/Buoyant Destabilized Two-phase/Unsaturated Flow," *Water Resour. Res.*, vol. 39, no. 3, p. 1058, 2003.

[29] X.-Y. Zou, X. Zhang, and J. a. M. Shaw, "Phase Behavior of Athabasca Vacuum Bottoms + n-Alkane Mixtures," *SPE Prod. Oper.*, vol. 22, no. August 2005, pp. 265–272, 2007.

Chapter 6: Conclusions and Future Work

Conclusions

Changes in the movement of fluids in unconsolidated porous media, due to the addition of solvents and vibration, and with specific application to heavy oil recovery in Alberta's oil sands are addressed. Solvent addition to the heavy oil changes fluid properties such as density, viscosity and interfacial tension between phases that govern the fluid dynamics of the system. Vibration is present in laboratories and industrial facilities at frequencies that directly impact fluid dynamics, particularly where bubbles are present. Vibration induced phenomena alter media properties and flow behaviors. Untangling the interaction among these effects is complex. Specific topics are addressed in chapters two, three, four and five.

Phase order inversion of diluted bitumen and water is described in Chapter two. This is important to the buoyancy driving force for bitumen production particularly when steam and solvent are co-injected. Phase order inversion causes preferential production of water over the diluted bitumen and therefore prevents generation of a solvent trap above the producing well. This means that either diluted bitumen floats on a water layer above the producer or that solvent and steam short circuit from the injector to the producer. Phase order inversion is also important in surface facilities where separation of diluted bitumen from water is based on buoyancy.

Specific conclusions from Chapter two:
- Addition of low molar mass solvents to facilitate production, as currently envisioned by the petroleum industry, leads to an inversion in the phase order of water and diluted bitumen over a broad range of pressures and temperatures even if only a small mass fraction of solvent is added to the hydrocarbon resource.
- Phase inversion envelopes for Athabasca bitumen + heptane and toluene illustrate the principles, and the quantitative outcomes, including composition ranges exhibiting two inversion temperatures at fixed pressure, and the pressure insensitivity to envelope placement in the phase diagram are readily generalized.

- Excess volumes for Athabasca bitumen + toluene and heptane mixtures, can be assumed to be zero within experimental uncertainty over broad ranges of conditions due to irreducible uncertainties arising in the Athabasca bitumen density measurements that mask potential non-ideal mixing effects.

- The impact of non-ideal mixing on phase envelope placement is expected to be significant and systematic, in general, above a reduced temperature for the solvent of 0.85.

The design and testing of a Dynamic Pressure View Cell (DPVC) that was built to investigate bubble formation and movement in liquids, and liquid–bubble interaction in unconsolidated porous media is described in Chapter three. Vibration causes fluids to cavitate and unconsolidated porous media to move. Preliminary tests with this new device suggested that the frequency range of vibrations in laboratory and industrial facilities cause motion of fluids and unconsolidated porous media. The large amplitude motion of bubbles, both present and formed in situ due to vibration has the potential to cause mixing within porous media.

Specific conclusions from Chapter three:
- The Dynamic Pressure View Cell permits the exploration of vibrations in fluids at industrially relevant frequencies from 10 to 5000 Hz, and amplitudes of at least 80 kPa and up to 500 kPa filling a gap in the range of frequencies covered by existing apparatus.

- Visualization of the impact of vibrations such as bubble formation, bubble motion and media motion is demonstrated down to a length scale of 180 μm.

- Resonance was apparent and resonant frequencies are shown to depend on the fluid, the presence or generation of bubbles and the presence of porous media.

- Videos of fluid cavitation and the accompanying changes in the resonant response allow the device to be used to study micro bubble generation and the impact of micro bubbles on non-isotropic miscible mixtures and immiscible mixtures in porous media.

Impacts of vibration on bubble–liquid–unconsolidated porous media with the use of scaling groups and experiments are reviewed in Chapter four. Scaling groups, including the Womersley number, viscous diffusion time, viscous and inertial response time, bubble resonant frequency, and a particle force balance, were used to describe flow mechanisms over the industrially relevant frequency and length scales.   For single-phase liquids, flat as opposed to parabolic velocity profiles are expected in micro porous media at frequencies exceeding ~ 10 Hz. The unconsolidated porous medium is expected to become mobile at frequencies greater than ~ 50 Hz. Dispersed micro-scale liquid drops are expected to deform from near 0 Hz to more than 1000 Hz. Size dependent bubble movement is expected at all frequencies. Interactions among the mechanisms were not resolved by analysis, and experiments were conducted at 50 Hz and 500 Hz to observe which one or ones dominate. Drop deformation and velocity profiles were not observed experimentally. However, particle movement and local particle bed compaction/channel formation were readily observed at both 50 Hz and 500 Hz. Bubbles, whether present or generated in situ disrupted behaviors otherwise observed. They compacted the sand bed, caused unconsolidated porous media motion, displaced the non-wetting liquid phase (if present), and caused particle mixing among other effects. The observed dominance of the combination of bubbles plus vibration on the behavior of bubble–fluid–porous media systems presents many areas of application for future study, from the impact of episodic seismic activity on aquifer properties, to vibration enhanced hydrocarbon production and carbon dioxide sequestration technology development, to the resolution of dissonance in performance between lab, pilot and industrial scale processes where vibrations and gas content is not carefully controlled.

Specific conclusions from Chapter four:
- Vibrations of industrially relavent frequency range are shown through scaling analysis to cause bulk velcity profile modification, drop deformation bubble compression and media motion.
- Vibration of bubbles, whether present or generated in situ, disrupted behaviors otherwise observed.

- Vibrating bubbles compacted the sand bed, caused unconsolidated porous media motion, displaced the non-wetting liquid phase (if present), and caused particle mixing among other effects.

The reported two to three orders of magnitude mismatch between semi-analytical predicted and experimental production rates for solvent assisted bitumen production processes is examined in Chapter 5. Comparative analysis using dimensionless groups to scale distance and time permits comparisons between assumptions in the semi-analytical models and what is physically possible at the pore scale. Drawing on conclusions from Chapter 2 and building onto the pore scale force balance arguments developed in Chapter 4, it is shown that while conventional natural and forced convection mass transfer mechanisms at interfaces can account for two order of magnitude increases in mass transfer, in general, these mechanisms are infeasible at the length scales arising in porous media. Analysis also reveals the importance of interfacial tension, an effect neglected in the semi-analytical production models, and the episodic nature of processes at the solvent-bitumen interface. Sloughing—a new mechanism for interface renewal and concentration shock driven by interfacial tension is proposed. This mass transfer enhancement mechanism is supported by observations in the literature. The need for production condition interfacial tension measurements, additional constraints in experiments and the potential for rate optimization in hydrocarbon production processes are discussed.

Specific conclusions from Chapter five:
- Semi-analytical models of solvent assisted production of bitumen are based on flawed analogies with steam assisted gravity drainage processes and do not include relevant physics as exhibited by the Bond number, Archimedes number, Fourier number, Prandlt number and Schmidt number.
- A new discrete flow and diffusion mechanism, sloughing, that can account for the two to three orders of magnitude mismatch between experiments and semi-analytical models is proposed whereby buoyancy overcomes interfacial forces of

small sections of fluid causing local high concentration gradients and associated accelerated mass transfer.

- The concept of sloughing is supported by the observed spacing of asphaltene striations in solvent assisted bitumen experiments.

Future Work

Phase order inversion should be investigated in specific reservoir and processing situations. There are situations where small changes in temperature can cause phase order inversion to occur that may be beneficial/harmful in process applications.

Opportunities for future work, whether related specifically to solvent aided bitumen production or to other fields and industries, were identified. Many involve applications of the DPVC.

The DPVC operation can be improved through further development of equipment and data interpretation.

- A high speed camera and stand with automated focus controls would increase resolution, repeatability between images and provide for more detailed observation of dynamic events that currently can only be observed due to temporal summation of events
- Introduction of a higher frequency Variable Frequency Drive (VFD) to allow operation through the 120-500 Hz range (note: Eaton claimed to have this but upon delivery it was found that it was only capable up to 120 Hz)
- Different actuators can be developed to more precisely control the transmitted waveform to observe the impact it has on bubble shape deformation
- Quantitative interpretation of transmitted signals

The scaling analysis of vibrations in porous media and associated literature review only scratch the surface of potential applications. Opportunities exist within porous media but

the impact of vibrations on bubbles is equally important in other areas of science. Within the focused field of application of vibration induced motion in unconsolidated porous media areas of future work include determining if:

- Vibrating bubbles can be used to accelerate communication between well pairs,
- Vibrating bubbles can be used as a transport mechanism for surface active species (asphaltenes, catalysts, nanoparticles, nano-devices),
- Vibration can improve gas–liquid mass transfer in porous media through enhancements to "snap-off",
- Resonance can be used to control the location of bubbles within a media or packed vessels and therefore locally target vibration impacts or transported particles,
- Vibration induced media motion can be utilized as a method to reduce particle size in coking and conversely can vibration isolation be used to protect catalysts from abrasion.

Finally, it is hoped that the insights gained through Chapter five allow researchers to focus on methods of improving solvent aided bitumen production to allow a reduction in greenhouse gas emissions to be realized. Future work is required to not only support the hypothesis but to determine how it can be applied to realize the benefits of solvent aided production:

- Measure interfacial tension at reservoir conditions between all four phases (gas, hydrocarbon liquid, aqueous liquid, and solid media),
- Determine applicability of sloughing through direct observation,
- Determine if J. Nenniger's correlation can be linked to sloughing through volume to surface area ratio in the critical sloughing Bond number,
- Explore impact of single file diffusion limit on sloughing,
- Explore near critical point solvents as an interfacial tension reduction technique to increase sloughing frequency,

- Explore whether vibration can be utilized to initiate sloughing as it does bubble motion.

The future work outlined above contains many potential equipment improvements, hypothesis to be developed and tested, and avenues to explore within the specific area of application to solvent aided bitumen production and beyond. The author hopes that this thesis and supporting equipment provide a solid starting point for these future works.

Bibliography

Abedi, S. J., Cai, H.-Y., Seyfaie, S., & Shaw, J. M. (1999). Simultaneous Phase Behaviour, Elemental Composition and Density Measurement using X-ray Imaging. *Fluid Phase Equilibria*, *158-160*, 775–781. doi:10.1016/S0378-3812(99)00109-0

Al-Murayri, M. T. (2012). *Experimenal Investigation of Expanding Solvent Steam Assisted Gravity Drainage using Multicomponent Solvents*.

Alizadehgiashi, M., & Shaw, J. M. (2015). Fickian and Non-Fickian Diffusion in Heavy Oil + Light Hydrocarbon Mixtures. *Energy & Fuels*, *29*, 2177–2189. doi:10.1021/ef502699c

Alvarez, J., & Han, S. (2013). Current Overview of Cyclic Steam Injection Process. J. Pet. Sc. Res., *2*(3), 116–127.

Amani, M. J., Gray, M. R., & Shaw, J. M. (2013a). Phase Behavior of Athabasca Bitumen+Water Mixtures at High Temperature and Pressure. *The Journal of Supercritical Fluids*, *77*, 142–152. doi:10.1016/j.supflu.2013.03.007

Amani, M. J., Gray, M. R., & Shaw, J. M. (2013b). Volume of Mixing and Solubility of Water in Athabasca Bitumen at High Temperature and Pressure. *Fluid Phase Equilibria*, *358*, 203–211. doi:10.1016/j.fluid.2013.07.021

Amani, M. J., Gray, M. R., & Shaw, J. M. (2014). The Phase Behavior of Athabasca Bitumen + Toluene + Water Ternary Mixtures. *Fluid Phase Equilibria*. doi:10.1016/j.fluid.2014.02.028

Arguelles-Vivas, F. J., Babadagli, T., Little, L., Romaniuk, N., & Ozum, B. (2012). High Temperature Density , Viscosity , and Interfacial Tension Measurements of Bitumen – Pentane – Biodiesel and Process Water Mixtures. *Journal of Chemical & Engineering Data*, *57*, 2878–2889.

Badamchi-Zadeh, A., Yarranton, H., Maini, B., & Satyro, M. (2009). Phase Behaviour and Physical Property Measurements for VAPEX Solvents: Part II. Propane, Carbon Dioxide and Athabasca Bitumen. *Journal of Canadian Petroleum Technology*, *48*(3). doi:10.2118/09-03-57

Badamchi-Zadeh, A., Yarranton, H., Svrcek, W., & Maini, B. (2009). Phase Behaviour and Physical Property Measurements for VAPEX Solvents: Part I. Propane and Athabasca Bitumen. *Journal of Canadian Petroleum Technology*, *48*(1). doi:10.2118/09-01-54

Bazyleva, A., Fulem, M., Becerra, M., Zhao, B., & Shaw, J. M. (2011). Phase Behavior of Athabasca Bitumen. *Journal of Chemical & Engineering Data*, *56*(7), 3242–3253. doi:10.1021/je200355f

Beresnev, I. A. (2006). Theory of Vibratory Mobilization on Nonwetting Fluids Entrapped in Pore Constrictions. *Geophysics*, *71*(6).

Beresnev, I. A., & Deng, W. (2010). Theory of Breakup of Core Fluids Surrounded by a Wetting Annulus in Sinusoidally Constricted Capillary Channels. *Physics of Fluids*, *22*(2010), 012105. doi:10.1063/1.3294887

Beresnev, I. A., & Johnson, P. A. (1994). Elastic-wave Stimulation of Oil Production: A Review of Methods and Results. *Geophysics*, *59*(6), 1000–1017. doi:10.1190/1.1443645

Beresnev, I., Gaul, W., & Vigil, R. D. (2011). Direct Pore-level Observation of Permeability Increase in Two-phase Flow by Shaking. *Geophysical Research Letters*, *38*(20), n/a–n/a. doi:10.1029/2011GL048840

Biot, M. A. (1956). Theory of Propagation of Elastic Waves in a Fluid-Saturated Porous Solid. I. Low-Frequency Range. *The Journal of the Acoustical Society of America*, *28*(2).

Bird, R. B., Stewart, W. E., & Lightfoot, E. N. (1960). *Transport Phenomena*. John Wiley and Sons.

Bormann, P. (2009). *New Manual of Seismological Observatory Practice - NMSOP. New Manual of IASPEI Seismological Observatory Practice (NMSOPM)* (p. 1162). doi:10.2312/GFZ.NMSOP

Brandt, A. (2011). *Upstream Greenhouse Gas Emissions from Canadian Oil Sands as a Feedstock for European Refineries. A Report Prepared for the European Commission* (pp. 1–51). Retrieved from https://circabc.europa.eu/d/d/workspace/SpacesStore/db806977-6418-44db-a464-20267139b34d/Brandt_Oil_Sands_GHGs_Final.pdf

Butler, R. M. (1979). Method for Continuously Producing Viscous Hydrocarbons by Gravity Drainage while Injecting Heated Fluids. Canada.

Butler, R. M., Mcnab, G. S., & Lo, H. Y. (1981). Theoretical Studies on the Gravity Drainage of Heavy Oil During In-situ Steam Heating. *The Canadian Journal of Chemical Engineering*, *59*(August), 455–460.

Butler, R. M., & Mokrys, I. J. (1989). Solvent Analog Model of Steam - Assisted Gravity Drainage. *AOSTRA Journal of Research*, *5*(1), 17–32.

Butler, R., & Mokrys, I. (1991). A New Process (VAPEX) For Recovering Heavy Oils Using Hot Water And Hydrocarbon Vapour. *Journal of Canadian Petroleum Technology*. doi:10.2118/91-01-09

Cassiede, M., & Shaw, J. M. (2015). Non-Intrusive, High-Resolution, Real-time, Two-Dimensional Imaging of Multiphase Materials Using Acoustic Array Sensors. *Review of Scientific Instruments*.

Cervenan, M. R., Vermeulen, F. E., & Chute, F. S. (1987). Thermal Conductivity and Specific Heat of Glasses. *Physical Review B*, *36*, 7620–7624.

Chrysikopoulos, C. V., & Vogler, E. T. (2006). Acoustically Enhanced Ganglia Dissolution and Mobilization in a Monolayer of Glass Beads. *Transport in Porous Media*, *64*(1), 103–121. doi:10.1007/s11242-005-1525-8

ConocoPhillips Surmont SAGD In Situ Performance Data 2013. (2013). Retrieved February 22, 2015, from http://www.aer.ca/documents/oilsands/insitu-presentations/2013AthabascaConocoSurmontSAGD9426.zip

Das, S. K., & Butler, R. M. (1994). Effect of Asphaltene Deposition of the VAPEX Process: A Preliminary Investigation Using a Hele-Shaw Cell. *Journal of Canadian Petroleum Technology*, *33*(6).

Das, S. K., & Butler, R. M. (1997). Extraction of Heavy Oil and Bitumen Using Vaporized Hydrocarbon Solvents. *Petroleum Science and Technology*, *15*(1-2), 51–75.

Das, S. K., & Butler, R. M. (1998). Mechanism of the Vapor Extraction Process for Heavy Oil and Bitumen. *Journal of Petroleum Science and Engineering*, *21*(1-2), 43–59. doi:10.1016/S0920-4105(98)00002-3

Deng, W., & Cardenas, M. B. (2013). Dynamics and Dislodgment from Pore Constrictions of a Trapped Nonwetting Droplet Stimulated by Seismic Waves. *Water Resources Research*, *49*(October 2012), 4206–4218. doi:10.1002/wrcr.20335

Deng, W., Cardenas, M. B., & Bennett, P. C. (2014). Extended Roof Snap-off for a Continuous Nonwetting Fluid and an Example Case for Supercritical CO2. *Advances in Water Resources*, *64*, 34–46. doi:10.1016/j.advwatres.2013.12.001

DIPPR Project 801 - Full Version. (2012). Design Institute for Physical Property Research/AIChE. Retrieved from http://www.knovel.com/web/portal/browse/display?_EXT_KNOVEL_DISPLAY_bookid=1187

Domenico, S. N. (1982). Acoustic Wave Propagation in Air-bubble Curtains in Water- Part I : History and Theory. *Geophysics*, *47*(3), 345–353.

Dunn, S. G., Nenniger, E. H., & Rajan, V. S. V. (1989a). A Study of Bitumen Recovery by Gravity Drainage using Low Temperature Soluble Gas Injection. *The Canadian Journal of Chemical Engineering*, *67*, 978–991. doi:10.1002/cjce.5450670617

Ellenberger, J., van Baten, J. M., & Krishna, R. (2003). Intensification of Slurry Bubble Columns by Vibration Excitement. *Catalysis Today*, *79-80*(August), 181–188. doi:10.1016/S0920-5861(03)00003-8

Fadaei, H., Shaw, J. M., & Sinton, D. (2013). Bitumen–Toluene Mutual Diffusion Coefficients Using Microfluidics. *Energy & Fuels*, *27*(4), 2042–2048. doi:10.1021/ef400027t

Firoozabadi, A., & Ishimoto, K. (1994). Reinfiltration in Fractured Porous Media: Part 1 - One Dimentional Model. *SPE Advanced Technology Series*, *2*(2), 35–44.

Firoozabadi, A., Ishimoto, K., & Dindoruk, B. (1994). Reinfiltration in Fractured Porous Media: Part 2 - Two Dimentional Model. *SPE Advanced Technology Series*, *2*(2), 45–51.

Glass, R. J., & Yarrington, L. (2003). Mechanistic Modeling of Fingering, Nonmonotonicity, Fagmentation, and Pulsation within Gravity/Buoyant Destabilized Two-phase/Unsaturated Flow. *Water Resour. Res.*, *39*(3), 1058. doi:10.1029/2002wr001542

Government of Alberta. (2012). Oil Sands: The Resource. Retrieved March 19, 2016, from http://www.oilsands.alberta.ca/FactSheets/Resource_FSht_June_2012_Online.pdf

Graham, D. R., & Higdon, J. J. L. (2000). Oscillatory Flow of Droplets in Capillary Tubes. Part 1. Straight Tubes. *Journal of Fluid Mechanics*, *425*, 31–53. doi:10.1017/S0022112000002020

Guan, J. G., Kariznovi, M., Nourozieh, H., & Abedi, J. (2013). Density and Viscosity for Mixtures of Athabasca Bitumen and Aromatic Solvents. *Journal of Chemical & Engineering Data*, *58*(3), 611–624. doi:10.1021/je3010722

Guidelines for the Avoidance of Vibration Induced Fatigue Failure in Process Pipework. (2008). Energy Institute (Great Britain).

Gupta, S., Gittins, S., Sood, A., Zeidani, K., & Energy, C. (2010). Optimal Amount of Solvent in Solvent Aided Process. In *Canadian Unconventional Resources & International Petroleum Conference* (pp. 19–21). Calgary, Alberta.

Hale, B. Y. J. F., Mcdonald, D. A., & Womersley, J. R. (1955). Velocity Profiles of Oscillating Arterial Flow, with some Calculations of Viscous Drag and the Reynolds Number. *Journal of Physiology - London*, (23), 629–640.

Hamida, T., & Babadagli, T. (2007). Immiscible Displacement of Oil by Water in Consolidated Porous Media due to Capillary Imbibition under Ultrasonic Waves. *The Journal of the Acoustical Society of America*, *122*(3), 1539. doi:10.1121/1.2756190

Hatzikiriakos, S. G., Gaikwad, R. P., Nelson, P. R., & Shaw, J. M. (1990). Hydrodynamics of Gas-Agitated Liquid-Liquid dispersions. *AIChE Journal*, *36*(5), 677–684.

Iassonov, P. P., & Beresnev, I. A. (2008). Mobilization of Entrapped Organic Fluids by Elastic Waves and Vibrations. *SPE Jounal*, (December), 465–473.

IHS CERA. (2012). *Oil Sands, Greenhouse Gases, and US Oil Supply: Getting the Numbers Right*. Retrieved from http://www.api.org/~/media/Files/ Oil-and-Natural-Gas/Oil_Sands/CERA_Oil_Sands_GHGs_US_Oil_Supply.pdf

Incropera, F. P., Dewitt, D. P., Bergman, T. L., & Lavine, A. S. (2006). *Fundamentals of Heat and Mass Transfer* (6th ed., p. 1024). John Wiley and Sons.

Introduction to nondestructive testing. (2016). Retrieved May 24, 2016, from https://www.asnt.org/MinorSiteSections/AboutASNT/Intro-to-NDT

J, A. Yazdani., & Maini, B. B. (2004). Effect of Drainage Height and Grain Size on the Convective Dispersion in the Vapex Process : Experimental Study. *SPE Symposium on Improved Oil Recovery.*

James, L. A. (2009). *Mass Transfer Mechanisms During the Solvent Recovery of Heavy Oil*. University of Waterloo.

Khammar, M., & Shaw, J. M. (2011). Phase Behaviour and Phase Deparation Kinetics Measurement using Acoustic Arrays. *Review of Scientific Instruments*, *82*(10). doi:10.1063/1.3650767

Kim, B.-N., Yoon, S. W., Choi, B. K., & Jung, S.-K. (2012). Gas Void Fraction Estimation in Gas-Bubble-Contained Sands with Difference Frequency Waves. *Japanese Journal of Applied Physics*, *51*. doi:10.1143/JJAP.51.07GD02

Krishna, R., Ellenberger, J., Urseanu, M. I., & Keil, F. J. (2000). Utilisation of Bubble Resonance Phenomena to Improve Gas-liquid Contact. *Naturwissenschaften*, *87*, 455–459. doi:10.1007/s001140050758

Lapo, K. E., Hinkelman, L. M., Raleigh, M. S., & Lundquist, J. D. (2015). Influence of Dynamic Factors on Nonwetting Fluid Snap-off in Pores. *Water Resources Research*, *51*, 1–8. doi:10.1002/2014WR016259

Leighton, T. G., Walton, J., & Pickworth, M. J. W. (1990). Primary Bjerknes Forces. *European Journal of Physics*, *11*, 47–50.

Lemmon, E. W., McLinden, M. O., & Friend, D. G. (n.d.). NIST Chemistry WebBook, NIST Standard Reference Database Number 69. In P. J. Linstrom & W. G. Mallard (Eds.), . Gaithersburg MD, 20899: National Institute of Standards and Technology. Retrieved from http:

Li, W., Vigil, R. D., Beresnev, I. A., Iassonov, P., & Ewing, R. (2005). Vibration-induced Mobilization of Trapped Oil Ganglia in Porous Media: Experimental Validation of a

Capillary-physics Mechanism. *Journal of Colloid and Interface Science*, *289*(1), 193–199. doi:10.1016/j.jcis.2005.03.067

Licence, P., Dellar, M. P., Wilson, R. G. M., Fields, P. A., Litchfield, D., Woods, H. M., … Howdle, S. M. (2004). Large-aperture Variable-volume View Cell for the Determination of Phase-equilibria in High Pressure Systems and Supercritical Fluids. *Review of Scientific Instruments*, *75*(10), 3233–3236. doi:10.1063/1.1790563

Liu, R. H., Yang, J., Pindera, M. Z., Athavale, M., & Grodzinski, P. (2002). Bubble-induced Acoustic Micromixing. *Lab on a Chip*, *2*, 151–157. doi:10.1039/b201952c

Mason, T. J., & Lorimer, J. P. (2002). Applied Sonochemistry The Uses of Power Ultrasound in Chemistry and Processing.

Mehrotra, A. K., & Svrcek, W. Y. (1985a). Viscosity, Density and Gas Solubility Data for Oil Sand Bitumens. Part 1: Athabasca Bitumen Saturated with CO and C2H6. *AOSTRA Journal of Research*, *1*(4), 263–268.

Mehrotra, A. K., & Svrcek, W. Y. (1985b). Viscosity, Density and Gas Solubility Data for Oil Sand Bitumens. Part II: Peace River Bitumen Saturated with N2, CO, CH4, CO2 and C2H6. *AOSTRA Journal of Research*, *1*(4), 269–279.

Meldin, W. I., Masse, L., & Zumwalt, G. L. (1983). United States Patent 4417621. United States.

Montemagno, C. D., & Gray, W. G. (1995). Photoluminescent Volumetric Imaging : A Technique for the Exploration of Multiphase Flow and Transport in Porous Media. *Geophysical Research Letters*, *22*, 425–428.

Morrow, N. R. (1970). Physics and Thermodynamics of Capillary Action in Porous Media. *Industrial & Engineering Chemistry*, *62*, 32–56. doi:10.1021/ie50726a006

Motahhari, H., Schoeggl, F. F., & Satyro, M. A. (2011). Prediction of the Viscosity of Solvent Diluted Live Bitumen at Temperatures up to 175° C. In *Canadian Society for Unconventional Gas* (pp. 1–19).

Muhamad, H., Upreti, S. R., Lohi, A., & Doan, H. (2012). Performance Enhancement of VAPEX by Temporal Variation of Solvent Injection Pressure. *Journal of Petroleum Science and Engineering*, *97*, 93–101.

Naderi, K., & Babadagli, T. (2011). Pore-scale Investigation of Immiscible Displacement Process in Porous Media under High-frequency Sound Waves. *Journal of Fluid Mechanics*, *680*, 336–360. doi:10.1017/jfm.2011.166

Nenniger, J. E. (2008). How Fast is Solvent Based Gravity Drainage? In *Canadian International Petroleum Conference*. Calgary, Alberta.

Nikolaevskii, V. N. (1993). Rock Vibration and Finite Oil Recovery. *Izvestuya Rossi*, (5), 689–696.

Oil Sands Discovery Centre. (2014). *Facts about Alberta's Oil Sands and its Industry*. *Government of Alberta* (pp. 3–5). Retrieved from http://history.alberta.ca/oilsands/resources/docs/facts_sheets09.pdf

Piping Vibration Analysis & Integrity Assessment | BETA Machinery Analysis. (n.d.). Retrieved from http://www.betamachinery.com/services/piping-vibration-and-integrity-assessment

Pittard, M. T., Evans, R. P., Maynes, R. D., & Blotter, J. D. (2004). Experimental and Numerical Investigation of Yurbulent Flow Induced Pipe Vibration in Fully Developed Flow. *Review of Scientific Instruments*, *75*(7). doi:10.1063/1.1763256

Qing, M., Jinghui, Z., Yushan, L., Haijun, W., & Quan, D. (2006). Experimental Studies of Orifice-induced Wall Pressure Fluctuations and Pipe Vibration. *International Journal of Pressure Vessels and Piping*, *83*(7), 505–511. doi:10.1016/j.ijpvp.2006.03.010

Rigord, P., Caristan, Y., & Hulin, J. P. (1993). Analysis of Porous Media Heterogeneities Using the Diffusion of Pressure Waves. *Journal of Geophysical Research*, *98*, 9781–9791.

Rostami, B., Kharrat, R., Pooladi-Darvish, M., & Ghotbi, C. (2009). Identification of Fluid Dynamics in Forced Gravity Drainage Using Dimensionless Groups. *Transport in Porous Media*, *83*(3), 725–740. doi:10.1007/s11242-009-9478-y

Ruark, A. E. (1935). Inspectional Analysis - A Method which Supplements Dimensional Analysis. *Journal of the Mitchell Society*.

Saber, N., & Shaw, J. M. (2011). On the Phase Behaviour of Athabasca Vacuum Residue+n-Decane. *Fluid Phase Equilibria*, *302*(1-2), 254–259. doi:10.1016/j.fluid.2010.09.038

Sadighian, A., Becerra, M., Bazyleva, A., & Shaw, J. M. (2011). Forced and Diffusive Mass Transfer between Pentane and Athabasca Bitumen Fractions. *Energy & Fuels*, *25*(2), 782–790. doi:10.1021/ef101435r

Shaw, J. M. (2003). A Microscopic View of Oil Slick Break-up and Emulsion Formation in Breaking Waves. *Spill Science & Technology Bulletin*, *8*(5-6), 491–501. doi:10.1016/S1353-2561(03)00061-6

Sheikha, H., & Pooladi-Darvish, M. (2012). Micro Bubbles in Solution–Gas Drive in Heavy Oil: Their Existence and Importance. *Transport in Porous Media*, *93*(3), 495–516. doi:10.1007/s11242-012-9965-4

Shell Canada Limited Orion SAGD In Situ Performance Data 2013. (2013). Retrieved February 22, 2015, from http://www.aer.ca/documents/oilsands/insitu-presentations/2013ColdLakeShellOrionSAGD10103.zip

Silberman, E. (1957). Sound Velocity and Attenuation in Bubbly Mixtures Measured in Standing Wave Tubes. *The Journal of the Acoustical Society of America*, *29*(8), 925–933.

Sparlin, D. D. (1974). Sand and Gravel - A Study of their Permeabilities SPE 4772. In *Offshore Technology Conference*.

Spence, R., & Amaral-Teixeira, J. (2008). Investigation into Pressure Pulsations in a Centrifugal Pump using Numerical Methods Supported by Industrial Tests. *Computers and Fluids*, *37*, 690–704. doi:10.1016/j.compfluid.2007.10.001

Stohr, M., Roth, K., & Jahne, B. (2003). Measurement of 3D Pore-scale Flow in Index-Matched Porous Media. *Experiments in Fluids*, *35*(2), 159–166. doi:10.1007/s00348-003-0641-x

Taheri, S., Ghomeshi, S., & Kantzas, A. (2014). Permeability Calculations in Unconsolidated Sands. In *GeoConvention 2014: FOCUS* (pp. 1–4).

Takamura, K. (1982). Microscopic Dtructure of Athabasca Oil Sand. *The Canadian Journal of Chemical Engineering*, *60*(4), 538–545. doi:10.1002/cjce.5450600416

Thomas, J. M., & Chrysikopoulos, C. V. (2007). Experimental Investigation of Acoustically Enhanced Colloid Transport in Water-saturated Packed Columns. *Journal of Colloid and Interface Science*, *308*(1), 200–207. doi:10.1016/j.jcis.2006.12.062

U.S. Department of of Energy. (2014). EIA International Energy Statistics. Retrieved March 19, 2016, from http://www.eia.gov/cfapps/ipdbproject/iedindex3.cfm?tid=5&pid=57&aid=6&cid=regions&syid=2010&eyid=2014&unit=BB

Upreti, S. R., Lohi, A., Kapadia, R. A., & El-Haj, R. (2007). Vapor Extraction of Heavy Oil and Bitumen: A Review. *Energy & Fuels*, *21*(3), 1562–1574. doi:10.1021/ef060341j

Vandu, C. O., Ellenberger, J., & Krishna, R. (2005). Hydrodynamics and Mass Transfer in an Upflow Monolith Loop Reactor. *Chemical Engineering and Processing: Process Intensification*, *44*, 363–374. doi:10.1016/j.cep.2004.05.011

Vandu, C. O., Liu, H., & Krishna, R. (2005). Mass Transfer from Taylor Bubbles Rising in Single Capillaries. *Chemical Engineering Science*, *60*, 6430–6437. doi:10.1016/j.ces.2005.01.037

Wallach, R., Margolis, M., & Graber, E. R. (2013). The Role of Contact Angle on Unstable Flow Formation During Infiltration and Drainage in Wettable Porous Media. *Water Resources Research*, *49*(October), 6508–6521. doi:10.1002/wrcr.20522

Werth, C. J., Zhang, C., Brusseau, M. L., Oostrom, M., & Baumann, T. (2010). A Review of Non-invasive Imaging Methods and Applications in Contaminant Hydrogeology Research. *Journal of Contaminant Hydrology*, *113*(1-4), 1–24. doi:10.1016/j.jconhyd.2010.01.001

White, F. M. (2008). *Fluid Mechanics* (6th ed.). New York: McGraw Hill. doi:10.1007/b138775

Womersley, J. R. (1955). Method for the Calculation of Velocity, Rate of Flow and Viscous Drag in Arteries when the Pressure Gradient is Known. *Journal of Physiology*, *127*, 553–563.

Wood, A. B. (1930). *A Textbook of Sound*. London: G. Bell and Sons Ltd.

Yang, C., & Gu, Y. (2005). Effects of Heavy-Oil / Solvent Interfacial Tension on Gravity Drainage in the Vapor Extraction (Vapex) Process. In *SPE/PS-CIM/CHOA International Thermal Operations and Heavy Oil Symposium*. Calgary.

Ye, X., Pang, F., & Zhang, A. (2014). Acoustic Radiation Induced by Bubble Motion in Compressible Fluid. *Applied Mathematics and Mechanics*, *35*(2), 177–190. doi:10.1007/s10483-014-1782-6

Zhang, C., Oostrom, M., Wietsma, T. W., Grate, J. W., & Warner, M. G. (2011). Influence of Viscous and Capillary Forces on Immiscible Fluid Displacement: Pore-Scale Experimental Study in a Water-Wet Micromodel Demonstrating Viscous and Capillary Fingering. *Energy & Fuels*, *25*(8), 3493–3505. doi:10.1021/ef101732k

Zou, X.-Y., Zhang, X., & Shaw, J. M. (2007). Phase Behavior of Athabasca Vacuum Bottoms + n-Alkane Mixtures. *SPE Production & Operations*, *22*(August 2005), 265–272. doi:10.2118/97661-PA